2024 SUMMER PROGRAMS @ CNF

:: FINAL REPORTS ::

2024 Cornell NanoScale Science & Technology Facility Research Experiences for Undergraduates (CNF REU) Program

2024 CNF REU Program with Morgan State University (CNF REU MSU)

Butcher Funded Tuskegee University Summer Program

2024 Cornell Robert Frederick Smith School of Chemical and Biomolecular Engineering FMRG: Cyber (CBE FMRG: Cyber) Summer Program

Cornell Center for Materials Research North Carolina Agricultural & Technical State University (CCMR NC A&T) Summer Program

2024 Xing Army Educational Outreach Program (AEOP)

2024 Cornell NanoScale Facility International Research Experiences for Undergraduates (CNF iREU) Program at National Institute for Materials Science (NIMS), Tsukuba, Ibaraki, Japan

2024 Global Quantum Leap International Research Training Experiences (GQL IRTE) Program at NIMS, Tsukuba, Ibaraki, Japan

TABLE of CONTENTS

:: :: ::

Identification of Microparticles from Low Resolution Optical Micrographs by Super Resolution

CNF Summer Student: Michael Batavia
Student Affiliation: Department of Computer Science and Engineering, NYU Tandon School of Engineering

Summer Program(s): 2024 Cornell Robert Frederick Smith School of Chemical and Biomolecular Engineering FMRG: Cyber (CBE FMRG: Cyber) Summer Program, 2024 Cornell NanoScale Science & Technology Facility Research Experiences for Undergraduates (CNF REU) Program

Principal Investigator(s): Prof. Nicholas Abbott, Prof. Fengqi You, Prof. Allison Godwin; Smith School of Chemical and Biomolecular Engineering, Cornell University

Mentor(s): Soumyamouli Pal, Guangyao Chen; Smith School of Chemical and Biomolecular Engineering, Cornell University

Primary Source(s) of Research Funding: National Science Foundation under Grant No. NNCI-2025233 and CMMI-2229092

Contact: batavm01@nyu.edu. nla34@cornell.edu, fengqi.you@cornell.edu, afg64@cornell.edu, sp2476@cornell.edu, gy.chen@cornell.edu

Abstract:

Observation of iCVD polymerization *in-situ* is often challenging due to the use of a long-distance focal lens needed to observe the reaction and external motor vibrations from the reactor leading to low resolutions and slight rotation and translation in images captured. In this research, we aim to improve the low resolution retrieved from *in-situ* monitoring and enable identification and characterization of individual polymer particles dispersed and aggregated as clusters. To achieve this, we fine-tune and train the Real-ESRGAN super resolution neural network using pairs of *in-situ* low resolution and *ex-situ* high resolution optical micrographs of 5 μm polystyrene particles dispersed in 5CB liquid crystal (LC), which are used as a surrogate for the polymer particles formed by iCVD. Through pure computer vision techniques, we successfully identify microparticle clusters in the upscaled images and approximate their properties using bounding box approximation. Despite longer training times compared to object detection methods, this method shows promise of identifying and characterizing individual microparticles via binary erosion and promises scalability and generalizability in identifying future microparticle clusters without need for manual identification and loss of spatial awareness of the clusters in the dataset.

Summary of Research:

In order to upscale the low-resolution (LR) *in-situ* images to their high-resolution (HR) *ex-situ* counterparts via super resolution, we focus on isolating the slide containing the microparticle clusters of interest in the images and collect them into a new LR-HR slide pair dataset. This ensures that the clusters are the target of the upscale instead of any extraneous background noise from the image.

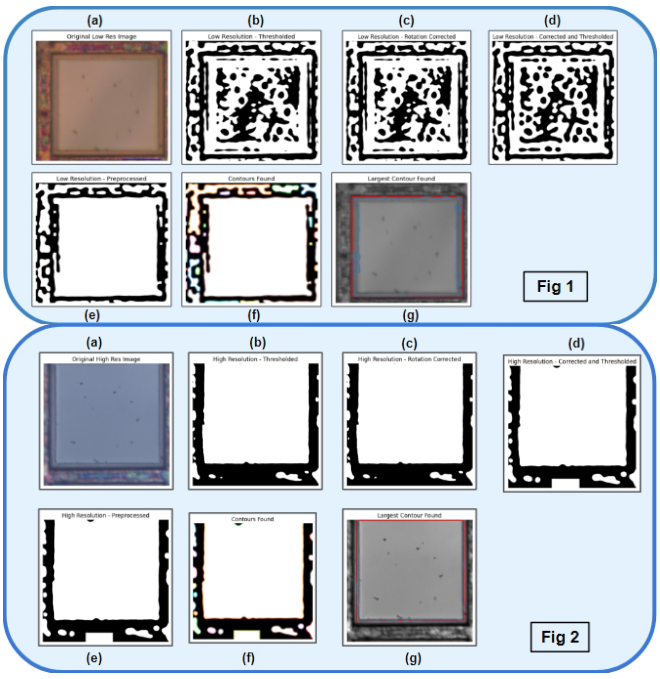

Figure 1, top: Full pipeline identifying the steps needed to isolate and crop the slide from a sample LR image into the new LR-HR slide dataset. Figure 2, bottom: Full pipeline identifying the steps needed to isolate and crop the slide from a HR image into the new LR-HR slide dataset.

Figures 1 and 2 show the computer vision pipeline needed to isolate the slide in the LR/HR images and curate the LR-HR pair dataset to pass to Real-ESRGAN. In order to isolate the slide in the LR images in Figure 1, we start by applying a Gaussian blur ($\sigma = 20$) and an adaptive threshold with a 65 pixel block size to create an initial segmentation of the image into foreground and background [Figure 1a-b].

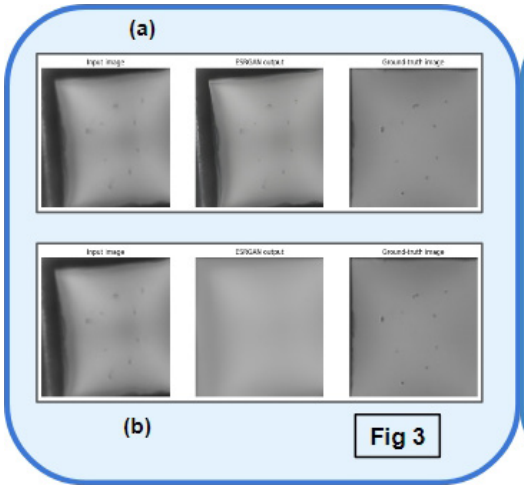

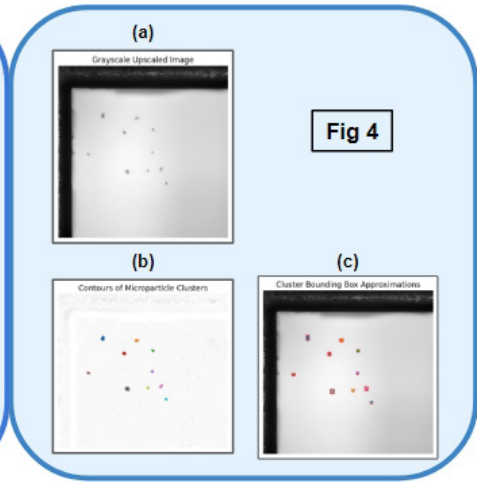

Figure 3, left: Comparison of visual output of super resolution upscaled output between pure inference Real-ESRGAN (a) and fine-tuned Real-ESRGAN (b). Figure 4, right: Process of identifying and characterizing microparticle clusters from the inference upscaled LR images.

To correct for slight rotations, we applied a Hough Transform to both images to rotate them to a top-down POV [Figure 1c]. Another Gaussian blur and adaptive thresholding was run on the rotated images to clean and straighten the thresholds; this was followed by passing the images into an algorithm to fill binary holes in closed shapes and to a binary opening with a square footprint of size 16 to merge various thresholded contours together [Figure 1d-e]. We then use the Marching Squares algorithm on the filled thresholded image, which uses a lookup table to connect lines together in binary images to draw contours and filter the returned contour list by area to identify the largest contour in the image: the slide [Figure 1e-g]. Isolating the slides in the HR images follows the same procedure except for the initial adaptive thresholding, which was changed to Otsu thresholding due to the easier contrast between foreground and background in the provided images [Figure 2]. Both found slides were cropped from their respective image into roughly 800 × 800 image patches to form the LR-HR pair dataset.

Super resolution was done by passing the LR-HR pair dataset into Real-ESRGAN for 4x upscaling. We compare the upscale by running the neural network by pure inference using only the pretrained weights and by fine-tuning the neural network with the weights over the training and validation data for 50 epochs (learning rate = 0.0001). Results were compared between the two groups by visual inspection and by using three image quality metrics: NIQE (Natural Image Quality Evaluator), PSNR (Peak Signal-To-Noise Ratio) and SSIM (Structured Similarity Index Measure). The visual output of the pure inference neural network and fine-tuned neural network for one image are shown in Figures 3a-b.

Over the test set, the average NIQE, PSNR and SSIM for the base network were 10.7, 17.8, 0.90 respectively. For the fine-tuned network, the average NIQE, PSNR and SSIM were 14.0, 22.6 and 0.94 respectively. This indicates that with further training of Real-ESRGAN, the fine-tuned network could perform even better upscaling than inference super resolution alone, though it may take longer to generate than current conventional methods.

In order to identify the microparticle clusters in the upscaled inference images, we applied a morphological reconstruction by erosion and an alternating binary opening and closing followed by the Marching Squares algorithm to identify all contours in the resulting image, which happened to be the clusters themselves [Figures 4a-c].

Properties of the microparticle clusters such as area and circumference were then able to be found via bounding box approximation. Furthermore, the spatial locations of the microparticles and their clusters with respect to each other in the same LC sample are retained in the upscaled images, which will allow for correlating LC local orientations to the particle properties.

Conclusions and Future Steps:

This research shows it is possible to use a super resolution neural network to upscale a LR image and characterize microparticle clusters scalable with the size of the provided dataset and, at the same time, retaining the relative spatial positions of each cluster. With further fine-tuning, it may be possible to characterize clusters in higher definition than can be done with pure super resolution inference. Individual microparticles in the clusters also show promise upon being detected with more investigation. In the future, we plan to fine-tune three data subsets of LR-HR pairs of size 30, 60 and 120 to see if dataset size has an impact on super resolution visual and metric performance and test to see if the super resolution preprocessing and procedure is robust to microparticle clusters of various sizes and types.

Acknowledgements:

Special thanks go out to Soumyamouli Pal and Guangyao Chen for their support and mentorship throughout the research experience. I would also like to acknowledge the Cornell NanoScale Facility Research Experiences for Undergraduates (CNF REU) Program for hosting this internship. This work was funded by the National Science Foundation via grants no. NNCI-2025233 and CMMI-2229092.

Fabrication of Superconducting Resonators on hBN Thin Films

CNF Summer Student: River Chen
Student Affiliation: Materials Science and Engineering, University of Illinois Urbana-Champaign

Summer Program(s): 2024 Cornell NanoScale Science & Technology Facility Research Experiences for Undergraduates (CNF REU) Program
Principal Investigator(s): Professor Zhiting Tian, Mechanical and Aerospace Engineering, Cornell University
Mentor(s): Joyce Christiansen-Salameh, Sibley School of Mechanical and Aerospace Engineering, Cornell University
Primary Source(s) of Research Funding: National Science Foundation under Grant No. NNCI-2025233; AFOSR Award Number FA9550-22-1-0177
Contact: riveryc2@illinois.edu, zt223@cornell.edu, jc3496@cornell.edu
Summer Program Website(s): https://cnf.cornell.edu/education/reu/2024, https://ztgroup.org/
Primary CNF Tools Used: AJA Sputter 1 and 2, ABM Contact Aligner, Plasma-Therm 770 Etcher

Abstract:

Studying loss in superconducting devices is essential for high coherence quantum devices. Dielectric loss at the metal-substrate interface is a significant contributor to overall loss [1], which is why methods to study this important factor have been developed [2,3]. hexagonal boron nitride (hBN) is a 2D material with several applicable properties, including low dielectric loss, chemical stability, and atomically flat surfaces free of dangling bonds, properties that make it an attractive material for integration into superconducting circuits [4]. In this research we employed a coplanar waveguide resonator design that is sensitive to dielectric loss at the metal substrate interface, comparing a "control" niobium (Nb)-on-sapphire resonator and an Nb-on-hBN-on-sapphire resonator.

Summary of Research:

Superconducting resonators are used to characterize materials loss in superconducting quantum computers [5]. The chip design used in this research implements eight multiplexed quarter wave resonators inductively coupled to a feedline with tapered bond pads as shown in Figure 1a. Areas where metal is removed are shown in orange, and metallized areas are shown in white. This design allows for 1:1 comparisons of dielectric losses at the metal substrate interface [2].

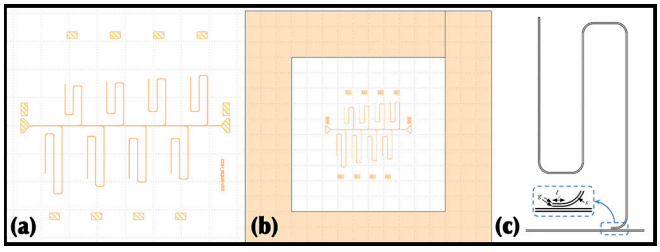

Figure 1: Device mask design. (a) Original 7.5 × 7.5 mm design. (b) Modified 6 × 6 mm design with border for alignment. (c) A single superconducting resonator with gap width g *and conductor width* s*. Diagram from Kopas, et al. [2].*

Any given resonator, as visible in Figure 1c, exhibited a gap width *g* of 3 μm and conductor width *s* of 6 μm. This was also true for the feedline, and we qualified the resolution of our device features throughout our process development based on these metrics.

The original design, shown in Figure 1a, supports a 7.5 × 7.5 mm device size, and we were fabricating on 10 × 10 mm sapphire substrates. Upon completion of our devices, they would be brought to a controlled facility which supports a 6 × 6 mm chip testing platform. We shrunk the design and added a guideline box around the device for improved mask alignment, better centering the new 6 × 6 mm device design (Figure 1b).

All 10 × 10 mm chips were cleaned via sonication for 10 minutes each in acetone, IPA, and water.

Molecular Beam Epitaxy (MBE). The first step in our device fabrication process was the growth of high-quality BN thin films via MBE on our ~ 500 μm thick sapphire substrate. Figure 2(a) shows resonant high-energy electron diffraction pattern indicating epitaxial quality of hBN film, Figure 2(b) is a Raman spectra showing the sharp characteristic hBN peak, and Figure 2(c) displays an AFM map of the film surface.

Sputter Deposition. After verifying the quality of our 5 nm thick hBN film, 600Å of Nb were sputtered at the default 400 Watts on an AJA Sputter Deposition tool.

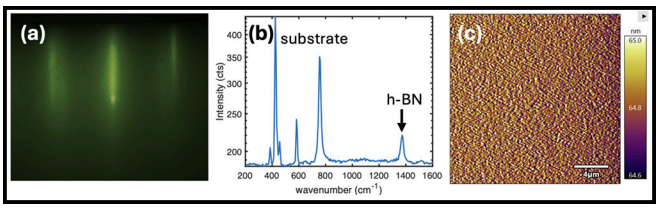

Figure 2: (a) Electron diffraction pattern, (b) Raman spectra, and (c) AFM map of hBN thin film.

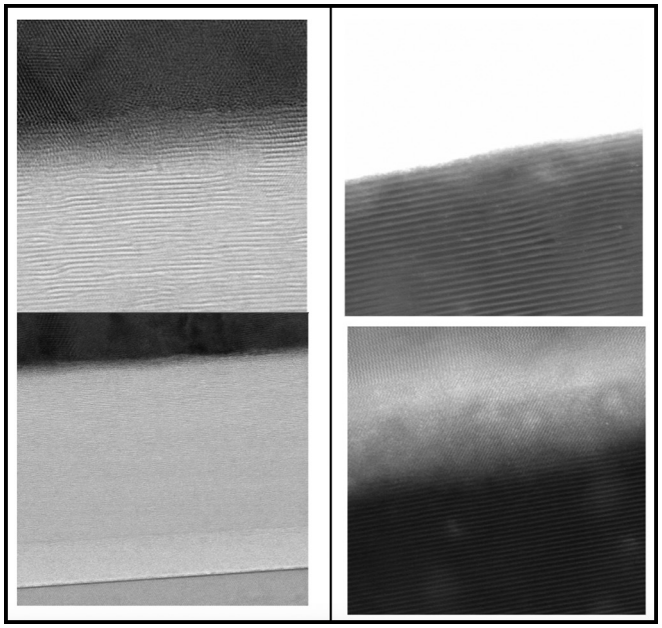

Figure 3: TEM of Nb sputter at 400W (left) and 50W (right) on hBN thin film.

In Figure 3, on the left side column, TEM of the hBN-Nb interface is shown to be damaged by the high-power metal ion bombardment.

We found, as shown in Figure 3 on the right-side column, that a lower sputter power of 50 watts maintained a pristine hBN film surface. Using a P7 profilometer, we determined that a sputter time of 10 minutes at this lower power yielded a 161Å thick layer of Nb. Therefore, a sputter time of 37.27 minutes or 2236.03 seconds would yield our desired 600Å of metal.

We were also interested in later comparing aluminum (Al) on sapphire and Al on hBN on sapphire resonators, so we also sputtered Al at 50 W for 10 minutes. Again, we used profilometry to determine an experimental average of 265Å of sputtered Al through the 10-minute period.

Photolithography. We sputtered 60 nm Nb onto several 10 × 10 mm sapphire substrates in order to test and establish our photolithography process.

S1805 photoresist spun at 4000 rpm for 60 seconds yielded an average thickness of 500 nm. Our several resist-coated substrates were subsequently exposed at varying doses on the ABM Contact Aligner to determine the exposure time for optimal feature definition. The best exposure time was found to be 1.6 seconds.

Reactive Ion Etch (RIE). It was predicted that the RIE Cl2 etch chemistry on the Plasma-Therm 770 etcher could also affect the hBN thin film upon etching through the Nb. Thus, the first step to mitigate this issue was to accurately determine the Nb etch rate. After 36.7 seconds of etching our device pattern, we found that 36.8 nm of niobium was etched and 36.57 nm of resist was etched. These measurements establish a 1:1 etch selectivity and 1nm/second etch rate.

A similar process was performed on the hBN where a pattern was etched for 15 seconds. We determined that the hBN

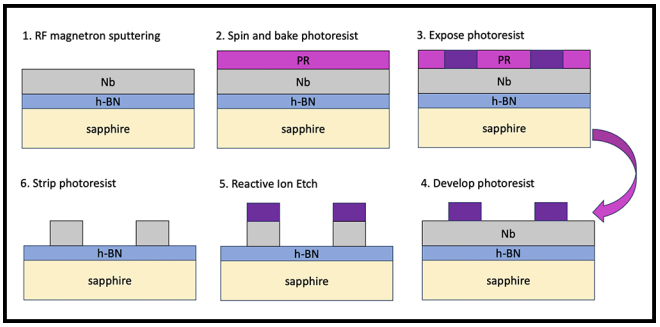

Figure 4: Complete fabrication process.

thin film experienced an etch rate of ~ 1 nm/3 seconds after performing atomic force microscopy on a sample.

Conclusions and Future Steps:

After establishing our etch process parameters, we would similarly verify the niobium was etched through by using a probe station to measure resistance between the gaps and the conductor, determining whether there is Nb in the gaps.

It has been shown that the superconducting transition temperature T_c of a metal can be affected by the substrate material [6]. We will observe this change using a Physical Property Measurement System, examining the change in resistance with varying extremely low temperatures.

As the pieces are required to conform to a 6 × 6 mm testing platform, they will be sent to DISCO laser dicing services.

Finally, the completed devices will be wirebonded and tested in a facility equipped with a He dilution fridge.

Acknowledgements:

I would like to thank Cornell University, NNCI, and the NSF for funding this research via grant NNCI-2025233. Thank you to Joyce, Professor Zhiting Tian, and the staff at the Cornell NanoScale Facility for all the guidance and support throughout this project.

References:

[1] C. R. H. McRae, et al. Materials loss measurements using superconducting microwave resonators. Rev. Sci. Instrum. 1 September 2020; 91 (9): 091101. https://doi.org/10.1063/5.0017378.

[2] Kopas, et al. Simple coplanar waveguide resonator mask targeting metal-substrate interface. arXiv 14 Apr 2022. https://arxiv.org/abs/2204.07202.

[3] Woods, W., et al. (2019). Determining Interface Dielectric Losses in Superconducting Coplanar-Waveguide Resonators. Phys. Rev. Appl., 12, 014012. doi:10.1103/PhysRevApplied.12.014012.

[4] Wang, J.IJ., et al. Hexagonal boron nitride as a low-loss dielectric for superconducting quantum circuits and qubits. Nat. Mater. 21, 398-403 (2022). https://doi.org/10.1038/s41563-021-01187-w.

[5] C. McRae, et al. Review of Scientific Instruments 91, 091101 (2020).

[6] J. Liu, et al. "Study of Stress and Morphology of Superconducting Niobium Thin Films," IEEE Transactions on App. Superconductivity, vol. 19, no. 3, pp. 245-248, June 2009, doi: 10.1109/TASC.2009.2019233.

Fabrication of 2D-Material-Based Ionic Transistors

CNF Summer Student: Siyi (Cathy) Chen
Student Affiliation: Materials Science and Engineering, University of Illinois at Urbana-Champaign

Summer Program(s): 2024 Cornell NanoScale Science & Technology Facility Research Experiences for Undergraduates (CNF REU) Program
Principal Investigator(s): Yu Zhong, Assistant Professor, Materials Science and Engineering, Cornell University
Mentor(s): Kaushik Chivukula, Graduate Student, Materials Science and Engineering, Cornell University
Primary Source(s) of Research Funding: National Science Foundation under Grant No. NNCI-2025233
Contact: cathychen0915k@gmail.com, yz2833@cornell.edu, kc836@cornell.edu
Summer Program Website: https://cnf.cornell.edu/education/reu/2024
Primary CNF Tools Used: Heidelberg Mask Writer DWL-2000, ABM Contact Aligner, Oxford 81 RIE, AJA Ion Mill, SC4500 Even-Hour Evaporator

Abstract:

Traditional electronic field-effect transistors (FETs), which utilize electrons and holes as charge carriers, are indispensable in modern electronic devices such as integrated circuits and microprocessors. They form the backbone of today's digital technology by enabling efficient information processing, storage, and transmission. Despite ongoing challenges in the miniaturization of electronic transistors, ionic FETs offer distinct advantages, particularly biocompatibility and tunable conductance. Our project aims to fabricate ionic transistors using advanced 2D materials and address the limitation of low on-off current ratios in these devices.

Summary of Research:

The human brain, with its highly selective ionic transmission system, processes vast amounts of information and facilitates neural communication daily. To mimic the ultra-functional capabilities of the brain, nano-channeled ionic field-effect transistors that use ions like Na^+ and Ca^{2+} as carriers, similar to those in neural processes, show great potential for future applications. Such transistors are promising for artificial brain systems and memory devices like neuromorphic memristors due to their unique ability to maintain discrete conductivity states, which serve as memory storage units.

In order to replicate the ultra-selectivity of brain ionic channels and increase the on-off ratio, we focused on fabricating ionic transistors with nanochannels approaching the Debye length. Conventional microchannels, characterized by their short Debye lengths and discontinuous electric field effects, often result in the undesirable coexistence of both negative and positive ions. In contrast, the nanochannel design allows the electric field to penetrate the entire channel, predominantly permitting the passage of only a single ion type. This ensures a low energy consumption in the transistor, mirroring brain functions.

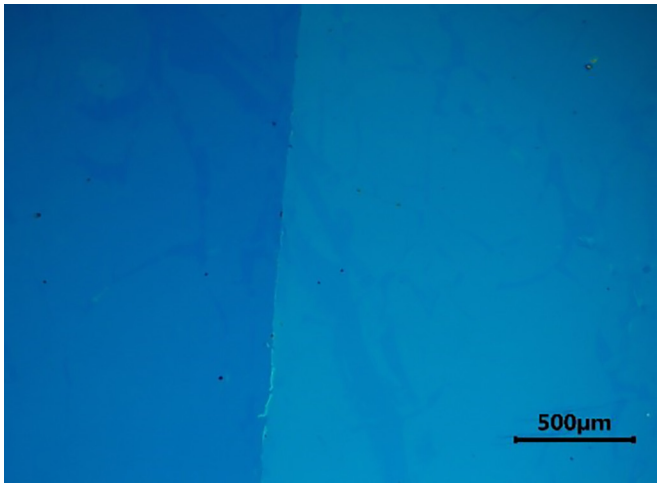

Figure 1: A stable 2D heterostructure is illustrated.

We began by preparing a silicon wafer with a 300 nm thermal oxide layer, cutting it into 1-inch by 1-inch pieces. To create the nanochannel ionic pathway, we deposited a monolayer of 2D Copper-Tetrakis (4-carboxyphenyl) porphyrin (CU-TCPP) by immersing the wafer pieces in a copper nitrate solution, capping them with hexane, and injecting TCPP solution using a syringe pump. After allowing the hexane to evaporate, the remaining solution was drained. Thereafter, a monolayer of molybdenum disulfide (MoS_2) was exfoliated and transferred onto the CU-TCPP-coated pieces, resulting in the formation of a stable 2D heterostructure, as illustrated in Figure 1.

To etch the MoS_2 monolayer into a 100 μm by 100 μm pattern, photolithography and the AJA ion mill at the Cornell NanoScale Facility were employed. Oxygen plasma then removed the photoresist cleanly. Next, we deposited 50 nm of silicon dioxide using the Oxford Atomic Layer Deposition

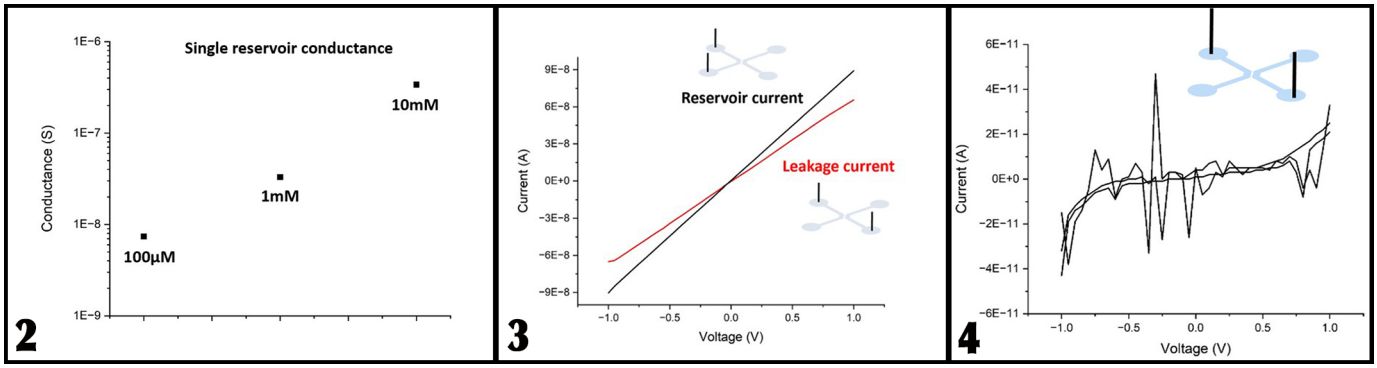

FlexAL machine to serve as the insulating layer of the ionic field effect transistor. The gate electrode was fabricated by depositing 10 nm of titanium and 50 nm of gold with the Thermal/E-gun Evaporation System, followed by a lift-off process using hot N-Methylpyrrolidone (NMP) stripper. The source and drain channels were defined using SU-8 and photolithography, and subsequently etched with the Oxford reactive ion etching tool. Finally, capping the pieces with polydimethylsiloxane (PDMS) completed the fabrication process.

For the measurement of Single Reservoir Conductance, four holes were made in the PDMS, into which sodium chloride (NaCl) electrolyte was injected. Two silver electrodes were placed in the same reservoir. With ions flowing freely within the unobstructed single fluid channel, conductivity was observed, confirming the successful fabrication of the single reservoir. Figure 2 shows the relationship between the NaCl solution concentration and its conductance, indicating that as the concentration increases, the number of ions available for carrying electric current also increases, leading to higher conductance.

During the leakage test, electrodes were placed in two separate fluid channels rather than in the same one. Without a nanochannel allowing current to flow between the channels in this case, no current should have been detected when applying voltage if there was no leakage. However, as shown in Figure 3, when voltage ranging from -1V to 1V was applied, a leakage current of approximately 10^{-8} A was detected. This current is of the same order as that of a single connected reservoir, suggesting that some leakage was indeed occurring between the two fluid channels.

To address this issue, we applied Vapor Phase (3-Aminopropyl) triethoxysilane (APTES) treatment [1] to the PDMS to induce covalent bonding between SU-8 and PDMS, enhancing the sealing of the fluid channels.

After this optimization, we repeated the leakage test under identical conditions. This time, the current was around 10^{-11} A, which is three orders of magnitude lower than the previous leakage current, and no linear trend was observed in Figure 4. This minor current, likely due to the open holes, was close enough to zero to indicate that there was no leakage, confirming the successful fabrication of a leakage-free device, ready for future experiments and innovations.

Conclusions and Future Steps:

In conclusion, our 2D material-based ionic field effect transistors demonstrate potential for applications in future Neuromorphic Computing systems by simulating brain functions. The use of Oxygen Plasma effectively removed the photoresist, while Hot NMP facilitated the lift-off process. The leakage between source and drain channels was minimized through APTES treatment of PDMS, resulting in a non-leakage current of approximately 10^{-11} A under a voltage range of -1V to 1V. Future work should focus on testing and measuring the conductance of different organic molecule cages, which could lead to the selective manipulation of ion types passing through the transistors.

Acknowledgements:

Special thanks to the 2024 Cornell NanoScale Facility Research Experiences for Undergraduates (CNF REU) Program funded by the National Science Foundation under Grant No. NNCI-2025233, and the National Nanotechnology Coordinated Infrastructure. I would also like to thank Prof. Yu Zhong and Kaushik Chivukula for their mentorship, as well as the CNF staff and program coordinators for their support.

References:

[1] Micromachines 2015, 6(12), 1923-1934.

Measuring the Stiffness of Embryonic Avian Myocardium Using Micropipette Aspiration Technique

CNF Summer Student: Kyla Christopher
Student Affiliation: College of Agriculture, Environment, and Nutrition Sciences, Tuskegee University

Summer Program(s): 2024 Butcher-Funded Tuskegee University Summer Program, 2024 Cornell NanoScale Facility Research Experiences for Undergraduates (CNF REU) Program

Principal Investigator(s): Jonathan Butcher, Biomedical Engineering, Cornell University

Mentor(s): Shuofei Sun, Alex Cruz; Biomedical Engineering, Cornell University

Primary Source(s) of Research Funding: 2024 Butcher-Funded Tuskegee University Summer Program (EF-2222434), National Science Foundation under Grant No. NNCI-2025233

Contact: kchristopher4205@tuskegee.edu, jtb47@tuskegee.edu, ss3946@cornell.edu, ac2853@cornell.edu

Summer Program Website: https://cnf.cornell.edu/education/reu/2024

Abstract:

Mechanical forces are essential to cardiac formation. The mechanosensitive (MS) ion channel, Piezo1, responds to different mechanical forces and converts them into intracellular signals. Yoda1 is a synthetic drug that serves as a specific agonist for the Piezo1 ion channel by binding to it, causing conformational changes that open the channel. Congenital heart defects (CHD) occur when cardiac morphogenetic processes are disrupted. CHDs affect approximately 2% of infants and are the primary cause of death in children under one year of age. CHD are the largest class of birth defects and account for 25% of all human congenital abnormalities. Chick embryos were used as a research model due to ease of microsurgical accessibility in the egg, and developmental similarities with human embryos, including a four-chamber heart. In this experiment, chick embryos were windowed and injected with Yoda1 to investigate the mechanical properties of the myocardium. We hypothesized that higher concentrations of Yoda1 would stiffen the myocardium. Our findings show that Yoda1 stiffened the myocardium and thus successfully stimulated the Piezo1 ion channels in the cardiomyocytes.

Summary of Research:

Cardiac morphogenesis varies across species but can be broken down into four key steps across vertebrates: heart tube formation, looping, trabeculation, and valve formation/septation. At the beginning stages of cardiogenesis, the cardiac wall is composed of an inner endocardial layer and outer myocardial sheath. Between these two layers is the cardiac jelly. As shown in Figure 1, when the heart tube extends and elongates, looping occurs and will promote growth of the atria and atrial septum. In cardiac trabeculation, endocardial extensions grow toward the myocardial layer, giving rise to trabeculae. Septation of the atrium and ventricles transpires when trabeculae compact and endothelial cells (ECs) fuse.

The myocardium is responsible for contractility of the heart and pumping action. The cardiac muscle must contract with the necessary force so enough blood can supply the metabolic demands of the body. Yoda1 caused an increase in Piezo1 activity which in turn made the myocardium more sensitive to mechanical loads.

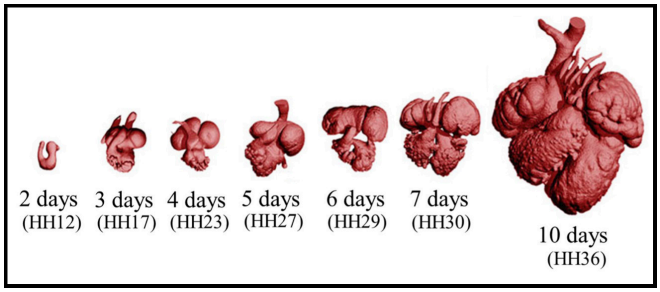

Figure 1: Images of chick embryo heart throughout development.

In the study, chick embryos were incubated until they reach HH 27. The eggs were then windowed in ovo and the eggshell membrane was removed to expose the chorioallantoic membrane (CAM). A pulled glass pipette needle was secured to a micromanipulator. Demonstrated in Figure 2, embryos were injected into the vitelline vein of the vasculature so the solution flowed directly to the heart.

Twelve embryos for three of the four HH stages used in this study (HH 31, HH 36, HH 38) were injected with Yoda1 and Hanks' Balanced Salt Solution (HBSS). For the three HH stages, three embryos were injected with a concentration of 5 μmol of Yoda1, three embryos were injected with a concentration of 10 μmol of Yoda1, three embryos were injected with a concentration of 15 μmol of Yoda1, finally, three embryos were injected with HBSS. All chick embryos were windowed and injected on HH 27. The other HH stages are the days the embryo's hearts were removed and measured. The twelve embryos whose hearts were removed in the fourth group, HH 27, received neither saline nor Yoda1 injections.

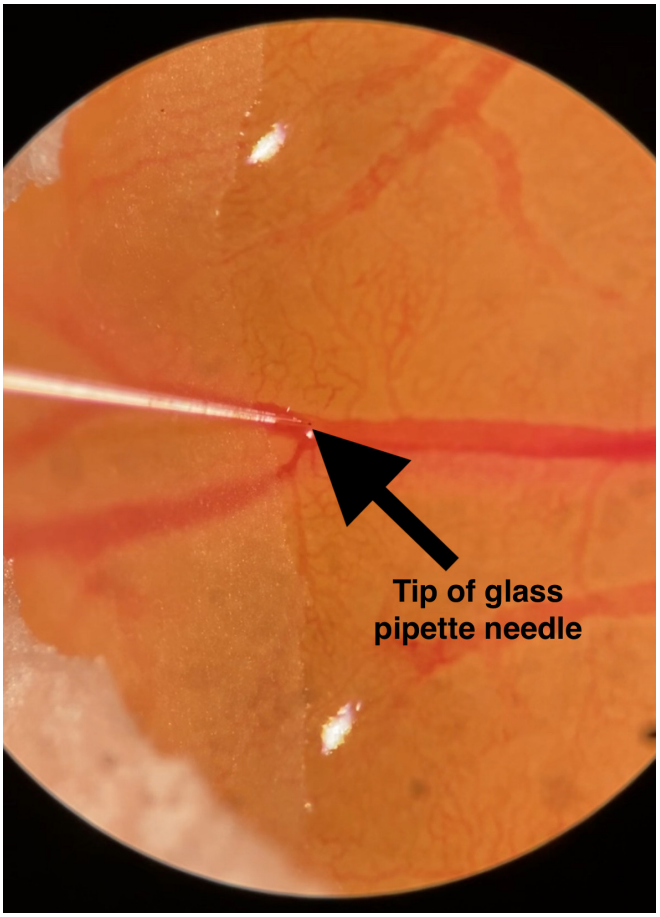

Figure 2: The needle is inserted in a vein, where blood flows toward the heart.

During the chick embryo heart removal, a portion of the left ventricle (LV), right ventricle (RV), and interventricular septum were removed for micropipette aspiration (MPA). MPA applies a controlled vacuum pressure and oversees tissue displacement within the tip of the pipette. MPA was used to determine the stiffness of the myocardium and how saline and different concentrations of Yoda1 influenced the stiffness of the myocardium. The ventricle and septum samples were secured to a polydimethylsiloxane (PDMS) Petri® dish for measurement. The PDMS was placed on the stage of a stereo microscope under a magnification of 150x. Before the tissue is measured it is first "massaged" to relax the cardiac muscle and ensure it is in contact with the pipette tip. Once massaged, a vacuum pressure was applied in increments of 2 μl, 2 μl, 3 μl, 3 μl, 4 μl, 4 μl, 5 μl, 5 μl, 6 μl, 6 μl, 7 μl, 7 μl, 8 μl, 8 μl to the myocardium surface in the interior of the pipette. The aspirated tissue was then imaged and measured in the research application, ImageJ, using a scale bar.

Conclusions and Future Steps:

Results from MPA showed that the sampled heart tissue injected with Yoda1 had a stiffer myocardium than the sampled heart tissue injected with HBSS. Figure 3 shows the formula our experimental values were fitted to.

$$\sigma_{yy} = \alpha C \exp\left[\alpha\left(\lambda^2 + \frac{2}{\lambda} - 3\right)\right]\left(\lambda^2 - \frac{1}{\lambda}\right)$$

Figure 3: Change pressure is represented by σ_{yy} and α and C are the variables that are changed to fit the measured data.

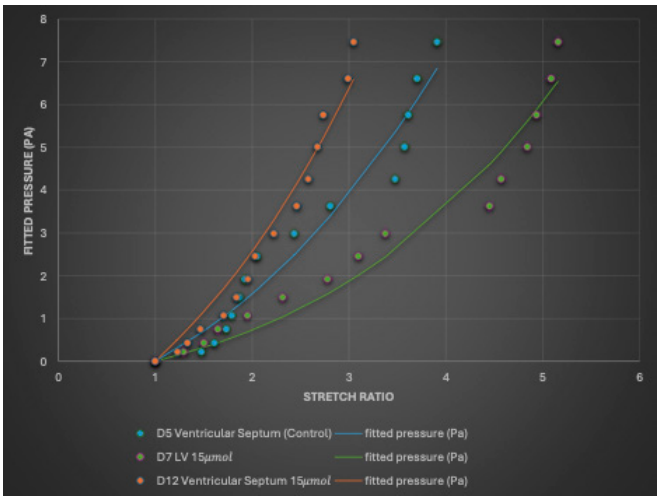

Figure 4: Stretch ratio always begins at "1" and fitted pressure always starts at "0" in this experiment.

In Figure 4, HH 38 had a steeper experimental curve compared to the HH 27 control group. A steeper value indicated a stiffer myocardium. In this experiment, over 60% of chick embryos died in this experiment, including all HH 36 embryos. Survival Rate (SR) of embryos was between 30% and 40%. For future studies, we want to improve the SR of chick embryos. Controlling contamination and ensuring embryos do not bleed out during injections is a possible solution to improving SR.

Acknowledgements:

This work was performed at the Butcher Lab and funded by the 2024 National Science Foundation (EF-2222434), the Cornell Einhorn Center for Community Engagement, the College of Engineering Diversity Programs in Engineering, and the National Institutes of Health HL160028, and the Cornell NanoScale Facility (NNCI-2025233). Special thanks to Prof. Jonathan Butcher, Shuofei Sun, and Alexander Cruz.

References:

[1] Lindsey, S., Butcher, J., Yalcin, H. Mechanical regulation of cardiac development. Frontiers in Physiology. 10.3389/fphys.00318 (2014).

[2] Lin, Chien-Jung, Lin, Chieh-Yu, Chen, C., Zhou, B., Chang, C. Partitioning the heart: Mechanisms of Cardiac Septation and Valve Development. Development 139, 3277-3299 (2012).

[3] Buskohl, P.R., Gould, R.A., Butcher, J.T. Quantification of embryonic atrioventricular valve biomechanics during morphogenesis. J Biomech 45(5): 895-902 (2012).

Characterization of Joined Alumina Components Manufactured via Digital Light Processing

CNF Summer Student: Brooklyn Jenkins
Student Affiliation: Mechanical Engineering, North Carolina Agricultural and Technical State University

Summer Program(s): 2024 Cornell Center for Materials Research North Carolina Agricultural & Technical State University (CCMR NC A&T) Summer Program, 2024 Cornell NanoScale Science & Technology Facility Research Experiences for Undergraduates (CNF REU) Program

Principal Investigator(s): Sadaf Sobhani, Mechanical and Aerospace Engineering, Cornell University

Mentor(s): Charlotte Albunio, Mechanical and Aerospace Engineering, Cornell University

Primary Source(s) of Research Funding: Cornell Center Materials Research NC A&T 2024, National Science Foundation under Grant No. NNCI-2025233, Empire State Development, Air Force Research Laboratory Regional Network, Fuze Hub, Cornell Atkinson Center for Sustainability

Contact: brjenkins1@aggies.ncat.edu, sobhani@cornell.edu, ca527@cornell.edu

Summer Program Website(s): https://www.sobhanilab.com/, https://cnf.cornell.edu/education/reu/2024

Primary Tools Used: Instron 5569, Admaflex 130

Abstract:

This study demonstrates effective strategies for overcoming print volume limitations in 3D printing of ceramics, offering insights into joint design and material performance critical for advancing large-scale ceramic manufacturing applications. The utilization of large-scale additively manufactured ceramic parts is constrained by print volume limitations. To address this challenge, this study investigates the mechanical performance of joined alumina ceramic beams created with the Admaflex 130 via Digital Light Processing (DLP), a method involving photosensitive resin and ceramic particles. Various joint designs are evaluated: Flat, Mouse Door, Notch, and T-slot; to discover their efficacy in joining these ceramic beams. Experimental tests included ambient flexural testing and thermal shock flexural testing, involving rapid cooling in a water bath after heating. While the standard alumina beam has a flexural strength of around 300 MPa, strength significantly decreases when joining. The T-slot joint, exhibited superior performance, over all geometries, as it achieved 88 MPa in ambient conditions and 55 MPa under thermal shock conditions. Comparatively, the Mouse Door joint showed a performance of 75 MPa in ambient flexural strength and, 30 MPa in thermal shock, surpassing the Notch joint which achieved 55 MPa in ambient flexural strength and 20 MPa under thermal shock.

Summary of Research:

Print volume constraints of digital light processing (DLP) printers, such as the Admaflex 130, limit the ability to print complex parts on larger scales. DLP is a mask-based technique of integral image transfer to the photopolymerizable liquid surface by exposing the light source through a patterned mask once only [1]. Previous research has explored the relationships between joint strength and cure time, as well as joint strength and sintering temperature. However, all tests were conducted using the same joint geometry. The findings indicated that strength was not significantly affected by curing time but was highly dependent on sintering temperature [2]. The different geometric designs compared, also ranked by surface area are Flat, Mouse Door, Notch, and T-slot — which can be seen in Figure 1. These interfaces are used to find the best configuration for strength and load-bearing capacity. These geometric interfaces were created to investigate how to get proper alignment while minimizing strength reduction and ensure proper alignment which is essential for complex shapes. It is hypothesized that the larger surface area will result in greater strength.

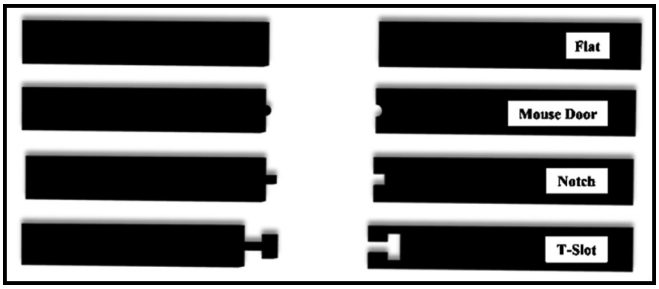

Figure 1: Types of interfaces used to join ceramic beams-Flat, Mouse Door, Notch, and T-Slot.

To create the ceramic beams, the Admaflex 130 machine is used, with a limiting build plate size of 54 × 96 × 110 mm. After printing, the ceramic beams are removed from the plate and cleaned with water and isopropyl alcohol to get rid of any leftover slurry. The beams are dried and then joined using a pea-sized amount of slurry followed by each face of the beam being exposed to UV light near 405 nm at 46 mW/cm^2 for one minute. The parts are then debound and

$$S = \frac{3PL}{2bd^2}$$

Figure 2: Equation used to calculate strength when ambient flexural strength tests are done. In this equation, P represents the break force, L denotes the outer support span, b indicates the specimen width, and d signifies the specimen thickness.

sintered. Debinding involves soaking the ceramic beams in a heated water bath (40°C) for 24 hours to remove the water-soluble resin. Then, a thermal debind is performed at 1000°C, resulting in brittle, chalk-like parts. Then sintering is done, at 1625°C, fully densifying the beams and shrinking them to the desired size of 3 mm × 4 mm × 45 mm. To test the strength of these joints, ambient flexural strength tests are conducted according to ASTM C1161-18 standards. The strength is calculated according to Figure 2, where S is strength, P is breaking force, L is outer support span, B is specimen width, and D is specimen thickness. Upon ambient flexural strength testing, the ceramic beams are broken. As seen in Figure 2, for all joints except the T-slot, failure occurs due to the joint slurry, as no breakage occurs through the joint geometry. This implies that the weakness of the joint is coming from the procedure of ceramic beam joining. It is also important to note that although the T-slot breaks in half, the other joints break but keep their geometry.

The results of this testing indicate that the Mouse Door and T Slot joint, with slurry, offer superior strength, making them preferable in mechanical strength applications. Notably, the T-Slot is two times stronger than the Flat. All complex geometries with slurry outperform the flat joint, suggesting the complexity of the joint improves strength. Next, joint performance under thermal shock was assessed, per ASTM E1225-20 guidelines. Here, samples are rapidly cooled after being heated to 400°C above bath temperature for fifteen minutes. The results shown in Figure 4 indicate that the T-slot joint with slurry remains the highest strength, while the Flat joint has the lowest strength. Interestingly, for ambient flexural testing, the Mouse Door joint is stronger than the Notch joint, contrary to initial expectations. The results suggest that T-slot joints are stronger than Flat joints. However, thermal shock tests reveal that ceramic joints can lose significant strength after sudden temperature changes. For the flat, 29.4% of strength is lost, 27% for Mouse door, 45.3% for notch, and lastly 62.9% for T-Slot with slurry and 69.5% without slurry.

Conclusion and Future Work:

This research offers valuable insights into ceramic joining, helping to standardize and quantify the effects of these joints. Among all the joints compared, the T-slot joint demonstrated significantly greater strength, both in ambient flexural strength testing and after undergoing thermal shock procedure. Future work will explore joint orientation, and joint strength on conductivity testing because that could impact our current observed data. This research offers valuable insights into ceramic joining to help standardize and quantify the effects of these joints. Thermal conductivity affects not only joint strength but also the introduction of new interfaces which can influence thermal shock behavior. Lastly, it is important to

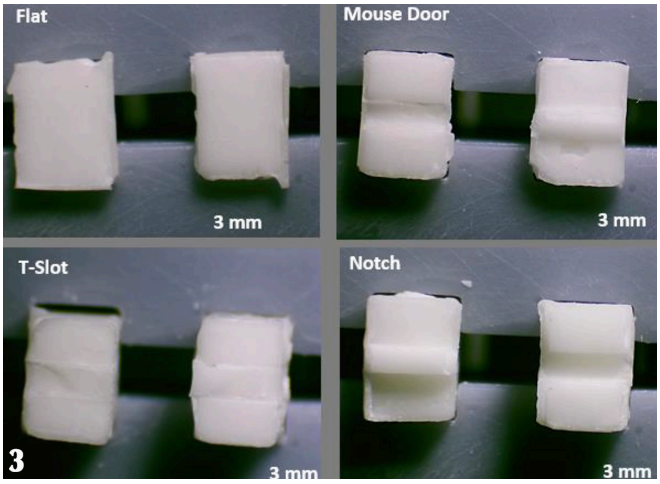

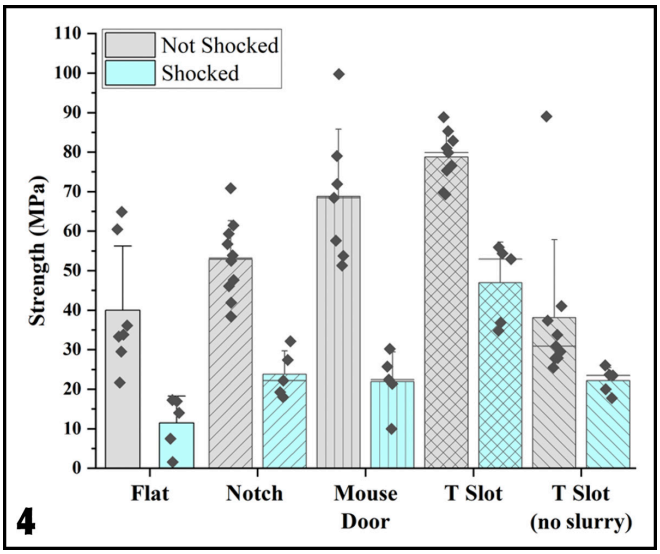

Figure 3, top: The ceramic beams upon ambient flexural strength testing. Figure 4, bottom: Types of interfaces used to join ceramic beams-Flat, Mouse Door, Notch, and T-Slot.

explore new materials like zirconia and cordierite to assess the impact of less understood materials on joining behavior. While Alumina is a very commonly studied and mature material, zirconia and cordierite are much more experimental and may not have the same reproduceable shrinkage, post-curing, and sintering morphology. Understanding joint behavior with these materials will allow for a more robust understanding of the effect of joint geometry on strength as well as allow for broader impacts of this work in the additive manufacturing field.

References:

[1] Chen, Z., Li, Z., Li, J., Liu, L., Zhao, G., and Li, Y. (2019). 3D printing of ceramics: A review. Journal of the European Ceramic Society, 39(4), 661-687. Yu, X.,

[2] Wang, Z., et al. (2024). Additive manufacturing and joining double processes of ceramic-resin green bodies using a single- or double-phase photocuring slurry. Ceramics International, 50, 14088-14100. Available online 24 Feb 2024. https://doi.org/10.1016/j.ceramint.2024.01.292

Fabrication and Characterization of High-Resistivity Silicon Interposers

CNF Summer Student: Gannon Lemaster
Student Affiliation: Electrical Engineering, Brown University

Summer Program(s): 2024 Cornell NanoScale Science & Technology Facility Research Experiences for Undergraduates (CNF REU) Program

Principal Investigator(s): James Hwang, School of Electrical and Computer Engineering, Department of Materials Science and Engineering; Cornell University

Mentor(s): Xiaopeng Wang, Yunjiang Ding, School of Electrical and Computer Engineering, Department of Materials Science and Engineering; Cornell University

Primary Source(s) of Research Funding: National Science Foundation under Grant No. NNCI-2025233

Contact: gannon_lemaster@brown.edu, jch263@cornell.edu, xw569@cornell.edu, yd439@cornell.edu

Summer Program Website: https://cnf.cornell.edu/education/reu/2024

Primary CNF Tools Used: ABM Contact Aligner, SÜSS Contact Aligner, AJA Sputter 1 and 2, AJA Ion Mill, Unaxis 770 Deep Si Etcher, Zeiss Ultra SEM, Zygo Optical Profilometer, Glen 1000 Resist Strip, Veeco Savannah ALD, DC Probe Station, Microwave Small-Signal Probe Station

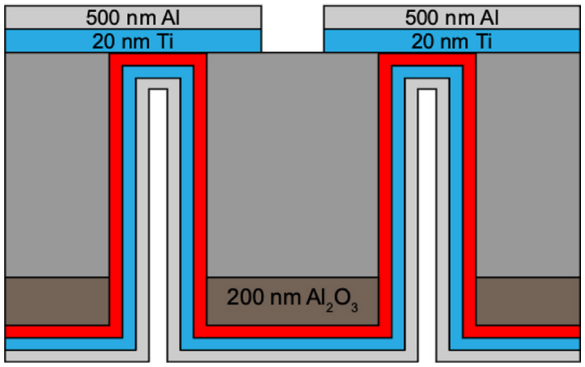

Figure 1: Cross-sectional geometry of through-silicon vias.

Abstract:

A recent focus of advancement in semiconductor technology involves the heterogeneous integration of chiplets on an interposer. Typically, the interposer is made of polymers, glass, or doped silicon. This work explores high-resistivity (HR, $\rho > 1$ kΩ·cm) silicon interposers fabricated at the Cornell NanoScale Facility for millimeter-wave applications. The most critical process is the etching and metallization of through-silicon vias (TSVs). The cross-sectional geometry of a TSV is shown in Figure 1.

Using aluminum oxide (Al_2O_3) as a backside hard mask and a frontside layer of titanium as an etch stop layer, 155 μm deep silicon etching was successfully carried out with the Unaxis 770 Deep Silicon Etcher using the SF_6/C_4F_8 Bosch Process. Subsequently, using an argon beam operating at 600 V and 295 mA with a vacuum of 10^{-8} torr, the frontside titanium layer was ion milled with a removal rate of 27 nm/s for 50 μm diameter TSVs. The TSVs were then metalized with a layer of platinum deposited using atomic layer deposition and sputtered titanium and aluminum, resulting in a series resistance of 2.5 Ω.

The TSVs were also patterned for RF characterization to form grounded coplanar waveguides (GCPWs). The GCPWs were probed up to 40 GHz, resulting in an insertion loss of 2 dB/mm and a return loss of 26 dB at 40 GHz.

Summary of Research:

The fabrication process began by adapting a previously verified method for creating substrate integrated waveguides (SIWs) on silicon carbide and applying it to a doped silicon substrate. This process flow involved distinct frontside and backside processes: the frontside process produced structures necessary for interconnects, such as microstrip and coplanar transmission lines, while the backside process formed the geometry of the TSVs. The electrical testing results obtained from this initial set of samples were quite poor, with TSVs exhibiting non-ohmic characteristics.

It was hypothesized that this issue stemmed from inadequate etching through the frontside aluminum oxide or inadequate metallization of the TSVs. For future samples, the fabrication process was adjusted by varying the incident angle and duration of the ion milling process, as well as the thickness of the platinum seeding layer for TSV metallization by atomic layer deposition (ALD). These adjustments resulted in an ohmic IV curve but with a significantly high TSV resistance of 14 ohms. Etching through the frontside aluminum oxide hard mask layer proved time-consuming and inconsistent, leading to the decision to remove the layer entirely with future samples.

Testing on these subsequent samples showed that Bosch etching through the silicon substrate and ion milling through the frontside titanium layer yielded better TSV resistance and uniformity. These samples were analyzed using the Microwave Small-Signal Probe Station at frequencies up to 40 GHz.

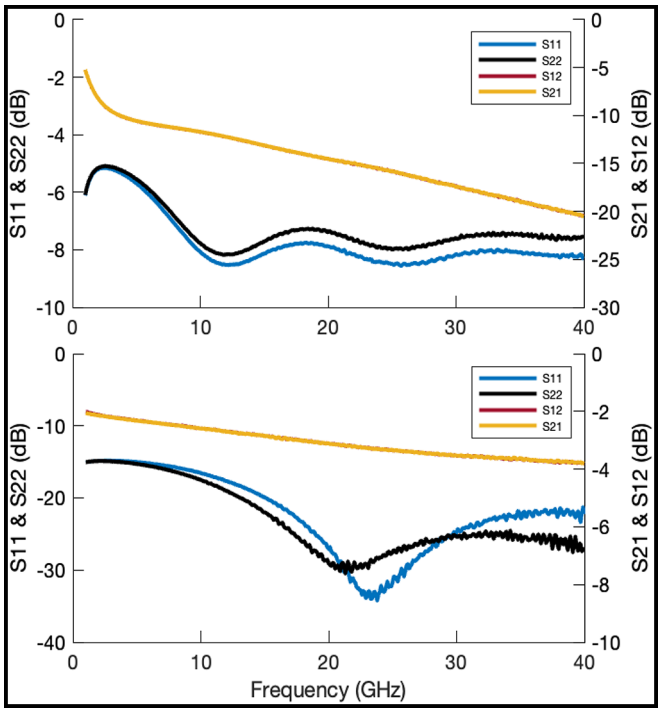

Figure 2: S-Parameters of 2146 μm GCPW test structures for doped silicon (above) and high-resistivity silicon (below) up to 40 GHz.

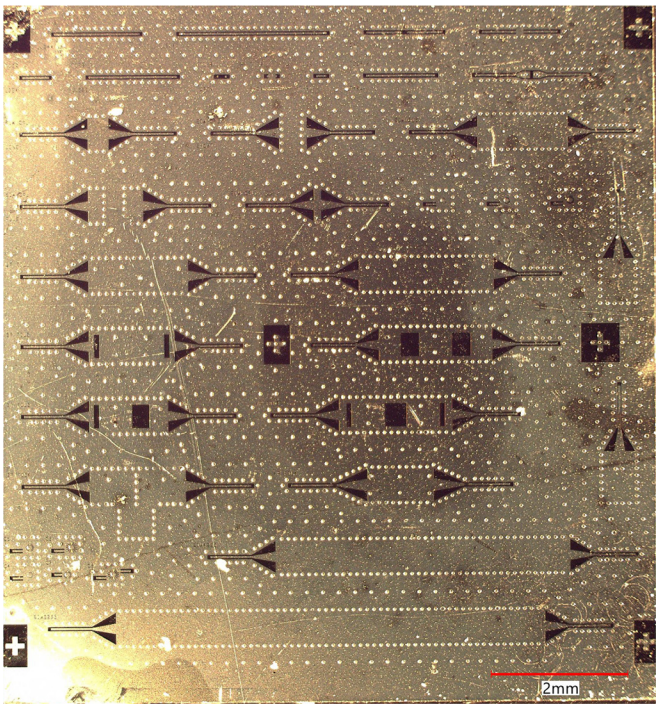

Figure 3: High-resistivity silicon sample, displaying frontside interconnect structures and backside TSVs.

A 10 dB/mm insertion loss was observed with a 2146 μm grounded coplanar waveguide (GCPW), with consistent results across various samples and GCPW lengths. After the electrical characterization, the samples were cleaved to capture cross-sectional scanning electron microscope (SEM) images. The TSV dimensions observed in the SEM images were consistent with optical profilometer images taken earlier in the fabrication process and confirmed the successful sputtering of aluminum. This finalized procedure was then transferred from a doped silicon substrate to a high-resistivity silicon substrate. Electrical characterization of this sample yielded a TSV resistance of 2.5 ohms, with subsequent measurements using a 2146 μm GCPW indicating an insertion loss of 2 dB/mm and a return loss of 26 dB.

Conclusions and Future Steps:

A complete process flow for the fabrication of high-quality TSVs for use on doped silicon and high-resistivity silicon interposers has been developed and verified. However, a TSV resistance of less than 1 ohm remains to be achieved for a high-resistivity silicon sample. Moreover, the insertion loss of the fabricated high-resistivity silicon GCPWs is too high, making them unsuitable for effective use within their intended frequency range, the D-band (110-170 GHz). It is theorized that this is due to an insufficient amount of frontside aluminum, which was sputtered at a thinner thickness than anticipated.

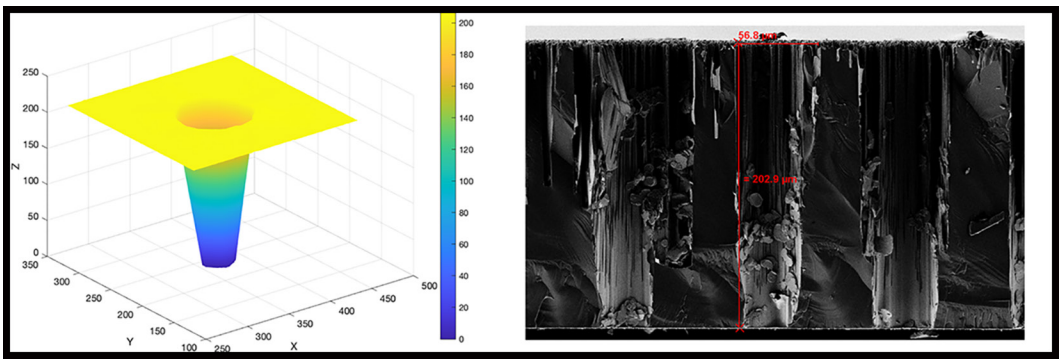

Figure 4: Optical profilometry image of TSV after through-substrate etching (left) and cross-sectional SEM of TSV (right).

Acknowledgments:

I would like to acknowledge the National Science Foundation (NSF) grant no. NNCI-2025233, the National Nanotechnology Coordinated Infrastructure (NNCI), and the Cornell NanoScale Facility for funding and curating the Research Experiences for Undergraduates (CNF REU) opportunity. Additionally, I would like to acknowledge and thank Yunjiang Ding, Xiaopeng Wang, and James Hwang for their invaluable guidance and support.

Atomic Layer Deposition of High-K Dielectrics

CNF Summer Student: Sarah Levine
Student Affiliation: Civil Engineering, Worcester Polytechnic Institute

Summer Program(s): 2024 Xing Army Educational Outreach Program (AEOP), 2024 Cornell NanoScale Facility Research Experiences for Undergraduates (CNF REU) Program

Principal Investigator(s): Prof. Huili (Grace) Xing, ECE and MSE, Cornell University

Mentor(s): Jeremy Clark, Cornell NanoScale Science and Technology Facility, Cornell University

Primary Source(s) of Research Funding: 2024 Xing Army Educational Outreach Program (AEOP), National Science Foundation under Grant No. NNCI-2025233

Contact: sjlevine@wpi.edu, grace.xing@cornell.edu, clark@cnf.conrell.edu

Summer Program Website: https://cnf.cornell.edu/education/reu/2024

Primary CNF Tools Used: Arradiance ALD Gemstar-6, AJA Sputter -2, SC4500 Odd-Hour Evaporator, Woollam RC2 Spectroscopic Ellipsometer, Hamatech Hot Piranha, Oxford 81/82 Etcher, Everbeing EB-6 Probe Station with Keithley SMU, Rapid Thermal Anneal -AG Associates Model 610

Abstract:

To keep making the world's most powerful central processing units faster and more energy-efficient dielectrics are used to increase the capacitance of these devices. Conventional HfO_2-based high-K dielectrics gate stacks cannot produce such a small effective oxide thickness and the consequent high capacitance without removing the interfacial SiO_2, which negatively impacts electron transport and gate leakage current. The superlattice gate stacks offer much-reduced leakage current and zero mobility deterioration as they lack the need for this kind of scavenging. The gate stacks are used in GaN transistors for power and communication, the existing dielectric in these transistors causes significant leakage and damages the underlying material. Ultrathin ferroic HfO_2-ZrO_2 multilayers, stabilized with competing ferroelectric-antiferroelectric order, offer a new method for advanced gate oxide stacks in electronic devices beyond traditional HfO_2-based high-dielectric-constant materials. The project aims to develop a process to deposit the high-K HfO_2/ZrO_2 superlattices whose new layers will help lower charge leakage. Atomic Layer Deposition (ALD) is used to build up the superlattice, we use ALD because it provides uniform and precisely tuned thickness, then through various depositing methods such as sputtering and e-beam evaporation aluminum was deposited through a capacitor shadow mask and then annealed through rapid thermal processing. The fabricated devices were characterized on a DC probe station and graphed for Capacitance-Voltage (C-V), to solve for the dielectric constant, also known as K, and also examine other material parameters such as defect density. The project works towards the smallest leakage at the smallest equivalent oxide thickness.

Summary of Research:

In capacitors, a tried and tested industry dielectric is SiO_2, which has a dielectric constant of 3.9. HfO_2 has become a forefront dielectric in the past few years with a dielectric constant between 18 and 25. The issue with this is that the smaller you make these capacitors, the higher the chance for electron leakage. The proposed HfO_2/ZrO_2 superlattice has new added layers that should help prevent such leakage and allow for a higher dielectric constant to be obtained. The goal is to be able to achieve smaller equivalent oxide thicknesses and keep leakage down.

The main part of this research has been to develop a process flow to deposit these high-K dielectric HfO_2/ZrO_2 superlattice devices. The first step in this process was to perform a hot piranha etch to get rid of any lingering organic material on the N-type silicon substrate. Next was to deposit the superlattice on the silicon substrate through Atomic Layer Deposition, which allowed for layer-by-layer deposition with increased control over thickness and composition at a relatively low growth temperature, which for this superlattice was 200°C. To determine the amount of loops used for each precursor ellipsometry was done to determine how much deposition was laid down with 300 loops. It was determined that 11 loops of ZrO_2 would be about equivalent to 1.2 nm whereas three loops of HfO_2 is about equivalent to 0.4 nm.

The next step in the process was to deposit aluminum and metalize the capacitor. This was done either through sputtering or e-beam evaporation. The sputtering while giving an incredibly uniform coating emits X-rays as a consequence of using plasma which can damage the sample. The evaporator was unable to provide that same guaranteed uniformity, but aluminum has such a relatively low evaporation rate that the silicon substrate isn't as harmed by any x-rays emitted from e-beam evaporation.

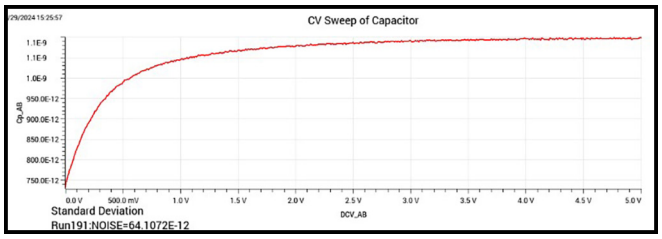

Figure 1: A CV sweep of a HfO_2 capacitor of voltage over capacitance in farads.

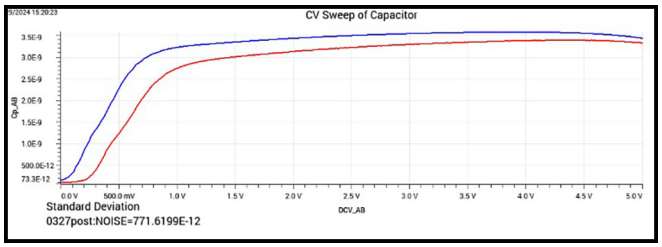

Figure 2: A CV Sweep of the capacitor of voltage over capacitance in farads. These graphs were used to determine the K dielectric of the capacitor. This particular sweep is of the Period x4 made on the evaporator, the red line is the pre-annealed data and the blue is the post-annealed.

Period, Aluminum Deposition Method	Pre-Annealing Dielectric Constant	Post Annealing Dielectric Constant
x 1, Sputter	1.65	2.63
x 1, Evaporator	1.34	2.25
x 2, Sputter	1.13	2.83
x 2, Evaporator	3.37	3.25
x 4, Sputter	7.03	8.61
x 4, Evaporator	7.16	7.56
x 8, Sputter	11.30	11.12
x 8, Evaporator	11.27	9.66
x 12, Sputter	15.08	14.74
x 12, Evaporator	12.19	12.57

Figure 3: A chart of the different periods of pre-annealed and post-annealed dielectric constants.

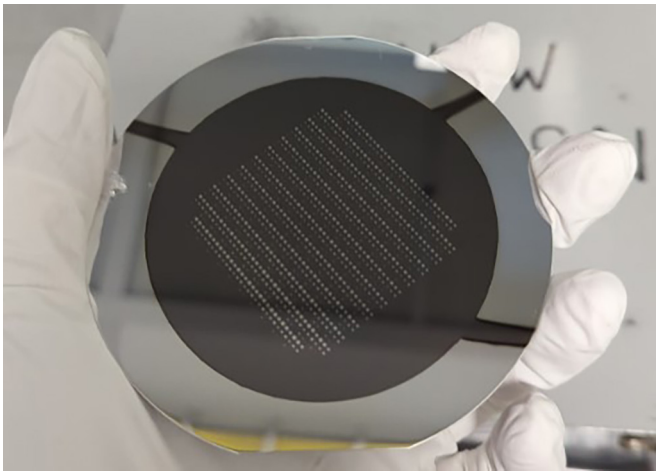

Figure 4: One of the wafers Levine fabricated through sputtering.

When depositing the superlattice residual deposition also ends up on the back side of the wafer, to remove this reactive ion etching, specifically a CF_4 etch, is used. To protect the capacitors, a clean silicon wafer was placed over the capacitors to not allow any CF_4 to etch off the needed dielectric. Aluminum is then deposited onto the back to improve overall contact resistance and thermal conduction.

The final step in the fabrication process is to perform rapid thermal annealing (RTA) using N_2 at 200°C for one minute. Characterization of these capacitors was done on a DC probe station and a Capacitance-Voltage (C-V) test was conducted. To test the C-V sweep and confirm our equation,

$$C = \frac{k\epsilon_0 A}{d}$$

solving for k, a sweep with HfO_2 as the dielectric was done resulting in pre-annealed data of 17.7. The graph for this data is shown in Figure 1, which is on the lower end of the expected dielectric constant range which confirmed the test being done.

Conclusions and Future Steps:

The data collected from the Capacitance-Voltage graphs, shown in Figure 3, showed the expected decrease in the dielectric constant as film thickness also decreased. Figure 2 shows what a graph of pre- and post-annealed date would look like for this C-V sweep. In the post-anneal data, it showed an increase in the dielectric constant for the thinner films after being annealed.

Future work on this project will be to take the superlattice and confirm the thicknesses through X-ray reflectivity (XRR) measurements and that will also ensure the ALD recipe is producing the film growth at the expected rate. Another step that could be taken to ensure the best dielectric constant is to etch the native oxide layer. Looking at higher annealing temperatures would be another variable that could increase the dielectric constant. Measuring the capacitors on different graphs such as doing a SMU-Sweep to characterize current versus voltage for leakage measurements.

Acknowledgements:

I would like to express my appreciation to my Principal Investigator Professor Grace (Huili) Xing, the Jena-Xing Group, and my mentor Jeremy Clark. This project would have been unsuccessful without their guidance. This work was performed at the Cornell NanoScale Facility, an NNCI member supported by NSF Grant NNCI-2025233, via the 2024 Xing Army Educational Outreach Program (AEOP).

Investigating the Lateral Spreading of Vanadium-Based Ohmic Contacts

CNF Summer Student: Fabiana P. Mayol López
Student Affiliation: Department of Natural Sciences, Ana G. Méndez University, Gurabo Campus

Summer Program(s): 2024 Cornell NanoScale Science & Technology Facility Research Experiences for Undergraduates (CNF REU) Program

Principal Investigator(s): Prof. Huili (Grace) Xing, ECE and MSE, Cornell University

Mentor(s): Joseph Dill, Department of AEP, Cornell University; Shivali Agrawal Department of CBE, Cornell University; Xianzhi Wei, Department of MSE, Cornell University

Primary Source(s) of Research Funding: National Science Foundation under Grant No. NNCI-2025233

Contact: anapao73@outlook.com, hgx2@cornell.edu, jed296@cornell.edu, sa2368@cornell.edu, xw694@cornell.edu

Summer Program Website: https://cnf.cornell.edu/educatison/reu/2024

Primary CNF Tools Used: SC4500 Odd-Hour Evaporator, Zeiss Supra Scanning Electron Microscope, Bruker Quantax 200 Energy Dispersive X-Ray Spectroscopy (EDS), GCA AS200 i-line Stepper, Glen 1000 Resist Strip, RTA-AG610b

Abstract:

Aluminum gallium nitride (AlGaN) is a material of interest for the development of UV-emitting photonic devices. Vanadium-based metal stacks are a popular means of forming ohmic contacts to n-type AlGaN. However, these metal stacks must be annealed to temperatures above 600°C [6] for VN to form during which the metals in the ohmic contact stack can spread laterally and short patterned devices. The aim of this study is to determine the annealing conditions that minimize the lateral spreading of V/Al/Ni/Au stacks and investigate the behavior of these stacks under annealing. Metal stacks were patterned on 8 × 8 mm silicon (Si) pieces and annealed for different temperatures and times. A "safe zone" of annealing conditions that didn't short the devices was determined. The amount of spreading was determined from scanning electron microscope (SEM) images of C-TLM structures. We also observed a "balling up" of the Ni under annealing, likely due to its high surface energy. This observation motivates switching Ni to a metal with a lower surface energy in future studies.

Summary of Research:

Background. Since the first realization of the GaN blue LED in 1993 [1], research attention has been devoted to AlGaN-based light-emitting devices that would emit invisible UV light. Such devices would enable many novel technologies, including chemical-free sterilization of medical equipment and water purification [2]. One key challenge to this end is the formation of ohmic contacts to n-type AlGaN. Several studies have achieved low resistance contacts using annealed V/Al/X/Au metal stacks [6,7]. When annealed in N_2, V alloys with N to form VN on the surface, which has a work function of 3.55 [5]. The Al helps form donor-like N vacancies in the AlGaN, and Au prevents oxidation and provides a soft surface for electrical probing. X is the "diffusion barrier" metal, usually V or Ni. However, annealing these metal stacks often leads to strange and undesirable metallurgical effects, such as the formation of Ni domains [7].

Methods. Annealed metal pads were fabricated on 8 × 8 mm Si pieces as follows:

1. Si pieces were cleaned in acetone, isopropyl alcohol (IPA), and deionized water for five minutes each with sonication to remove any organic contamination from the surface.
2. Pieces were spin-coated with AZ nLOF 2020 negative photoresist and baked.
3. Circular transmission line method (C-TLM) patterns were exposed using the GCA AS200 i-line Stepper, followed by a post-exposure bake.
4. The pattern was developed in 726 MIF developer for 30 sec.
5. An ozone descum was performed to remove all residual undeveloped photoresist.
6. A metal stack of 20 nm of V, 80 nm of Al, 40 nm of Ni, and 100 nm of Au was deposited by electron-beam evaporation (see Figure 1).
7. Liftoff was performed by immersing the pieces in Microposit Remover 1165 and IPA with sonication.
8. Each sample was annealed in N_2 ambient. The anneal times and temperatures for each sample are shown in Figure 2a.

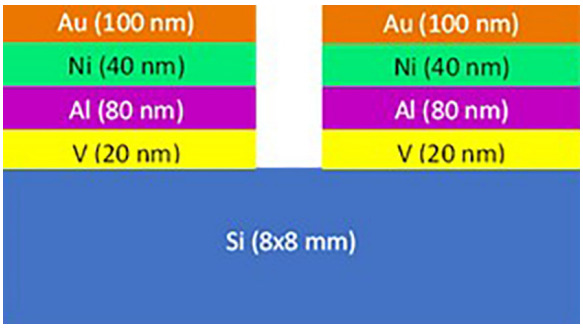

Figure 1: Cross-sectional view of sample.

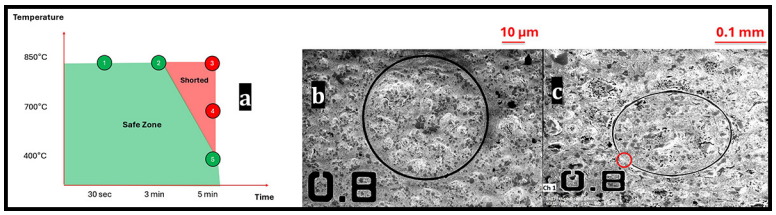

Figure 2: Plot of each annealed sample with temperature vs time annealed in (a). Post-anneal SEM images in (b) sample 1: 850°C, 30 seconds and (c) sample 3: 850°C, five minutes. Red circle indicates shorting the in the C-TLM pattern.

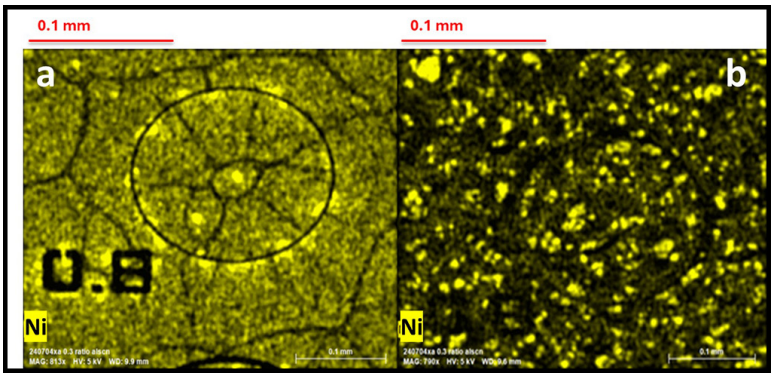

Figure 3: EDS map of Ni in (a) sample 5: 400°C, 5 minutes and (b) sample 3: 850°C, five minutes.

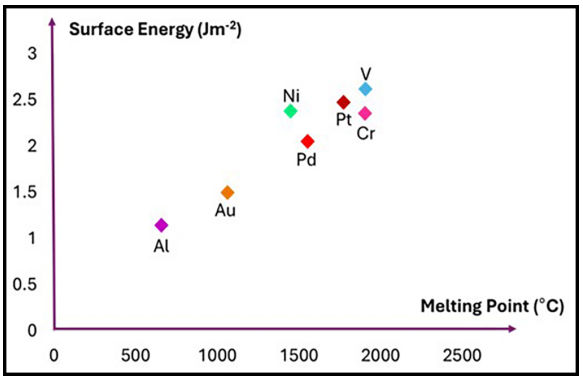

Figure 4: Plot of surface energy vs melting point. Values obtained from [4].

Results. Figures 2b and 2c show SEM images of a C-TLM structure with 0.8 μm spacing on samples 1 and 3, annealed at 850°C for 30 sec and 5 min, respectively. The red circle in 2c indicates a point where the C-TLM pad was shorted due to lateral spreading of the metal during annealing. The annealing conditions that did and didn't result in shorting of the 0.8 μm pattern are summarized in Figure 2a. The annealing conditions for samples 1, 2, and 5 establish a "safe zone" in which annealing didn't cause shorting.

The annealed samples were imaged with Electron Dispersive X-Ray Spectroscopy (EDS) to investigate the motion of the constituent metals in the stack during annealing. As seen in Figure 3, Ni was observed to coalesce, forming domains that decreased in size with increasing anneal temperature. In sample 5, annealed at 400°C for 5 minutes, ~ 40 μm-wide domains formed (see Figure 3a), and in sample 3, annealed at 850°C for 5 minutes, ~ 5 μm-wide domains formed (see Figure 3b). This is likely a result of nickel's high surface energy.

Conclusions and Future Steps:

During annealing, a metal can minimize its surface energy by forming a spherical shape rather than remaining flat. These spheres will be tighter at higher temperatures to minimize the additional thermal free energy. We observe the initial stages of this in Figure 3a wherein the Ni begins forming wide domains, presenting a "cracked" appearance. Ni's tendency to ball up during annealing is *used* by Shi, et al. to form Ni nanoparticles annealing sputtered Ni thin films [3].

Considering these findings, future ohmic contact stacks should utilize a diffusion barrier with a lower surface energy than Ni. The surface energies and melting points of V, Al, Ni, Au, and alternate diffusion barrier metals (Pd, Pt, Cr) are benchmarked in Figure 4. Of the candidate metals, Pd has the lowest surface energy. Future studies should also be conducted on AlGaN, rather than Si, such that the electrical performance of the ohmic contacts can be investigated in parallel with the metallurgical behavior under annealing.

Acknowledgements:

Special thanks to the Cornell NanoScale Science & Technology Facility Research Experiences for Undergraduates (CNF REU) Program for hosting this internship. I would like to express my appreciation for the Jena-Xing Group, my PI Prof. Grace Xing, my mentors Joseph Dill, Xianzhi Wei, and Shivali Agrawal for their support and guidance.

References:

[1] S. Nakamura, APL (1994).
[2] H. Amano, Jour. of Phys D (2020).
[3] Shi, Coatings, (2022).
[4] Vitos, Surface Science (1998).
[5] V. S. Fomenko, Handbook of Thermionic Properties (1966).
[6] R. France, APL 90(6) (2007).
[7] X. Guo, APL 124(23) (2024).

Micro-Scale Ceramic Additive Manufacturing for Aerospace Applications

CNF Summer Student: Elizabeth Quansah
Student Affiliation: Department of Materials Science & Engineering, University of Illinois at Urbana-Champaign

Summer Program(s): 2024 Cornell NanoScale Science & Technology Facility Research Experiences for Undergraduates (CNF REU) Program
Principal Investigator(s): Sadaf Sobhani, Department of Mechanical and Aerospace Engineering, Cornell University
Mentor(s): Giancarlo D'Orazio, Department of Mechanical and Aerospace Engineering, Cornell University
Primary Source(s) of Research Funding: National Science Foundation under Grant No. NNCI-2025233
Contact: elizaq99@gmail.com, sobhani@cornell.edu, gd373@cornell.edu
Summer Program Website: https://cnf.cornell.edu/education/reu/2024
Primary CNF Tools Used: Nanoscribe Photonic Professional GT2, Zeiss Ultra Scanning Electron Microscope

Abstract:

This paper suggests mechanisms for producing silica glass microscale electrospray emitters for spacecraft propulsion systems and prefaces the potential of these methods for producing microscale ceramics. The following research is conducted in an effort to replace tungsten needles currently used as emitters and explore micro-scale additive manufacturing. This work relies on two-photon photolithography for additive manufacturing green bodies that undergo thermal processing to produce silica glass, silicon carbide (SiC), or silicon oxycarbide (SiOC). GP Silica, a polymer-based resin containing glass nanoparticles, is converted into emitter-shaped green bodies using the Nanoscribe Photonic Professional GT2. Conversion of SiC and SiOC precursor resins into green bodies using the Nanoscribe is also attempted as in previous works [1-3], and the SiOC precursor exhibits success. Thermally processing green bodies is completed in an air furnace to produce glass and a microwave furnace to produce SiC and SiOC. Characterization of resulting structures suggests high potentials for additively manufacturing glass and thermally processing ceramics in the microwave furnace, although further optimizations remain necessary.

Summary of Research:

Additive manufacturing demonstrates increasing promise for device fabrication, making identifying technological limitations of interest. The Nanoscribe Photonic Professional GT2, a micro-additive manufacturing technology utilizing two-photon photolithography, fires a 780 nm femtosecond laser that is re-emitted at 390 nm after striking a molecule within the resin it is printing with. This provides sufficient energy to cure the resin. This paper explores the Nanoscribe's ability to micro-additively manufacture green bodies for thermal processing to make silica glass, silicon carbide (SiC), and silicon oxycarbide (SiOC).

GP Silica is a polymer-based resin containing glass nanoparticles. Developing emitter green bodies with this resin requires optimizing print parameters using the 10X large feature objective. This was completed by printing a 4 × 4 array of 150 μm cubes on a silicon substrate. Scan speed varied along one axis and laser power along the other. 60% laser power and 80,000 μm/s scan speed produced the smoothest edges and fewest bubbles.

The array was placed in a Nabertherm air furnace for thermal processing according to NanoGuide's standard curve [4], which peaks at 1300°C with three hour holds at 90°C, 150°C, 230°C, and 280°C. Following sintering, the array was imaged under the scanning electron microscope (SEM), revealing that 14/16 cubes survived, 12 of which were smooth without cracks or bubbles (Figure 1).

Due to this success, solid glass emitters with a 1000 μm base, 700 μm height, and 20° cone angle were attempted using the same process (Figure 2). Many emitters survived, although deformed, as signified by an estimated 55% shrinkage instead of the expected 30%. Next, a new batch of solid emitters and emitters with porous exteriors were printed and heated for 20 hours in the air furnace according to NanoGuide's fast curve [4], which ramps to 1300°C at 180°C/hr, saving approximately 40 hours compared to the standard curve. These emitters were more successful, as demonstrated by an estimated 24% shrinkage (Figure 3).

To determine whether a similar process is possible for producing SiC and SiOC emitters, SiC and SiOC precursor resins were developed for printing on the Nanoscribe with 63X oil immersion on glass substrates. Starfire SMP-10 and Starfire SPR-688 were homogenized into resins by mixing in 1%/wt 2-Isopropylthioxanthone and 9%/wt 1,6-Hexanediol diacrylate. Attempting to print with the SiC precursor Starfire SMP-10 based resin using a 10,000 μm/s scan speed with laser power ranging from 30% to 80%, as well as a 20,000 μm/s scan speed with 70% and 80% laser power produced no parts due to the resin's low viscosity. Significant motion during printing prevented proper curing and substrate adhesion. When printing with the SiOC precursor Starfire SPR-688 based resin, bubbling occurred at laser powers above 50%

with a 10,000 μm/s scan speed, suggesting that printing is possible with the SiOC precursor but not the SiC precursor for the formulations and settings tested.

Lastly, the microwave furnace, an alumina crucible lined with SiC within a 1 kW microwave that ramps at 150°C/min, was evaluated for thermal processing ceramics. SiC precursor Starfire SMP-10 cured at 200°C and SiOC precursor Starfire SPR-688 cured at 445°C were placed into the microwave furnace independently for 2, 3, 4, and 5 minutes. Examining 4-minute thermally converted SiC precursor optically and using the SEM revealed consistency with SiC and an amorphous silicate phase. Similarly, 3-minute thermally converted SiOC precursor appeared consistent with SiOC after optical examination.

Conclusions and Future Steps:

In conclusion, GP Silica is useful for micro-additively manufacturing glass emitters with the Nanoscribe. The fast heating curve [4] proves effective as demonstrated by the emitters' 24% shrinkage. Additionally, printing was achieved with the SiOC precursor resin, but not the SiC precursor resin. Finally, the microwave furnace may present an option for sintering ceramics, but further research is required. In the future, optimizing thermal processing glass emitters and developing emitters using the SiOC precursor resin is necessary, along with testing this process with a more viscous SiC precursor resin.

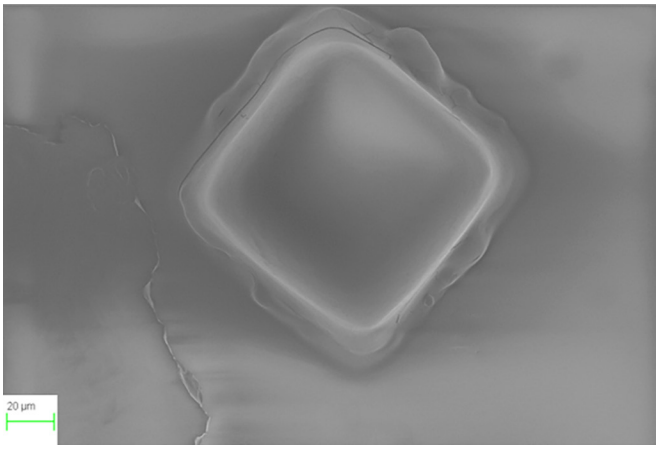

Figure 1: A successful glass cube has a smooth surface without cracks and bubbles.

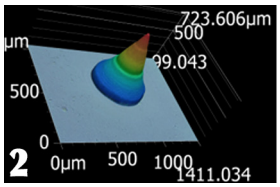

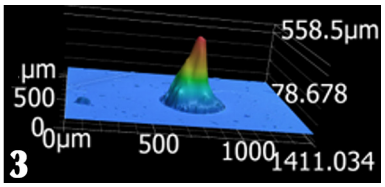

Figure 2, left: Shown here is a Keyence image of a GP Silica solid emitter green body. Figure 3, right: Depicted is a Keyence image of a solid glass emitter.

Figure 4: The alumina crucible is lined with SiC and goes inside of a 1 kW microwave.

Acknowledgements:

Many thanks to the Cornell NanoScale Science & Technology Facility Research Experiences for Undergraduates Program of the National Nanotechnology Coordinated Infrastructure funded by National Science Foundation grant no. NNCI-2025233. Special thanks to Sadaf Sobhani, Giancarlo D'Orazio, Giovanni Sartorello, and Melanie-Claire Mallison for their guidance.

References:

[1] J. Bauer, et al., "Additive manufacturing of ductile, Ultrastrong polymer-derived nanoceramics," Matter, vol. 1, no. 6, pp. 1547-1556, Dec. 2019. doi:10.1016/j.matt.2019.09.009.

[2] G. Konstantinou, et al., "Additive micro-manufacturing of crack-free PDCS by two-photon polymerization of a single, low-shrinkage Preceramic Resin," Additive Manufacturing, vol. 35, p. 101343, Oct. 2020. doi:10.1016/j.addma.2020.101343.

[3] L. Brigo et al, "3D Nanofabrication of SiOC Ceramic Structures," Advanced Science, vol. 5, (12), 2018/12//. Available: https://www.proquest.com/scholarly-journals/3d-nanofabrication-sioc-ceramic-structures/docview/2262718647/se-2.

[4] NanoGuide Professional Photonic Series. (n.d.). Retrieved July 8, 2024, from https://support.nanoscribe.com/hc/en-gb/articles/4402084033810-Printing-with-the-Glass-Printing-Explorer-Set-GP-Silica.

Nanomolding of Topological Materials for Interconnects

CNF Summer Student: Richard A. Remias
Student Affiliation: Physics, University of Rhode Island

Summer Program(s): 2024 Cornell NanoScale Science & Technology Facility Research Experiences for Undergraduates (CNF REU) Program
Principal Investigator(s): Judy Cha, Materials Science and Engineering, Cornell University
Mentor(s): Quynh Sam, Khoan Duong; Materials Science and Engineering, Cornell University
Primary Source(s) of Research Funding: National Science Foundation under Grant No. NNCI-2025233
Contact: riskoalbi@live.com, jc476@cornell.edu, qps2@cornell.edu, nd399@cornell.edu
Summer Program Website: https://cnf.cornell.edu/education/reu/2024
Primary CNF Tools Used: Oxford FlexAl ALD, Zeiss Supra SEM, Bruker EDX, Veeco Icon AFM, Woollam RC2 Ellipsometer

Abstract:

The increasing resistivity of copper (Cu) interconnects with decreasing dimensions poses many challenges for the continued downscaling of integrated circuits and computer chips. At the nanoscale, electron scattering at grain boundaries and surfaces of the interconnects causes an increase in resistivity leading to higher energy consumption and signal delay in computer chips. Conversely, topological materials may show decreasing resistivity with decreasing size at nanoscale dimensions due to their topologically protected band structures that are predicted to suppress electron scattering. Thus, transport studies of topological materials at the nanoscale are critical to find alternative metals to Cu interconnects. Nevertheless, current nanowire synthesis methods such as molecular beam epitaxy (MBE) and chemical vapor transport (CVT) struggle to create uniformly sized nanowires. We use nanomolding to fabricate nanowires of topological materials, where a bulk material is pressed into a porous anodic aluminum oxide (AAO) mold to create high aspect ratio nanowires. To promote more facile nanomolding and to prevent oxidation of the molded nanowires, we coat the AAO mold pore walls with a thin film of aluminum nitride (AlN) and tantalum nitride (TaN). The CNF's Oxford FlexAl atomic layer deposition (ALD) tool is used to deposit precise and uniform films due to its self-limiting reactions. Through energy dispersive X-ray spectroscopy (EDX), we determine the infiltration depth of AlN in our pores. Additionally, InBi is a topological material which may exhibit interesting quantum properties at few-layer thicknesses. We use nanomolding to compress InBi into thin flakes by encapsulating the InBi with hexagonal boron nitride (hBN). The CNF's AFM Veeco Icon tool is used to determine the resulting thickness of the InBi flake.

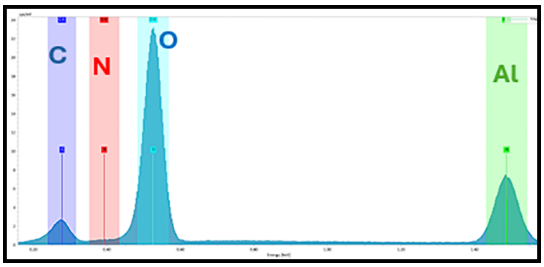

Figure 1: Cross-sectional EDX Spectrum of AAO Channels Post AlN ALD.

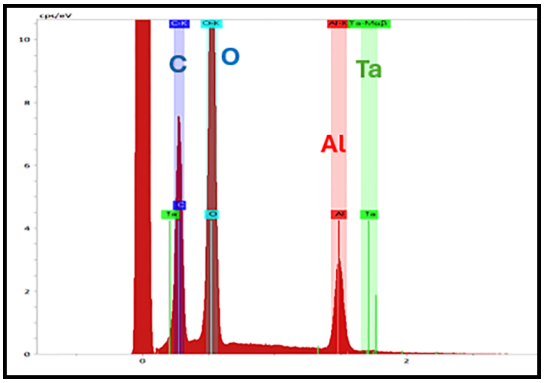

Figure 2: Cross-sectional EDX Spectrum of AAO Channels Post TaN ALD.

Summary of Research:

ALD was first used to deposit 20 nm of AlN onto the AAO mold which had a pore diameter of 120 nm. This deposition was done at 400°C for 334 cycles at 0.6Å/cycle, using trimethylaluminum (TMA) and H_2/N_2 plasma as precursors. These precursors were pulsed for 0.02 seconds and 5 seconds, respectively. To estimate deposition thickness, a blank silicon substrate was placed next to the mold in the ALD chamber and ellipsometry was used to determine the thickness of AlN deposited

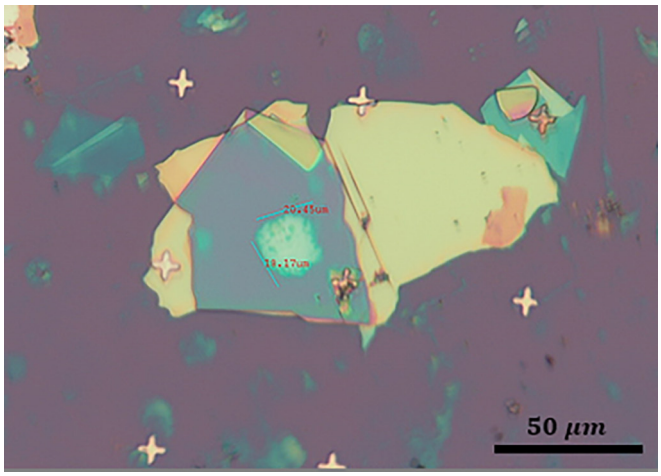

Figure 3: Optical Microscope Image of Compressed InBi Stack.

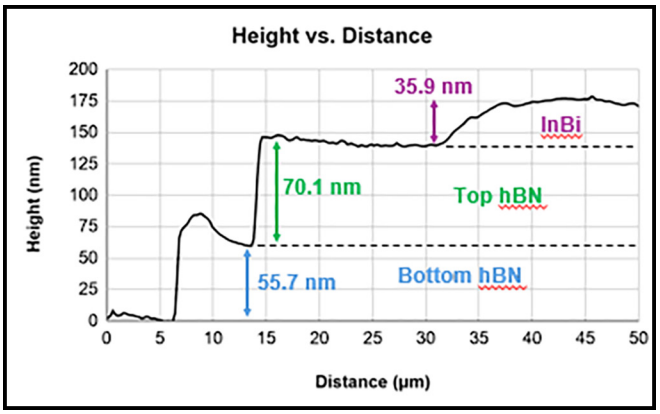

Figure 4: AFM Line Profile Graph of Compressed InBi Stack.

onto the substrate. The resulting thickness was estimated to be about 18.02 ± 0.027 nm. A scanning electron microscope (SEM) was then used to take a cross-sectional image of the AAO mold which was combined with EDX to map the elements deposited within the mold channel walls. However, due to low film thickness and low atomic weight of nitrogen, the infiltration depth of AlN in our pores was inconclusive as no nitrogen was detected on the pore walls (Figure 1).

Next, we used ALD to deposit 10 nm of TaN onto a mold of identical pore diameter. This deposition was done at 250°C for 250 cycles at 0.4 Å/cycle, using tris(diethylamido)(tert-butylimido)tantalum(V), or TBTDET, and ammonia (NH3) as precursors. The pulse time for these precursors was 6 seconds and 15 seconds, respectively. The same method was used to estimate the deposited film thickness, which was determined to be 6.87 ± 0.081 nm. SEM was used to take a cross-sectional image and EDX was used for element mapping. Unfortunately, no tantalum was detected in the pores so the infiltration depth of TaN is inconclusive (Figure 2). Through improvements in ALD parameters, we may be able to determine infiltration depth using EDX.

Additionally, we used nanomolding to press InBi into thin flakes. This was done by placing an hBN flake both on top of and underneath the InBi piece to create an hBN-InBi-hBN stack. The stack was made using tape exfoliation and the desired flakes of uniform thickness were found under a microscope and transferred using a glass slide with an epoxy drop. We used a hot press to compress the InBi stack at 80°C for 15 minutes. The resulting stack is shown in Figure 3.

To determine the final thickness, we used atomic force microscopy to create a line profile over the stack. We measured the thickness of InBi to be 35.9 nm (Figure 4). Different nanomolding parameters were also used on different stacks, such as pressing for 30 minutes at 100°C, however, no flakes were pressed to be thinner than 35.9 nm.

Conclusions and Future Steps:

EDX results after deposition of AlN and TaN show that a more sensitive elemental mapping method may be needed for accurate determination of infiltration depth into AAO channel pores. A method such as X-ray photoelectron spectroscopy may be more sensitive to thinner films as well as lighter elements. Also, increasing precursor pulse time in ALD processes may allow more time for gases to travel into high aspect ratio features, increasing infiltration depth. Increasing gas flow rates may also prove useful as it will increase delivery of gases deeper into the pores.

Results also show that nanomolding can be used to create sub 40 nm thin InBi flakes. Future work would include removing the top hBN flake and testing the resistance of the InBi flake.

Acknowledgements:

This work was made possible by the Cornell NanoScale Facility and funded by the National Science Foundation via grant no. NNCI-2025233. Special thanks to Judy Cha, Quynh Sam, Khoan Duong, Sihun Lee, and Melanie-Claire Mallison for their great help and guidance.

References:

[1] Chen, L., Wu, A.X., Tulu, N., et al. Exceptional electronic transport and quantum oscillations in thin bismuth crystals grown inside van der Waals materials. Nat. Mater. 23, 741-746 (2024). https://doi.org/10.1038/s41563-024-01894-0.

[2] Kiani, M. T., Sam, Q. P., Jin, G., Pamuk, B., Han, H. J., Hart, J. L., Stauff, J., and Cha, J. J. (2023). Nanomolding of metastable Mo4P3. Matter, 6(6), 1894-1902. https://doi.org/10.1016/j.matt.2023.03.023.

Effect of Temperature on Particle Morphology Polymerized via Initiated Chemical Vapor Deposition in Liquid Crystal

CNF Summer Student: Imrie Ross
Student Affiliation: Biochemical Engineering, University of Georgia

Summer Program(s): 2024 Cornell Robert Frederick Smith School of Chemical and Biomolecular Engineering FMRG: Cyber (CBE FMRG: Cyber) Summer Program, 2024 Cornell NanoScale Science & Technology Facility Research Experiences for Undergraduates (CNF REU) Program

Principal Investigator(s): Dr. Nicholas Abbott, Dr. Rong Yang; Smith School of Chemical and Biomolecular Engineering, Cornell University

Mentor(s): Soumyamouli Pal, Shiqi Li; Smith School of Chemical and Biomolecular Engineering, Cornell University

Primary Source(s) of Research Funding: 2024 CBE FMRG: Cyber Summer Program, 2024 CNF REU Program via the National Science Foundation under Grant No. NNCI-2025233

Contact: icr32942@uga.edu, nla34@cornell.edu, ryang@cornell.edu, sp2476@cornell.edu, sl2869@cornell.edu

Summer Program Website: https://cnf.cornell.edu/education/reu/2024

Primary CNF Tool Used: Zeiss Supra Scanning Electron Microscope

Abstract:

The ability to create designed polymer particle shapes would greatly benefit many applications, including timed drug delivery and reconfigurable metamaterials because the polymer's intrinsic properties largely depend on the shape. Prior works from our research group have leveraged the use of an anisotropic medium, namely liquid crystals (LCs), as templates to direct the growth of polymer structures by initiated chemical vapor deposition (iCVD) [1]. In this work, we have successfully obtained a range of glycidyl methacrylate (GMA) and divinyl benzene (DVB) polymer morphologies in a one-step, one-pot polymerization process by iCVD in a nematic LC called E7 (a eutectic mixture of cyanobiphenyls). We established multiple substrate temperatures in a single polymerization run by leveraging a temperature gradient placed directly on a cooled reactor stage. A filament array above the stage radially and thermally heats the gradient, providing lower temperatures as the distance from the gradient to the filament increases. E7 has a nematic to isotropic phase transition temperature of ~ 60°C, above, which the orientational order of the LC mesogens no longer exists. We have investigated the effect of temperature on the rate of evaporation and phase change of the LC by utilizing a brightfield and cross-polarized optical microscope placed directly over the reactor for *in-situ* monitoring. Using a set of controls and experiments, we have mapped a set of reactor conditions where temperature solely influences the progression of particle morphology, allowing us to study how the morphology varies with temperature. These conditions limit the amount of evaporation and prevent isotropic phase change of the LC. Structural characterization using the CNF Zeiss SEM reveals the formation of different particle morphologies as a function of the various temperatures achieved.

Summary of Research:

Micro and nanoparticles are promising for future imaging, medical, and energy applications. The ability to synthesize and control the size and morphologies is crucial for utilizing these particles at an industrial scale. Initiated chemical vapor deposition (iCVD) is a promising technique for synthesizing nanoparticles since it allows for high control of continuous polymerization and provides multiple particle morphologies without external manipulation. We utilized liquid crystals (LCs) as an anisotropic medium to provide a template for the iCVD polymerization and to optically monitor the polymerization *in-situ* using a long-distance focal lens. Our work focused on determining the effect of temperature on the morphology of glycidyl methacrylate (GMA) and divinyl benzene (DVB) polymeric particles polymerized using the iCVD-in-LC system.

Utilizing a temperature gradient placed in the iCVD reactor, we achieved multiple temperatures within one polymerization run, as shown in Figure 1. The gradient was created by stacking glass slides in a staircase fashion. The reactor stage was cooled using a chiller set at 5°C, and a heated filament array was set above the reactor stage, reaching ~ 260°C. Our custom-built staircase sample holder experiences higher temperatures at the top step and lower temperatures at the bottom. We mapped the top step and reactor stage temperatures and consistently achieved a temperature difference of 20-25°C between the two extremes. We achieved multiple temperatures during each reactor run by placing samples on different steps of the staircase sample holder. This allowed us to compare the morphologies of the GMA particles polymerized in LC at different temperatures while minimizing the variables that could contribute to morphological differences. LCs are

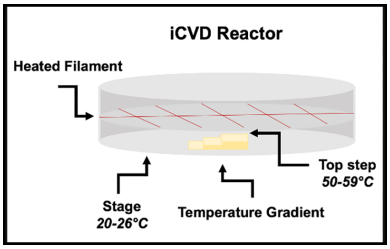

Figure 1: Schematic of the temperature gradient in the iCVD reactor.

sensitive to temperature and change phase as temperature increases. The LC nematic phase provides mesogen orientational order and is the iCVD polymerization target phase. As temperature increases, the LC mesogens will transition to the isotropic phase; at this point, the LC loses its order and does not provide a templating effect. E7 LC was used for this project and has a nematic to the isotropic phase transition of ~ 60°C. To ensure the E7 remained in the nematic phase, we monitored multiple steps on the staircase and found no phase change of LC in the samples placed on any step during 30-minute and 60-minute polymerizations.

We also utilized two surfaces for the iCVD reactions: nochromix-treated glass and octadecyltrichlorosilane (OTS) substrates. Cross-polarized optical images of the LC samples were taken before and after the polymerization. We found negligible evaporation and no phase change of the LC during the 60-minute polymerizations for both glass and OTS samples using the optical images and the long-distance lens placed directly above the reactor. However, an anchoring change was observed at the mid-range temperatures for OTS from homeotropic to planar/tilted LC anchoring. We are currently investigating the cause of the anchoring change. After the polymerization, we characterized the morphologies of the GMA particles using a Zeiss Supra scanning electron microscope. We found that the particle morphology for GMA particles on OTS and glass does not drastically change their morphology but instead becomes larger and more elongated, as shown in Figures 2 and 3.

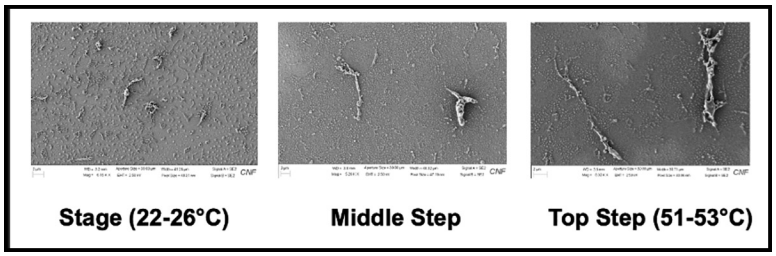

Figure 2: Morphologies of GMA particles polymerized on OTS.

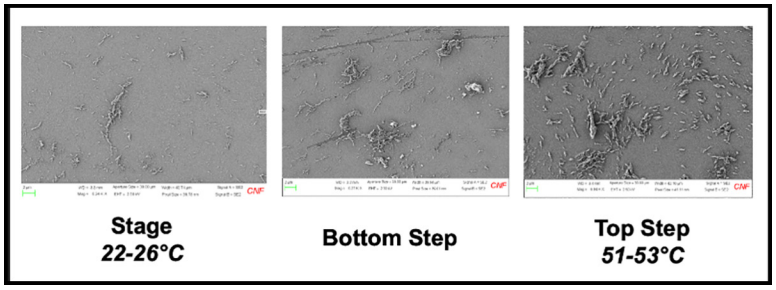

Figure 3: Morphologies of GMA particles polymerized on glass.

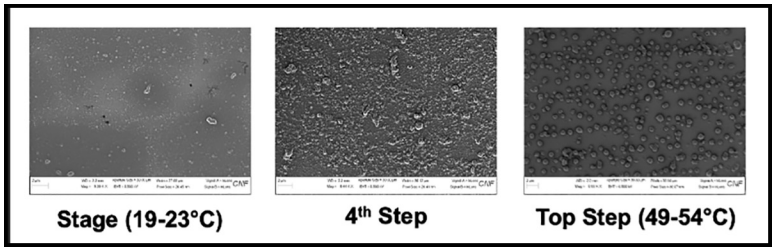

Figure 4: Morphologies of DVB particles polymerized on OTS.

Utilizing the temperature gradient, we also polymerized DVB particles on OTS. We found that DVB particle morphologies differ more significantly than GMA polymerized at similar temperatures, as shown in Figure 4. The lower temperatures provide 300-400 nm diameter DVB nanoparticles. As temperature increases, DVB particles become larger and less symmetrical; at higher temperatures, they become symmetrical microspheres 1 μm in diameter. We hypothesize that DVB can achieve more morphologies because of crosslinking, while GMA is linear, achieving fewer morphologies.

Conclusion and Future Steps:

Using a temperature gradient, we achieved multiple temperatures during a single LC-templated iCVD reactor run, allowing the comparison of GMA morphologies at different temperatures. We found that the GMA morphologies do not differ significantly with increasing temperature but increase in size and elongation. DVB particles were also polymerized using the temperature gradient, and the obtained morphologies changed more significantly. Reproducible reactor runs must be done to ensure the GMA particles are fully characterized at the different polymerization temperatures. The temperature gradient created for this project can also be used in future polymerizations to achieve multiple temperatures within a single polymerization.

Acknowledgments:

Thank you to CBE FMRG: Cyber and the CNF REU for all the funding and support I received during the 2024 summer. I also want to thank my mentors, Soumyamouli Pal and Shiqi Li, for their support and mentorship. Finally, thank you to my PIs, Dr. Abbott and Dr. Yang, for hosting me this summer and allowing me to work in their fantastic labs.

References:

[1] Jain, A., Pal, S., Abbott, N. L., and Yang, R. (2023, March 10). Single-step synthesis of shape-controlled polymeric particles using initiated chemical vapor deposition in liquid crystals.

Micro-Additive Manufacturing Processes for Electrochemical CO_2 Reduction

CNF Summer Student: Hunter Saylor
Student Affiliation: Electrical and Computer Engineering, Morgan State University

Summer Program(s): 2024 Cornell NanoScale Science & Technology Facility Research Experiences for Undergraduates Program with Morgan State University (CNF REU MSU)

Principal Investigator(s): Sadaf Sobhani, Mechanical and Aerospace Engineering, Cornell University

Mentor(s): Giancarlo D'Orazio, Mechanical and Aerospace Engineering. Cornell University

Program and Primary Source(s) of Research Funding: Cornell College of Engineering (CNF REU MSU), National Science Foundation under Grant No. NNCI-2025233 (CNF REU)

Contact: husay1@morgan.edu, sobhani@cornell.edu, gd373@cornell.edu

Summer Program Website: https://cnf.cornell.edu/education/reu/2024

Primary CNF Tools Used: Nanoscribe GT2, AJA Sputter, Zeiss Ultra SEM

Abstract:

This work investigates the application of micro-additive manufacturing in the development of gas diffusion electrodes (GDEs) for electrochemical CO_2 reduction reactors. This technology relies on the principles of electrochemistry to convert CO_2 into useful chemical products. A key focus of this work is the reactor design and fabrication, as these elements impact the overall efficiency and functionality of the system. The gas diffusion electrode is identified as a common failure point in such reactors. To enhance the performance and durability of the GDE, we utilize the Nanoscribe Photonic Professional GT2 two-photon lithography 3D printer to print a microporous layer atop a carbon paper electrode. This effort aims to mitigate electrolyte flooding in our vapor-fed reactor. A copper catalyst will be deposited onto the microporous layer using the AJA sputter system. Subsequent analysis of the GDE surface will be conducted using a scanning electron microscope (SEM) to ensure structural integrity and optimal surface characteristics. To evaluate the performance of the CO_2 reduction reactor, measurements of open-circuit potential, electrochemical impedance spectroscopy, and cyclic voltammetry will be scrutinized. The results will highlight common failure modes, such as catalyst delamination and electrolyte flooding. Additionally, a long-duration, steady-state test will be performed to measure changes in potential at a fixed current, providing insights into the long-term performance and lifespan of the GDE. Our findings will deliver quantitative insights into the optimization of gas diffusion electrode synthesis, advancing the efficiency of electrochemical CO_2 reduction processes. This research underscores the potential of micro-additive manufacturing in addressing critical challenges in renewable energy and carbon capture technologies.

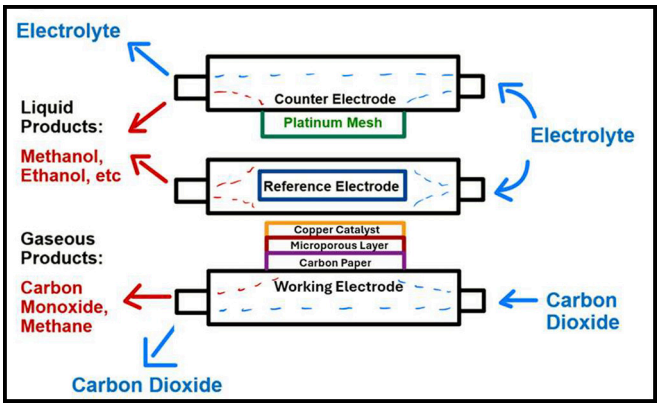

Figure 1: Diagram of CO_2 reduction reactor.

Summary of Research:

In the effort to optimize the fabrication and design of the CO_2 reduction reactor's Gas Diffusion Electrode (GDE), we addressed common failure modes such as catalyst degradation and flooding of the electrolyte into the vapor-fed reactor. To minimize these failure modes, we had to [1] characterize the reactor before and after long-duration trials, [2] design and print a microporous layer on the GDE, and [3] test the effect of electrolyte mixing into the reactor's expected liquid products.

The rate of degradation of the gas diffusion electrode's copper catalyst and the rate of flooding of electrolyte into the vapor-fed reactor are both dependent on the flow rate of CO_2 into the reactor. In order to measure these effects, we employed the characterization of the reactor before and after an hour long run of the reactor at different flow rates. Our characterization involved taking cyclic voltametric scans of the reactor, in which a voltage is applied across the working and reference electrodes, and its current density is measured. These scans display the reduction and oxidation reactions occurring at the copper catalyst of the GDE. Over the course of the long-duration trial, a galvanostatic scan was taken, in which a steady current of 350 mA/cm^2 was applied and the voltage

across the reactor was measured. The galvanostatic scan measures the rate of electrochemical reaction. Multiple trials were conducted at varying CO_2 flow rates of 5, 10, 20, and 40 standard cubic centimeters per minute (SCCM). The operating conditions in which we applied to our long-duration trials were influenced by previous literature, which concluded that 5 SCCM of CO_2 at an applied current density of 350 mA/cm^2 outputs the best reactor performance and efficiency [1].

3D-printing the microporous layer (MPL) offers control of the GDE's pore size and density. The MPL is printed on a layer of carbon paper using the Nanoscribe GT2, then a ~ 300 nm layer of copper is deposited on top of the MPL using AJA Sputter system. This design of the gas diffusion electrode allows the copper layer to be used as a catalyst for the CO_2 conversion, and the microporous layer to be used to prevent flooding of electrolyte into the vapor-fed reactor.

Another facet in the effort to optimize the design of the GDE involved measuring the effect that of electrolyte mixing into the liquid products of the CO_2 reduction reactor. To address this, we performed a test involving measuring the rise velocity of the various samples through a capillary tube. The samples included deionized water to act as a control, the electrolyte (KHCO3), the alcohol and acid products, as well as the alcohol and acid products mixed with KHCO3.

Conclusions and Future Steps:

The cyclic voltametric scans taken before and after the long-duration trials suggest that the copper catalyst degrades more rapidly if there is a higher CO_2 flow rate input.

This can be determined because the reduction and oxidation reactions that are present in the characterization of the reactor before the long-duration trial are no longer present afterwards. The galvanostatic scans taken over the course of the trial also show that the CO_2 reduction reactor reaches steady-state operation after approximately half an hour.

Our 3D-printed microporous layer has pores approximately 1-5 microns in diameter, and also improves upon the previous method of 3D-printing the entire GDE. In comparison, printing the MPL takes ~ 6-9 hours, whereas printing the entire GDE takes ~ 35-55 hours.

Results from measuring the rise velocity of electrolyte and liquid products through capillary tubes suggest that KHCO3 has relatively low hydrophobicity, as it has the lowest rise velocity from our tests, and it lowers the rise velocity of the alcohol and acid products when they are mixed together. The results of these experiments will influence the hydrophobic coating used on the microporous layer.

Future work involves coating the printed microporous layer with a hydrophobic coating. The coated microporous layer will then be tested and its effectiveness against electrolyte flooding and catalyst degradation will be measured.

Acknowledgements:

Many thanks to 2024 Cornell NanoScale Facility Research Experiences for Undergraduates Program with Morgan State University (CNF REU MSU) via the National Science Foundation under Grant No. NNCI-2025233. Special thanks to my principal investigator Dr. Sadaf Sobhani for the wonderful opportunity, to my mentor Giancarlo D'Orazio for his patience and guidance, to my staff host Giovanni Sartorello for his support, and to Melanie-Claire Mallison for being an excellent host.

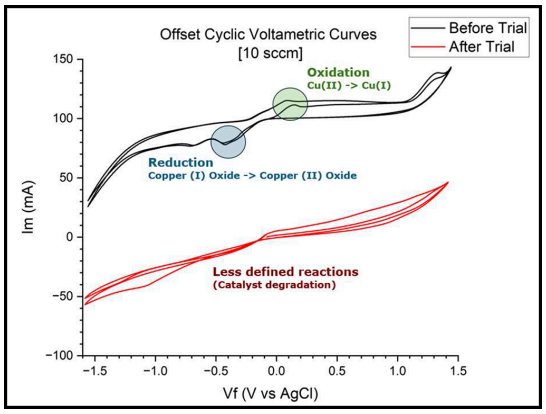

Figure 2: Offset cyclic voltametric scans taken of reactor cell before and after long-duration trial.

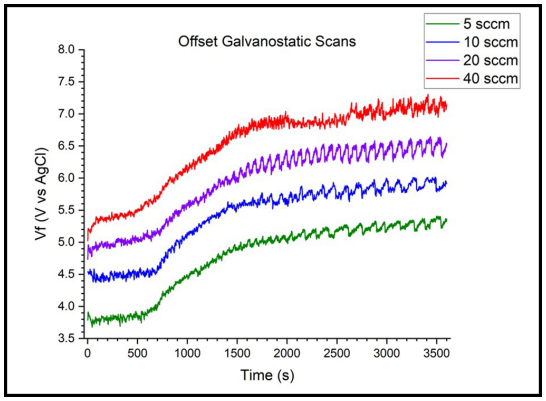

Figure 3: Offset galvanostatic scans of reactor cell at different CO_2 flow rates.

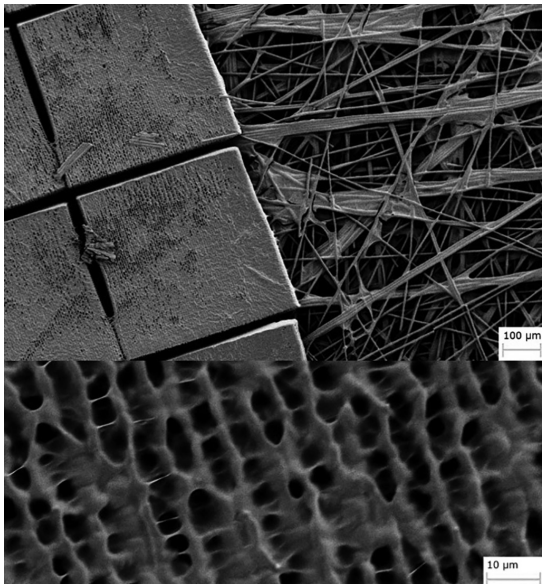

Figure 4: Scanning electron microscope (SEM) images of the microporous layer printed on carbon paper.

References:

[1] D. Corral, et al., "Advanced manufacturing for electrosynthesis of fuels and chemicals from CO_2," Energy Environ. Sci., vol. 14, no. 5, pp. 3064-3074, May 2021, doi: 10.1039/D0EE03679J.

Stoichiometric Dependence of Physical and Electrical Properties of Silicon Nitride

CNF Summer Student: Daniel Teleshevsky
Student Affiliation: Electrical and Computer Engineering, Cornell University

Summer Program(s): 2024 Xing Army Educational Outreach Program (AEOP), 2024 Cornell NanoScale Facility Research Experiences for Undergraduates (CNF REU) Program

Principal Investigator(s): Prof. Huili (Grace) Xing, ECE and MSE, Cornell University

Mentor(s): Phil Infante, Cornell NanoScale Facility, Cornell University

Primary Source(s) of Research Funding: Xing Army Educational Outreach Program (AEOP), National Science Foundation under Grant No. NNCI-2025233

Contact: dt532@cornell.edu, grace.xing@cornell.edu, infante@cnf.cornell.edu

Summer Program Website: https://cnf.cornell.edu/education/reu/2024

Primary CNF Tools Used: LPCVD Furnace, CVC SC4500 Thermal Evaporation System, FleXus, Woollam Spectroscopic Ellipsometer

Abstract:

In recent years, nitride transistors have received much attention in the semiconductor device research community due to their wide bandgap, high thermal conductivity, and polarization properties. Two important performance metrics of these devices are the suppression of leakage current through the gate dielectric and its resilience under repeated use. Previous studies [1] have shown that these properties can be improved in SiN_x (a common gate dielectric for nitride transistors) by changing the stoichiometry of the dielectric deposition.

This investigation entails the physical and electrical characterization of silicon nitride (SiN_x) thin films deposited on silicon substrates by low-pressure chemical vapor deposition (LPCVD). Films were deposited at temperatures of 775°C, 750°C, and 725°C, and dichlorosilane to ammonia gas flow ratios of 5:1, 5:2, and 1:4, yielding a total of nine samples. Physical characterization measurements, including stress and index of refraction, were conducted on each film. The films with the lowest Si content showed the most stress and lowest index of refraction. Aluminum contacts were deposited on the silicon nitride using CNF's CVC SC4500 Thermal Evaporation System and patterned by contact lithography in a metal-first process to form MOS capacitors.

Capacitance-voltage behavior of the fabricated capacitors was measured at a DC probe station to determine the dielectric properties of the SiN_x. The leakage current through the capacitors under applied bias was also measured as a function of time to determine the time-dependent dielectric breakdown of each film.

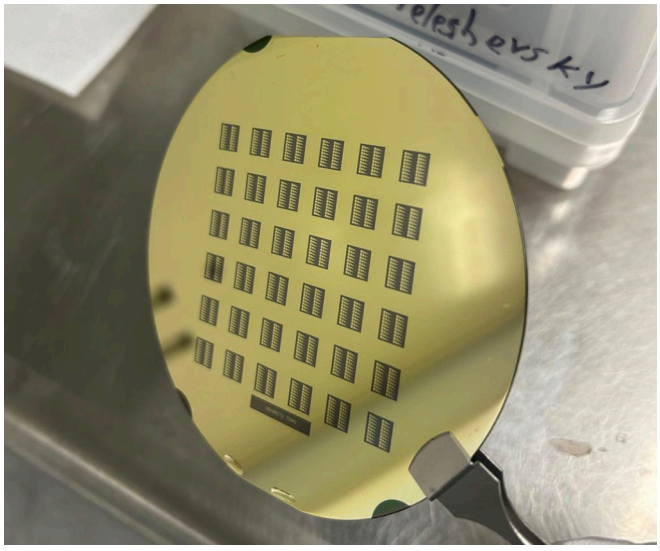

Figure 1: Photograph of the wafer with the individual capacitors visible on the black squares.

Summary of Research:

The goal of this research was to check the impact of low pressure chemical vapor deposition conditions on the characteristics of physical and electrical properties of silicon nitride. This was done using a parallel plate capacitor that consisted of silicon and aluminum as its plates, and silicon nitride as the dielectric. The physical properties tested included the stress imposed by the dielectric and the index of refraction of the dielectric. The electrical properties consisted of the dielectric breakdown of the dielectric, and capacitance measurements of some of the capacitors that included the dielectric.

The process began with a plain 100 mm n-type silicon wafer, on which silicon nitride was deposited using low pressure chemical vapor deposition (LPCVD). This deposition was done at three different ammonia to dichlorosilane ratios and at three different temperatures. The goal of these varying conditions being to vary the concentration of silicon in the dielectric. The

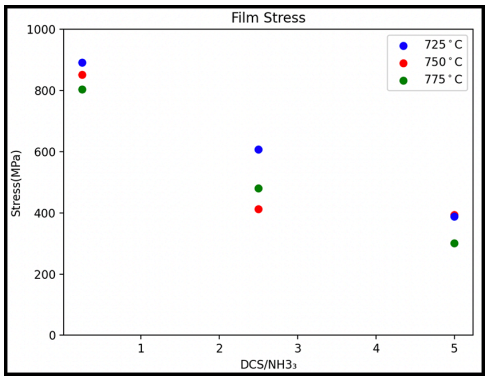

Figure 2: Graph of the stress of the wafer, which is one of the physical properties measured. A potential downward trend of increased stress with decreased silicon concentration is depicted.

three dichlorosilane to ammonia ratios were regulated using the LPCVD furnace, and these three ratios were 5:1, 5:2, and 1:4. The three different temperatures chosen were 775°C, 750°C, and 725°C. This process resulted in nine wafers that had distinct deposition conditions. The physical properties, such as stress and index of refraction, were measured using the FleXus and the Woollam Spectroscopic Ellipsometer respectively. The silicon nitride index of refraction appeared to increase with the concentration of silicon during deposition. The stress imposed by the silicon nitride seemed to decrease with an increased silicon concentration, as well as with higher temperatures during deposition (Figure 2).

The wafer was coated with Al using thermal evaporation, which was patterned and etched using photolithography. This resulted in six clear square capacitors whose width was 50 μm, 100 μm, 200 μm, 300 μm, 400 μm, and 500 μm (Figure 1).

As part of the electrical characterization, the dielectric breakdown of these capacitors, as well as the capacitances of the 500 μm capacitors were measured using the Everbeing EB-6 DC Probe Station. This study included two variables, which were the flow rate of dichlorosilane to ammonia ratios, and the deposition temperature. The dielectric breakdown of silicon nitride was tested in all nine different wafers. It was found that films with a higher concentration of silicon broke down at lower voltages (Figure 3). Different deposition temperatures also showed to impact dielectric breakdown, with higher deposition temperatures causing a dielectric breakdown at lower voltages (Figure 4).

Conclusions and Future Steps:

Both deposition temperatures and silicon content had an effect on the physical and electrical properties of the dielectric. Higher silicon content resulted in lower stress and a higher index of refraction, as well as a faster dielectric breakdown. Additionally, a higher deposition temperature resulted in lower stress and a faster dielectric breakdown. While both conditions did impact the properties of the film, silicon content had a greater effect than deposition temperature.

In the future, time-dependent measurements should be taken of the dielectric breakdown at each of the conditions, and this data should be collected in much larger quantities in order to conduct statistical analysis and determine the statistical significance of the data.

Acknowledgements:

I would like to thank: the Army Educational Outreach Program and the Cornell NanoScale Facility Research Experiences for Undergraduates program; Professor Grace (Huili) Xing, my principal investigator, and Joseph Dill of the Jena-Xing group who provided me with scientific guidance throughout this project; as well as Phil Infante, my mentor, and Ben Infante, without whom this project would have been impossible.

References:

[1] W. M. Waller, et al., in Proc. CS-MANTECH, Indian Wells, CA, USA, May 2017.

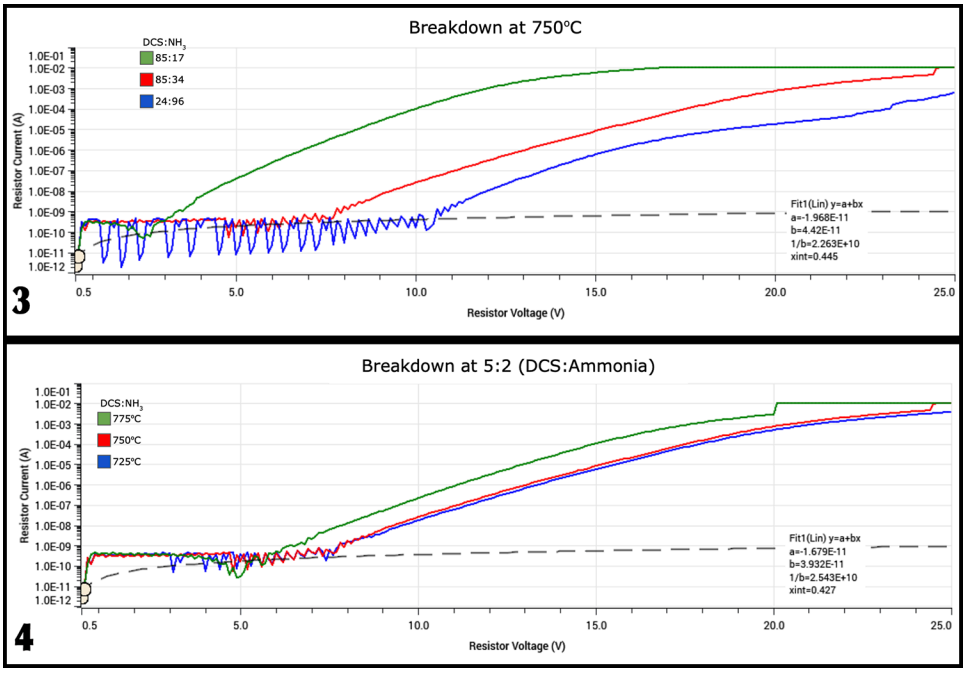

Figure 3, above: Graph of the dielectric breakdown of the silicon nitride at 750°C. A trend of a faster breakdown at higher concentrations of silicon is demonstrated. Figure 4, below: Graph of the dielectric breakdown of the silicon nitride at a 5:2 dichlorosilane to ammonia deposition ratio. A trend of faster breakdown at higher deposition temperatures is demonstrated.

Optimizing Annealing Temperature for Ohmic Contacts to AlGaN/GaN

CNF Summer Student: Timothy Walsh
Student Affiliation: Chemical Engineering, Cornell University

Summer Program(s): 2024 Xing Army Educational Outreach Program (AEOP), 2024 Cornell NanoScale Facility Research Experiences for Undergraduates (CNF REU) Program

Principal Investigator(s): Prof. Huili (Grace) Xing, ECE and MSE, Cornell University

Mentor(s): Aaron Windsor, Cornell NanoScale Science and Technology Facility, Cornell University; Joseph Dill, Applied Engineering Physics, Cornell University; Jimy Encomendero, Electrical and Computer Engineering, Cornell

Primary Source(s) of Research Funding: Xing Army Educational Outreach Program (AEOP), National Science Foundation under Grant No. NNCI-2025233

Contact: tpw29@cornell.edu, hgx2@cornell.edu, windsor@cnf.cornell.edu, jed296@cornell.edu, jje54@cornell.edu

Summer Program Website: https://cnf.cornell.edu/education/reu/2024

Primary CNF Tools Used: GCA AS200 i-line Stepper, Glen 1000 Resist Strip, SC4500 Odd-Hour Evaporator, Rapid Thermal Annealer (RTA), Zeiss Supra SEM, Bruker Energy-dispersive X-ray Spectrometer (EDS), Optical Microscope

Abstract:

As ultra-wide bandgap semiconductor research progresses, the need for reliable, low-resistivity ohmic contacts becomes more essential. To ensure high contact quality and reproducibility, process conditions must be carefully optimized. This project specifically analyzed the impact of various annealing temperatures on a Ta/Al/Ni/Au metal stack to minimize contact resistance. Previously, annealing at 830°C under N_2 ambient showed lateral metal diffusion, known as contact spreading, leading to the transistor short-circuiting and preventing the measurement of contact resistance. GaN pieces were first coated with photoresist, onto which transfer length method patterns were transferred using the GCA AS200 i-line stepper. The SC4500 Odd-Hour evaporator was then used for e-beam evaporation of 20 nm tantalum, 50 nm aluminum, 100 nm nickel, and 40 nm gold. After liftoff, the samples were analyzed and measured under the Zeiss Supra Scanning Electron Microscope (SEM). The samples were then annealed in N_2 ambient at temperatures ranging from 500, 600, 700, 800, and 900°C. Using the SEM and its Energy Dispersive Spectroscopy (EDS), the spreading of the metals was measured. Lastly, using the transfer length method, the optimal annealing conditions for the lowest contact resistance were explored.

Summary of Research:

Silicon Process & Results. The spreading under investigation was seen previously on a 20 nm tantalum, 150 nm aluminum, 50 nm nickel, and 50 nm gold stack on GaN. Thus, the process started by recreating this metal stack onto four 8 × 8 mm Si pieces in order to trial the process. First, each piece was cleaned with sonication in acetone, isopropyl alcohol, and deionized water for five minutes each. Then, to remove any excess moisture, the pieces were placed on a hotplate at 110°C for five minutes. From there, AZ NLOF 2020 negative photoresist was spun onto each piece, with a target width of 1.1 μm, and then they were baked at 115°C for 60 seconds. The GCA AS200 i-line stepper exposed each piece in four spots with an Ohmic contact mask. After baking these pieces again at 115°C for 60 seconds on a hotplate, they developed in 726 MIF for 60 seconds, removing the unexposed

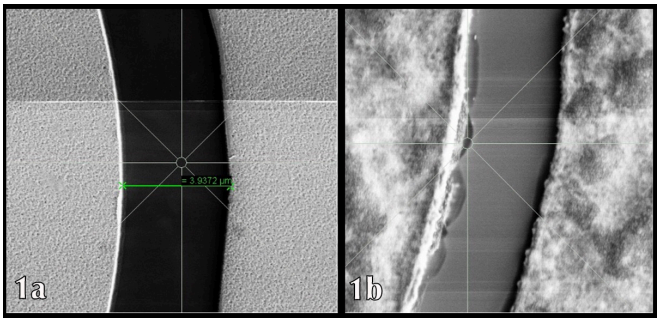

Figure 1: (a) Si Sample 2 µm Gap Pre-anneal. (b) Si Sample 2 µm Gap Annealed at 850°C.

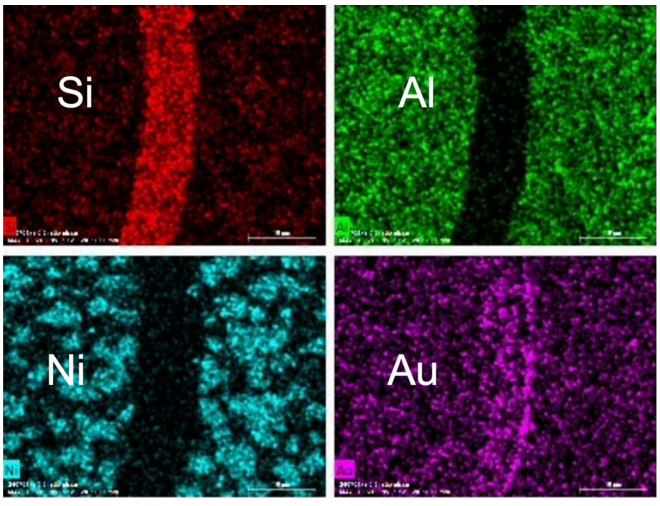

Figure 2: Si Sample 2 µm Gap Annealed at 700°C.

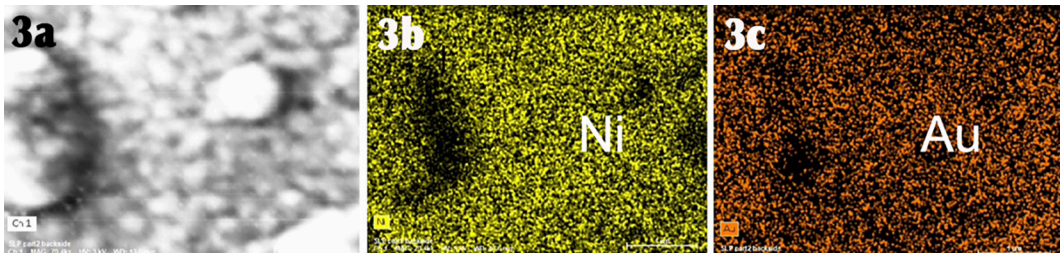

Figure 3: (a) GaN SEM Image. (b): Ni EDS. (c) Au EDS.

photoresist. The Glen 1000 Resist Strip removed any excess organic matter or resist on the pieces. To deposit the metal stack, the SC4500 Odd-Hour electron beam evaporator was used. Liftoff consisted of 10 minutes in Microposit Remover 1165, five minutes isopropyl alcohol, both in sonication, then a rinse with deionized water. Under the Zeiss Supra SEM, the Circular Transfer Length Method (C-TLM) spacings were measured, and EDS baseline images were taken. Then, the four pieces were annealed at 700, 750, 800, and 850°C for 60 seconds under N_2 ambient in the Rapid Thermal Annealer (RTA). Again, the pieces were analyzed under the SEM with EDS to examine any spreading.

Before annealing, the circle lines were crisp, as seen in Figure 1(a). After annealing, visual spreading of aluminum could be seen under both the optical microscope and the SEM, as in Figure 1(b). Additionally, annealing induced nickel clumping. This can be seen in the EDS images in Figure 2. This effect is likely due to the high surface energy of nickel. Since aluminum melts at 660°C, it likely forms a liquid at an annealing temperature above this. Because the nickel sits atop this aluminum liquid, to reduce its surface energy, the nickel obtains a lower surface energy by forming spheres. This causes the clumping effect.

GaN Process and Results. The fabrication process with five 10 × 10 mm GaN pieces was identical to that of the Si pieces, except before the electron beam deposition, the pieces were cleaned in HCl, deionized water, BOE, and deionized water again for 60 seconds each. Additionally, the Ta/Al/Ni/Au metal stack was changed to 20 nm tantalum, 50 nm aluminum, 100 nm nickel, and 40 nm gold. The intention was to reduce the amount of aluminum liquid that the nickel layer sits atop to prevent the nickel clumping. Also, the thickness of nickel was doubled to encourage it to remain flat instead of clumping and forming spheres. The five GaN pieces were annealed at 500, 600, 700, 800, and 900°C, and the 800°C sample was measured on a probe station.

On GaN, there was no visual spreading as there was on the Si, but a "bubbling" effect was observed. This bubbling is evident in Figure 3(a). Figure 3(b) and 3(c) show that these bubbles are actually voids of gold and nickel, so they are different from the nickel clumps seen on Si. Annealing the

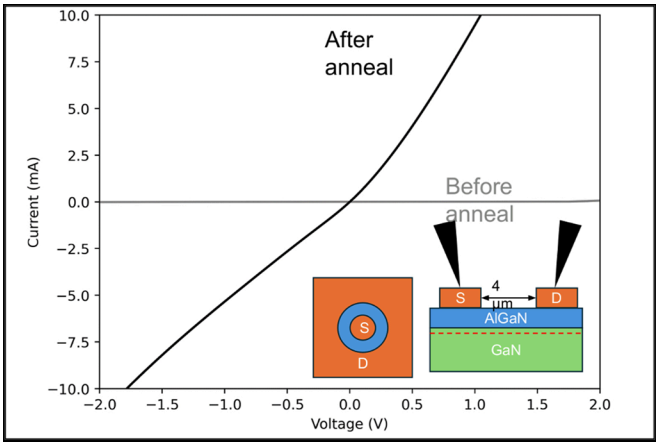

Figure 4: TLM Measurement for 800°C GaN Sample.

GaN at 800°C increased the amount of current that could pass through the contact by roughly two orders of magnitude, as shown in Figure 4. Although, the contact is still not Ohmic, as Current vs Voltage is not linear.

Conclusion and Future Steps:

Varying the annealing temperature of the Ta/Al/Ni/Au stack on GaN from 500 to 900°C showed minimal spreading but an increasing "surface bubbling" effect as temperature increases. Nickel clumping as well as spreading on the Si pieces was evident after annealing, and future TLM measurements on the GaN pieces will determine the annealing temperature with the lowest contact resistance.

Acknowledgements:

The author would like to thank the Army Educational Outreach Program (AEOP) and the Cornell NanoScale REU Program; my principal investigator, Professor Grace Xing, and my mentors, Aaron Windsor and Jimy Encomendero.

Self-Assembly of CdS Quantum Dot Films with Chiral Optical Properties

CNF Summer Student: Jaden Watt
Student Affiliation: Mechanical Engineering, North Carolina Agricultural and Technical State University

Summer Program(s): 2024 Cornell Center for Materials Research North Carolina Agricultural & Technical State University (CCMR NC A&T) Summer Program, 2024 CNF REU Program

Principal Investigator(s): Richard Robinson, Materials Science & Engineering, Cornell University

Mentor(s): Thomas Ugras, Materials Science & Engineering, Cornell University

Primary Source(s) of Research Funding: 2024 CCMR NC A&T, NSF Grant No. NNCI-2025233, Empire State Development, Air Force Research Lab Regional Network, Fuze Hub, Cornell Atkinson Center for Sustainability

Contact: jawatt1@aggies.ncat.edu, rdr82@cornell.edu, tju6@cornell.edu

Summer Program Website: https://cnf.cornell.edu/education/reu/2024

Abstract:

This project investigates the self-assembly of CdS magic-size clusters (MSCs), a type of quantum dot, into hierarchical films with complex structures that mimic biomolecular organization. We focus on developing chiral optical films through thiolation and examining their optical properties [1]. Our experiments involve time-resolved thiolation, aiming to shift the absorption peak from 324 nm to 350 nm over 48 hours. We also study spatial variations in thiolate films, expecting similar spectral shifts. Glass substrates are prepared and coated with CdS solutions, then thiolate and analyzed using circular dichroism spectrometry. Although the predicted peak shift to 350 nm was not fully achieved, the films exhibit novel chiral and linear dichroic properties, alongside intriguing LDLB interactions. These findings indicate potential applications in creating nano-polarized light pixels. The primary tool used in the lab was the JASCO-1500 CD Spectrometer, which was essential in characterizing and analyzing the films.

Summary of Research:

This research aimed to explore the self-assembly of CdS quantum dot films that exhibit chiral optical properties, with a particular focus on how thiolation affects these films' optical characteristics [1]. Thiolation refers to the process of treating quantum dot films with thiol ligands. This treatment alters the optical properties of the films, including a redshift in the absorption spectrum due to changes in the electronic environment of the quantum dots [2]. This study was motivated by the potential applications of quantum dots in advanced technologies, such as nano-polarized light pixels, which require precise control over chiral optical properties. Additionally, the research aimed to investigate the influence of linear dichroism (ld) and linear birefringence (lb) effects on the optical behavior of the films.

Circular Dichroism (CD) is the differential absorption of right- and left-circularly polarized light used to characterize chiral materials. In this study, CD was employed to analyze the chiral optical properties of the films. LD refers to the differential absorption of light polarized in different linear orientations; an effect important in materials with anisotropic optical properties. LB, on the other hand, is the splitting of a light beam into two rays that travel at different speeds due to the material's optical anisotropy. The combination of LD and LB can result in a CD signal because the orientation and birefringence of the material influence how circularly polarized light is absorbed, leading to chiroptical effects.

This research was conducted through a series of experiments designed to observe the effects of thiolation on CdS films, both over time and across different spatial locations, while also examining the impact of LD and LB effects. The primary objective of the time-resolved experiment was to shift the absorption peak of the CdS films from 324 nm to 350 nm over 48 hours and to study the progression of the absorbance and CD of the film to see if there are different stages or intermediate species. To achieve this, CdS films were prepared and then subjected to thiolation over various time intervals. The optical properties of the films, including LD and LB effects, were measured using CD and absorbance spectroscopy.

The spatial experiment aimed to observe the variations in the optical properties of the thiolate films depending on the location of measurement because we have observed that the chiroptical response can be of opposite-handedness and varying magnitudes across a single MSC film. Measurements were taken at three different spots on the thin film before (Figure 3) and after thiolation (Figure 3) to determine how spatial differences influenced the absorption peaks and the LD/LB effects. In the time-resolved experiments, a progressive shift in the absorption peak was observed during the thiolation process, although the expected shift to 350 nm was not fully achieved within the 48-hour timeframe. The films exhibited distinct chiral properties, with notable variations in left-hand and right-hand circularly polarized light, as indicated

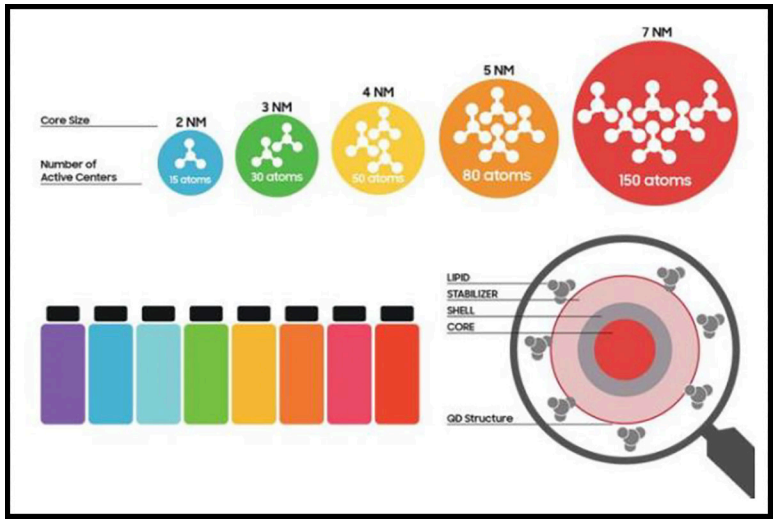

Figure 1: Quantum dots & Products/Technology -QD-OLED. Samsung Display. (n.d.). https://www.samsungdisplay.com/eng/tech/quantum-dot.jsp

Figure 2: Films made of glass substrates and tape.

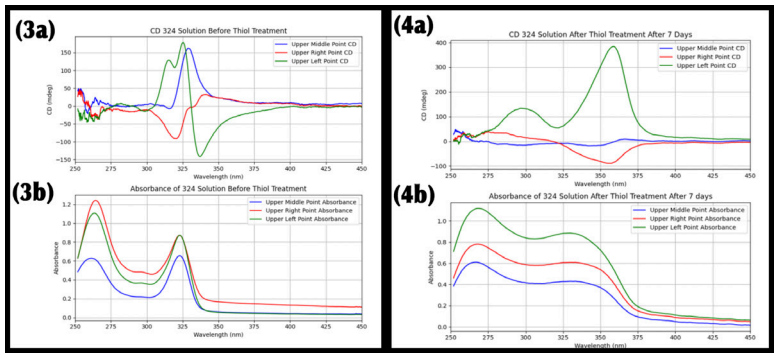

Figure 3, left: a, CD for 3 different positions on an MSC film before treatment. b, Absorbance for 3 different positions on an MSC film before treatment. Figure 4, right: a, CD for 3 different positions on an MSC film after treatment. b, Absorbance for 3 different positions on an MSC film after treatment.

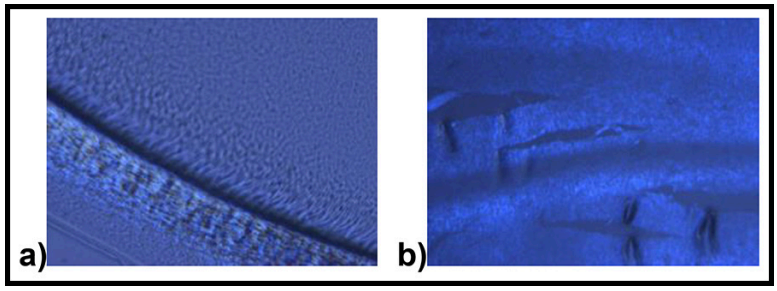

Figure 5: a, MSC film under a microscope before treatment. b, MSC film under a microscope after treatment.

by the CD spectra. Furthermore, the LD and LB effects were prominent, demonstrating how the orientation of the films influenced the absorption of polarized light and the splitting of light beams traveling through the material.

The spatial experiments revealed that the absorption peaks varied depending on the specific location measured on the film (Figure 4), confirming that the effects of thiolation were not uniform across the entire mo. The spatial differences also highlighted variations in LD and LB effects across the film. The thiolation process induced significant changes in the chiral properties of the CdS films, though the desired peak shift to 350 nm was not fully realized. The observed LD and LB effects further contributed to understanding how film orientation and thiolation influence the optical properties of quantum dot films. These results suggest that thiolation has the potential to fine-tune the optical properties of quantum dot films and the structure of the film (Figure 5), particularly in enhancing their chiral and polarized light responses. Future research could explore longer thiolation times, alternative thiol ligands, and manipulating LD/LB effects to achieve more pronounced shifts in optical properties.

This study successfully demonstrated the potential of thiolation to modify the optical properties of CdS quantum dot films, particularly in enhancing their chiral characteristics and LD/LB effects. While the specific goal of shifting the absorption peak to 350 nm was not met, the findings provide valuable insights into quantum dots' self-assembly, optical behavior, and polarization effects.

References:

[1] Chem. Commun., 2017, 53, 2866-2869.

[2] Nano Lett. 2022, 22, 1778-1785.

Atomic Layer Etching of III-Nitride Semiconductors

CNF Summer Student: Hajo Johann Wise
Student Affiliation: Mechanical Engineering, Rochester Institute of Technology

Summer Program(s): 2024 Xing Army Educational Outreach Program (AEOP), 2024 Cornell NanoScale Science & Technology Facility Research Experiences for Undergraduates (CNF REU) Program

Principal Investigator(s): Prof. Huili (Grace) Xing, ECE and MSE, Cornell University

Mentor(s): Dr. Xinwei Wu, Cornell NanoScale Science and Technology Facility, Cornell University

Primary Source(s) of Research Funding: 2024 Xing Army Educational Outreach Program (AEOP), National Science Foundation under Grant No. NNCI-2025233

Contact: penguinhajo1@gmail.com, grace.xing@cornell.edu, xw77@cornell.edu

Summer Program Website: https://cnf.cornell.edu/education/reu/2024

Research Group Website: https://jena-xing.engineering.cornell.edu/

Primary CNF Tools Used: Veeco Icon AFM, ABM Contact Aligner, Zeiss SEMS, Plasma-Therm Takachi ALE, Oxford 81 RIE etcher, Oxford 100 PECVD, P-7 Profilometer, Woolam RC-2 Ellipsometer

Abstract:

III-nitride semiconductors offer unique advantages in the manufacturing of high-voltage field effect transistors (FETS). However, production of nanoscale III-nitride FETs requires precise etching of III-nitride semiconductor films. We identified atomic layer etching (ALE) as an ideal technique for this application. ALE weakens the bond between a film and its surface layer via a chemical reaction with a reagent gas or plasma. The reagent is then purged, and the surface is bombarded with non-reactive ions. These ions impart enough energy to sputter away the reacted surface layer, but not enough to remove unreacted material underneath. These self-limiting characteristics allow for consistent removal of a few atomic layers at a time [1].

To adapt and characterize ALE for the processing of III-nitride films, samples with gallium nitride (GaN), aluminum nitride (AlN), and aluminum-gallium nitride (AlGaN) films were etched in the Cornell NanoScale Facility's (CNF) Plasma-Therm Takachi ALE tool. All ALE recipes tested used a Cl_2 and BCl_3 chemistry. However, key parameters such as gas flow rate, bias power, inductively coupled plasma (ICP) power, and step times were varied. Critical etch metrics such as surface roughness, film thickness, etch rate, and etch selectivity were recorded for each trial. By identifying recipe elements that yielded favorable etch results, this report gives preliminary guidance for the ALE of III-Nitride semiconductors.

Summary of Research:

The first round of ALE processing was performed with one of each sample type (GaN, AlN, AlGaN) and a photoresist mask process. Nlof-2020 negative photoresist was chosen due to its popularity in device fabrication. Test features were patterned onto the samples to provide convenient etch characterization sites. The recipe flowed 30 sccm each of Cl_2 and BCl_3 for surface modification and applied 10 W of bias power for ion bombardment. All three samples were processed at the same time, for 20 ALE cycles.

Following ALE, profilometry was performed on the AlGaN sample, producing the reading shown in Figure 1. Notably, this reading indicated that the "etched" areas were ~ 250 nm higher than the unetched areas. This meant that something must have deposited during the etching process. This substance can be seen in SEM imagery of the sample (Figure 2), where the raised squares should be etched into the surface. Both the GaN and AlN samples exhibited deposition as well.

To identify the substance, energy-dispersive x-ray spectroscopy (EDS) was employed to map elements on the sample's surface. Figure 3 shows an SEM image of the AlGaN sample with a corresponding boron EDS map. Boron correlates with deposits along the edge of the etch pad, suggesting that it played a role in deposition. However, EDS is not sensitive enough to lighter elements to positively identify the material.

While inconclusive, the EDS results hinted that photoresist might play a role in the deposition. Consequently, our process flow was adapted to use an SiO_2 hard mask for the next trial. Only AlN was tested, due to limited sample availability. The ALE recipe was altered to flow 30 sccm of Cl_2 and 3 sccm of BCl_3, while the bias power was reduced to 8 W. These changes limited boron concentration, reducing the likelihood of adverse reactions. The sample was processed for 100 total ALE cycles, with measurements taken after 50 cycles.

Initial results from the hard-mask sample were promising, with ellipsometry indicating an etch depth of 20 nm after 50 cycles. The etched surface was also significantly smoothed, with a pre-etch roughness of 2.66 nm RMS and a post-etch roughness of 1.70 nm RMS. Unfortunately, the sample also exhibited crystalline defects across all exposed AlN surfaces.

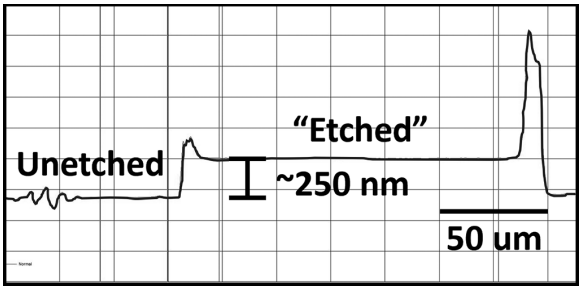

Figure 1: Profilometry reading of "etched" feature.

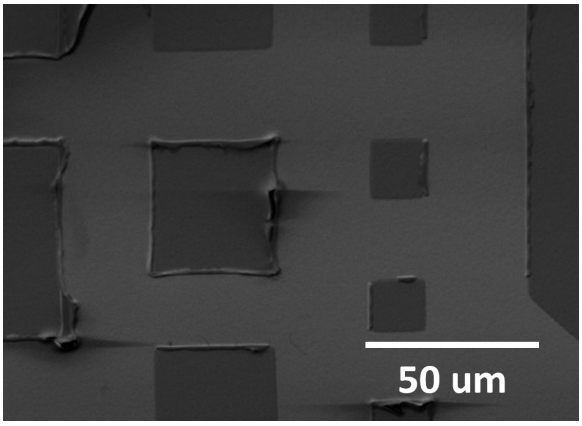

Figure 2: SEM image of "etched" squares.

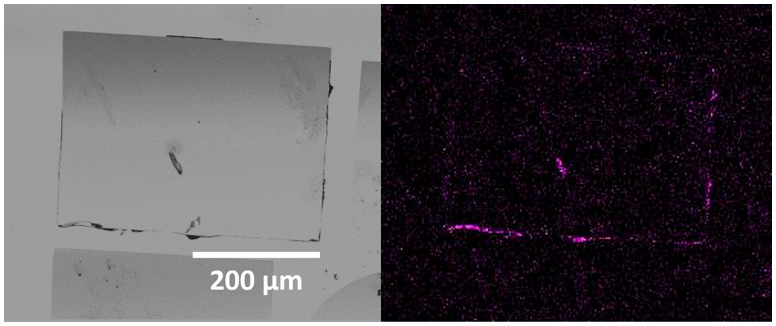

Figure 3: SEM and boron EDS imagery of photoresist-masked sample.

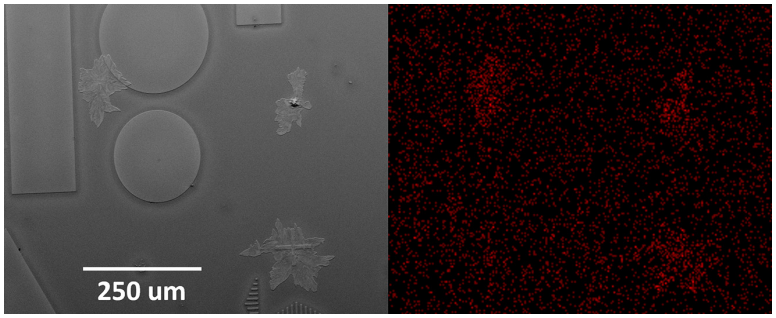

Figure 4: SEM and chlorine EDS image of hard-mask sample, including crystalline defects.

These defects are visible in the SEM image of Figure 4, where they appear to have grown across the patterned surface.

EDS was once again used to analyze the defects, with the EDS image Figure 4 showing a chlorine map of the sample. Chlorine hotspots strongly correlate with the defects, indicating that they contain chlorine. However, no other elements demonstrated a similar correlation. This poses an issue, as pure chlorine is a gas at room temperature. Logically, there must be other elements in the defects that we were unable to positively identify.

Conclusions and Future Steps:

While ALE processing was not wholly successful, these trials highlight "best practices" that will hopefully contribute to a mature process flow in the future. The use of a hard mask is the most apparent, as it likely contributed to the significantly cleaner result of the second trial. Hard masks, especially SiO_2, are known for their resistance to unwanted chemical interaction. This is especially valuable for a high precision process like ALE, where even minimal unexpected reactions can disrupt the etching cycle.

Looking to the future, there are several promising approaches to obtain more favorable results. First, it would be useful to analyze the deposits with wavelength-dispersive x-ray spectroscopy (WDS). This technique is similar to EDS, but it offers increased sensitivity to lighter elements. This may allow for positive identification of the deposited materials, and subsequent process alterations to prevent their formation. Aside from WDS, an ALE recipe without BCl_3 would entirely remove a potential source of unwanted chemical reactions. We believe that these techniques and alterations will bring us one step closer to the successful atomic layer etching of III-nitrides.

Acknowledgements:

This work was carried out at the Cornell NanoScale Science and Technology Facility, an NNCI member site supported by NSF grant no. NNCI-2025233. The opportunity to work at CNF was provided by the Army Educational Outreach Program. I'd like to give special thanks to Professor Grace Xing, Dr. Xinwei Wu, Wenwen Zhao, Jeremy Clark, Joseph Dill, Lynn Rathbun, and Melanie-Claire Mallison.

References:

[1] Keren J. Kanarik, Samantha Tan, and Richard A. Gottscho. Atomic Layer Etching: Rethinking the Art of Etch; The Journal of Physical Chemistry Letters 2018 9 (16), 4814-4821. DOI: 10.1021/acs.jpclett.8b00997 Copyright 2018 by American Chemical Society.

In Situ FTIR Spectroscopy to Probe Effects of $LiNO_3$ on First Cycle SEI Formation and Electrolyte Decomposition in Li-Metal Batteries

CNF Summer Student: Ben Hodder Alexander
Student Affiliation: Physics, Haverford College (graduated spring 2024); Physics Ph.D. Program, Stanford University (starting fall 2024)

Summer Program(s): 2024 Cornell NanoScale Facility International Research Experiences for Undergraduates (CNF iREU) at National Institute for Materials Science (NIMS), Tsukuba, Ibaraki, Japan

Principal Investigator(s): Dr. Hidenori Noguchi, Chief Researcher, Interface Electrochemistry Group, Battery and Cell Materials Field, Research Center for Energy and Environmental Materials (GREEN) at NIMS; Graduate School of Chemical Sciences and Engineering, Hokkaido University

Mentor(s): Wang Yushen, Research Center for Energy and Environmental Materials (GREEN) at NIMS; Graduate School of Chemical Sciences and Engineering, Hokkaido University

Primary Source(s) of Research Funding: NSF awards under Grants No. OISE- 2246252 (IRES) and NNCI-2025233

Contact: benalex@stanford.edu, noguchi.hidenori@nims.go.jp, wang.yushen@nims.go.jp

Summer Program Website: https://cnf.cornell.edu/education/reu/2024

Abstract:

Anode-free lithium metal batteries have a high theoretical performance ceiling for next-generation energy storage. To better control the system, it is important to understand the behavior of the solid electrolyte interface layer, particularly during the first charge cycle. This work uses FTIR spectroscopy to examine the role of lithium nitrate additive in ether electrolytes. Lithium nitrate is found to promote the irreversible formation of organic SEI species during electrolyte decomposition in TEGDME.

Summary of Research:

Background and Motivation. The commercial lithium-ion battery is a backbone of modern rechargeable energy storage, being found everywhere from electric vehicles to cellular phones. While improvements in storage capacity are ongoing, they are theoretically limited by the graphite anode used in the system — a limitation made more painful by ever-increasing demands for energy storage in pursuit of climate-friendly infrastructure.

Lithium metal anodes represent a theoretical order of magnitude improvement in specific capacity over their graphite counterparts in commercial batteries [1]. Significant challenges remain, however, in developing lithium metal battery (LMB) technology for commercial use. This includes poor cycle life and safety issues, often resulting from lithium dendrite growth and/or parasitic reactions [2]. Anode-free configurations (anode-free lithium metal battery: AFLMB), where lithium is electrodeposited directly upon a current collector, seek to improve cell capacity and enable easier manufacturing. In such conditions, lithium is plated on the electrode surface during the first charge cycle, motivating the attention of researchers.

The interface between the electrode and electrolyte is chemically unstable, resulting the in formation of a solid electrolyte interface (SEI) layer between the two. This study aims to understand the first cycle behavior of this layer in ether electrolyte systems, with a particular emphasis on the role of lithium nitrate ($LiNO_3$) in the system, which is understood to improve stability as an additive [3].

Materials and Methods. Electrolyte solutions were prepared in glovebox using tetraethylene glycol dimethyl ether (TEGDME), which is commonly used in oxygen battery systems for its superior cathodic stability [4]; the common ether solvent dimethoxymethane (DME) was used for comparison measurements. Lithium bis(trifluoromethanesulfonyl)imide (LiTFSI) was added to these ethers as the primary salt at 0.4 M concentration. samples were tested without $LiNO_3$, and to maintain a constant concentration of Li^+, with an 0.05 M (functioning as an additive) or 0.2 M (as a co-salt) concentration of $LiNO_3$ replacing LiTFSI salt. All electrolytes were tested in a half cell with a copper working electrode and metallic Lithium reference and counter electrodes to examine anode behavior.

Characterization was primarily performed via Fourier Transform Infrared (FTIR) spectroscopy. Sectra were captured continuously, with a collection time of approximately 30 seconds while performing cyclic voltammetry tests of the first cycle behavior at 1 mV/s. Python code was written to analyze the large number of spectra produced by such a methodology.

Similar cyclic voltammetry tests were performed alongside quartz crystal microbalance (QCM) measurements of surface absorbed mass — after calibration, this allowed calculation of MPE (mass absorbed per mole of electrons of passed charge) values associated with the identified process.

Results. While data was collected to examine the entire first cycle anode behavior, the results presented here focus on the electrolyte decomposition process in TEGDME. They suggest that $LiNO_3$ accelerates the formation of organic surface species in the pre-SEI layer that are formed because of slightly decomposed TEGDME solvent.

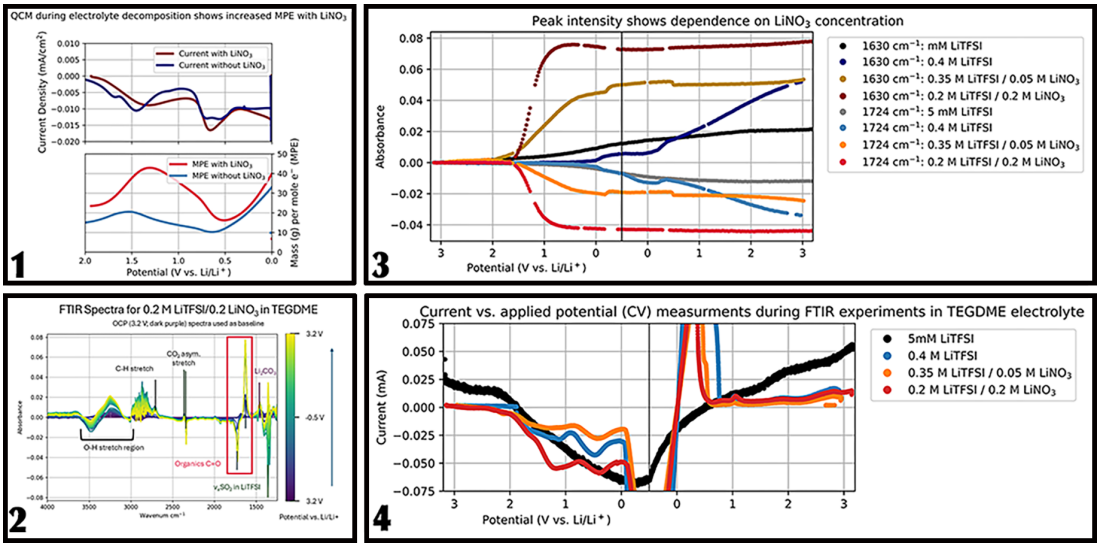

The electrolyte decomposition process in solvents containing (0.4 M LiTFSI in TEGDME) and not containing (0.2 M LiTFSI/ 0.2 M $LiNO_3$ in TEGDME) was first examined using a quartz crystal microbalance. Results are shown in Figure 1. Mass per electron values (technically an average over the entire system) increased from approximately 20 g/mole e^- to over 40 during electrolyte decomposition — note that this process identified with the first downwards peak in current, around 1.3 V vs. Li/Li^+. MPE values are notably high for electrochemical processes and likely correspond to either the deposition of organics or a chemical process, rather than a strictly electrochemical one; a chemical reaction not requiring electrons to deposit material has a theoretically infinite mass per electron value.

This process was examined in greater detail using FTIR spectroscopy. Figure 2 shows the spectra collected during the cycle of the half cell in TEGDME with $LiNO_3$. Various peaks were observed. This included hydrogen bonding; $\nu_a SO_2$ bonds breaking in LiTFSI; signs of lithium carbonate, a common SEI species; CO_2; and C=O bonding from organic species.

This work focuses on the last of these observations: the most unexpected result and one displaying a strong dependence on lithium nitrate. This can be most clearly seen in the heights of the absorbance peaks as a function of applied potential, shown in Figure 4. This shows peaks at 1724 cm^{-1} and 1630 cm^{-1}. Both are identified with C=O bonding, with the former believed to correspond to chemically decomposed TEGDME solvent and the latter thought to be a lithium-containing organic SEI species (e.g. ROCO2Li or Li-formate). Note that decreases in absorbance for the peak at 1724 cm^{-1} correspond to increases in absorbance at 1630 cm^{-1}, indicating that the former is consumed to produce the latter in all samples.

However, $LiNO_3$ has clear effects on this process. Let us scrutinize the electrolyte decomposition region, identified to be at 1.3 V on the downwards potential scan by examination of Figure 3. Here, increasing concentrations of $LiNO_3$ correspond to the acceleration of this process. Notably, this results in greater stability after the lithium plating and stripping process in systems with $LiNO_3$.

Conclusions and Future Steps:

The ability of $LiNO_3$ to accelerate organic deposition in the SEI layer in TEGDME may help explain its role as a stabilizing agent — as $LiNO_3$ is known to quicken electrolyte decomposition, it may allow the system to reach near-equilibrium before plating and stripping. Alternatively, these results might indicate potential issues with the stability of TEGDME on the anode side. The organic deposition observed here may be undesirable and has not been the focus of previous studies with the solvent, which generally emphasize cathode interactions in Li-O_2 systems.

In future studies, the effects of this organic deposition on later cycles could be combined with additional characterization techniques to obtain a more complete understanding of the system. Such an understanding aids in developing the stable SEI layers required for the success of Li-metal batteries. This work may also motivate study into native-SEI formation and chemical degradation of ether solvents. Such understanding could improve the precision of work throughout the field.

Acknowledgments:

Participation supported by National Science Foundation awards to Cornell University under OISE-2246252 (IRES) and NNCI-2025233 (NNCI). Thanks are given to Yushen Wang for excellent mentorship and Dr. Hidenori Noguchi for hosting this research.

References:

[1] Shao, A., et al. Advanced Energy and Sustainability Research 2022, 3 (4), 2100197. https://doi.org/10.1002/aesr.202100197.

[2] Jo, C.-H., et al. Energy Storage Materials 2023, 57, 471-496. https://doi.org/10.1016/j.ensm.2023.02.040.

[3] Wu, L., et al. Electrochimica Acta 2023, 466, 142973. https://doi.org/10.1016/j.electacta.2023.142973.

[4] Chen, J., et al. ACS Omega 2019, 4 (24), 20708-20714. https://doi.org/10.1021/acsomega.9b02941.

Fabrication and Photoelectron Spectroscopy of Sn-Based Intermetallic Compounds

CNF Summer Student: Vashti Allred
Student Affiliation: Chemical and Environmental Engineering, University of Arizona

Summer Program(s): 2024 Cornell NanoScale Facility International Research Experiences for Undergraduates (CNF iREU) at National Institute for Materials Science (NIMS), Tsukuba, Ibaraki, Japan

Principal Investigator(s): Takeo Ohsawa and Naoki Ohashi, National Institute for Materials Science (NIMS), Japan

Primary Source(s) of Research Funding: NSF awards under Grants No. OISE- 2246252 (IRES) and NNCI-2025233

Contact: vapallred@gmail.com, ohashi.naoki@nims.go.jp, ohsawa.takeo@nims.go.jp

Summer Program Website: https://cnf.cornell.edu/education/reu/2024

Abstract:

This paper explores the physical properties of tin-based intermetallic compounds AuSn, $AuSn_2$, and $AuSn_4$ for their potential application in sustainable energy. Using x-ray diffraction (XRD), x-ray photoelectron spectroscopy (XPS) and ultraviolet photoelectron spectroscopy (UPS), the study reveals how increasing the tin content alters their crystal structure and electronic properties leading to unexpected shifts in binding energy and work function values. These findings suggest the need for further research to explore the complexity of the system and optimize the material for future sustainable energy applications.

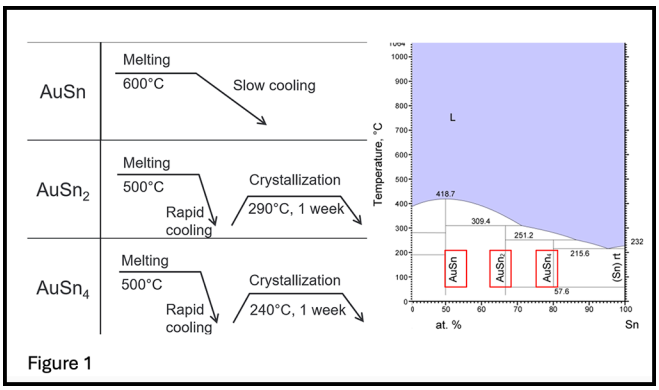

Figure 1

Introduction:

In a world that is continuing towards a decarbonized future, the pursuit of materials for sustainable eco-friendly energy solutions with tailored physical and chemical properties is crucial. Among these materials, tin-based intermetallic compounds, particularly AuSn, $AuSn_2$, and $AuSn_4$, have attracted attention recently in our group for their potential applications in various energy-related technologies. These intermetallic compounds have unique crystal structure and physical properties that alter with the amount of tin in the sample. Understanding how the material works and what is driving the physical changes is key in optimizing the performance of the future technology for practical applications.

One of the potential approaches for the materials exploration has been reported in the discovery of electrides. This is a class of materials with a unique crystal structure where the electrons serve as anions. These materials have been shown to exhibit unusual physical properties both electronically and optically. The study of these materials provides valuable insights into the relationship between the crystal structure and fundamental physical properties, possibly providing a solution for the interesting properties seen in the tin-based compounds.

This paper explores the unique physical properties seen with highly pure AuSn, $AuSn_2$ and $AuSn_4$. By examining the impact of the tin content in the compound through the XPS data and work functions, this study aims to shed light on the potential of these materials and the advancing development of eco-friendly energy technologies.

Materials and Methods. In creating the samples for analysis in the study, each compound was synthesized slightly differently. For the AuSn sample, the melting point was higher and thus was heated to 600°C and slowly cooled which created a pure alloy of tin and gold. For the $AuSn_2$ and $AuSn_4$ the samples needed to be heated to 500°C and then rapidly cooled and crystalized at 290°C and 240°C, respectively. This process created samples that had the correct crystalline structure (Figure 1).

After the samples had been created, XRD was done to confirm their crystalline structures. The machine used a 5 mm slit and swept two theta angles from 10° to 80°. This was placed against a reference to see where the peaks were located on the spectrum. XPS and UPS were then completed for the samples to see what electronic states they were exhibiting. The use of argon gas was employed to complete a contamination removal and a depth analysis. The UPS measurement enables

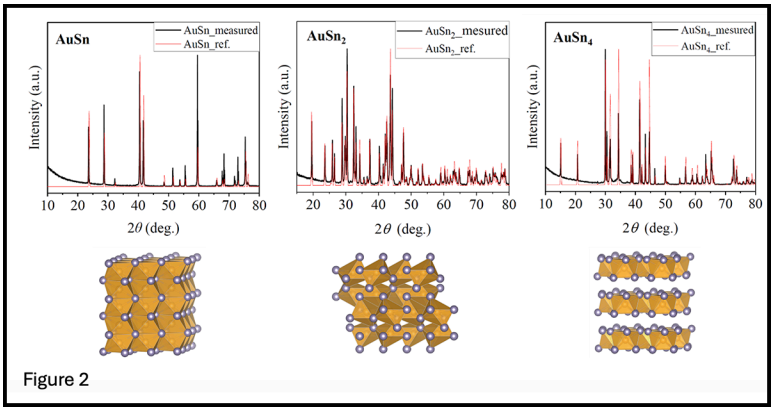

Figure 2

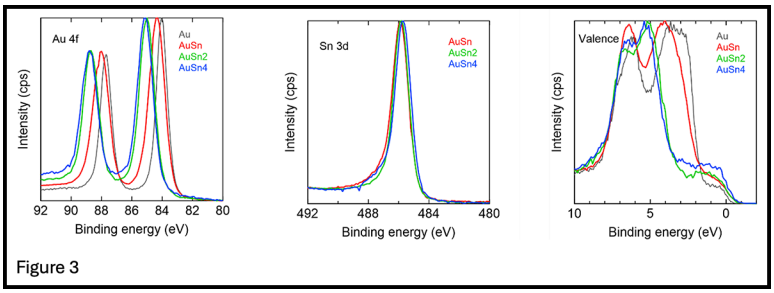

Figure 3

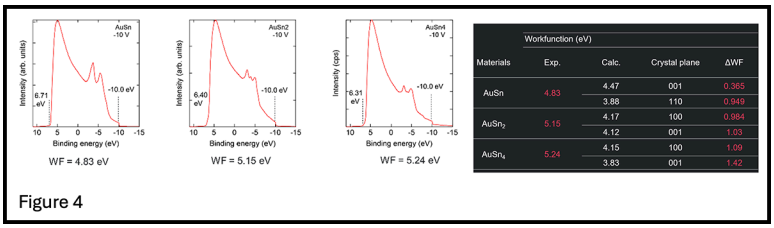

Materials	Workfunction (eV) Exp.	Calc.	Crystal plane	ΔWF
AuSn	4.83	4.47	001	0.365
		3.88	110	0.949
$AuSn_2$	5.15	4.17	100	0.984
		4.12	001	1.03
$AuSn_4$	5.24	4.15	100	1.09
		3.83	001	1.42

Figure 4

to estimate the workfunction values, which is important to create practical electronic devices.

Results and Discussion. From XRD analysis, the reference and experimental data lined up showing that our intermetallic samples are highly pure and crystalline Au-Sn compounds, as designed (Figure 2). After confirming the orientation of the crystal planes, the AuSn sample was examined by XPS which interestingly had a shift towards higher binding energy in the gold spectra compared to the gold reference. This implies that there is an increase of positive charge cations or a decrease in negative charge anions with the addition of tin. Similarly, this also occurred in the valence spectrum where the band was narrower, and the binding energy was shifted higher implying that there is ionic bonding occurring. From both of these observations, it is hypothesized that the gold and tin in AuSn are behaving as cations in the sample.

To further examine the samples and confirm the hypothesis, the $AuSn_2$ and $AuSu_4$ samples were run through XPS and it was found that as the tin content increased in the sample, the binding energy was shifted higher in the gold spectrum. In the tin spectrum the samples seemed to stay consistent in the peak position. However, in the valence spectra again it was seen that with an increase of tin the band decreased in width and shifted to higher binding energy (Figure 3).

Additionally, to gain more data on the system, the work function was examined theoretically and experimentally through UPS. It was found that the experimental work functions differed from the theoretical, and the change became more apparent as tin content increased in the sample (Figure 4). This leads to some interesting questions as to why the work function values differ so greatly from the theoretical with the change in tin. Looking more closely at the crystal orientation of each sample it is believed that something is not being explored fully. This leads back to the XPS results and the spectra increasing in binding energy with the increasing tin and the associated hypothesis of the gold and tin acting as cations.

Looking at the materials that have similar physical properties, electrides are front and center. Although with the tin-based intermetallic compounds, the atoms are acting as cations instead of anions. There is still testing and further research to be done to solidify how the material works but it is interesting to note that the tin-based samples are not behaving the same way experimentally as they are theoretically.

Conclusions:

In conclusion, this study reveals how the crystal structure and tin content in AuSn, $AuSn_2$ and $AuSn_4$ intermetallic compounds influence their physical properties. Through XRD, XPS and UPS analysis, there were significant shifts in binding energy and work function values observed that deviated from the theoretical predictions. This suggests that there are complex behaviors occurring the material that may be similar to electrides. These finding highlight the need for further research on the compounds to fully understand and optimize the materials for applications in sustainable technologies.

Acknowledgements:

I would like to thank Dr. Ohsawa and Dr. Ohashi for their mentorship throughout this project. I would also like to thank NIMS and the NNCI for providing me with this incredible opportunity.

Probing Mechanical Vibrations in 2D Materials: A Michelson Interferometer Approach

CNF Summer Student: Amelie Deshazer
Student Affiliation: Materials Science and Engineering, University of Wisconsin Madison

Summer Program(s): 2024 Global Quantum Leap International Research Training Experiences (GQL IRTE) Program at the National Institute for Materials Science (NIMS), Tsukuba, Ibaraki, Japan
Principal Investigator(s): Dr. Ryo Kitaura, National Institute of Materials Science (NIMS), Tsukuba, Japan
Mentor(s): Dr. Daichi Kozawa, National Institute of Materials Science (NIMS), Tsukuba, Japan
Primary Source(s) of Research Funding: NSF GQL IRTE Grant to University of Minnesota No. OISE-2020174
Contact: deshazaf@gmail.com, kozawa.daichi@nims.go.jp, kitaura.ryo@nims.go.jp
Summer Program Website: https://cnf.cornell.edu/education/reu/2024

Abstract:

Two-dimensional (2D) materials have gained attention in recent research due to their unique electrical, mechanical, and optical properties, making them promising candidates for future applications in semiconductors and quantum technologies. However, the intrinsic properties of 2D materials require sensitive instruments for accurate measurement and analysis. One such instrument is an interferometer, which measures interference patterns generated by wave interactions. This paper provides an overview of the interferometer's design, construction, and testing to ensure accurate interference detection. This research aims to utilize the interferometer to measure the mechanical vibrations of 2D materials suspended on membranes.

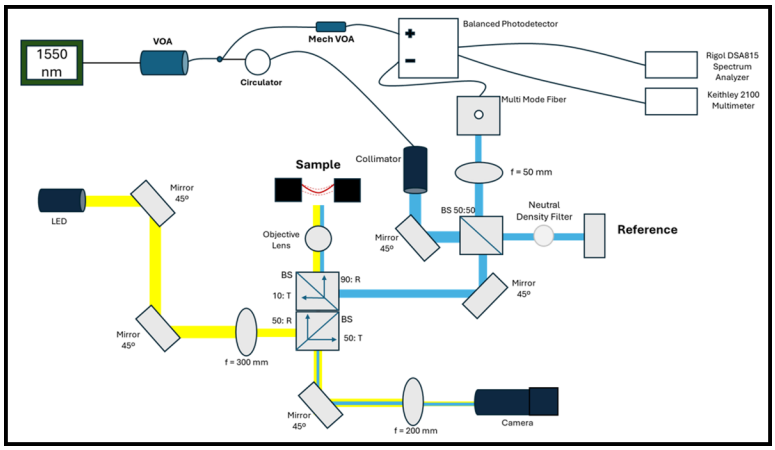

Figure 1: System block diagram of the interferometer.

Summary of Research:

Optomechanics. Optomechanics is a field that examines the interaction between electromagnetic waves and the motion of mechanical resonators. This interaction is studied using a setup where a beamsplitter directs laser beams of different wavelengths onto an oscillator. The radiation force from the lasers creates motion in the oscillator, which generates an interference pattern that is then detected. In linear mechanics, this signal typically produces a single symmetric peak.

This research focuses on nonlinear mechanics characterized by nonsymmetric and multiple peak vibrations. This behavior arises from Brownian motion in 2D materials, where atoms easily oscillate due to external factors. The sensitive nature of these fluctuations requires using an interferometer to accurately study and measure the nonlinear properties of 2D materials.

Building the System. An interferometer was constructed using a Michelson interferometer design, with a primary focus on reflection. Figure 1 presents a system diagram detailing the component configuration.

In this setup, a 1550 nm laser is directed toward the reference arm and the sample. The light reflected from these components interferes at the 50:50 beamsplitter, and the resulting interference pattern is transmitted through a multi-mode fiber to a balanced photodetector. The signal is then output to a spectrum analyzer. An LED is incorporated into the design to illuminate the sample, with the reflected light captured by a Thorlabs CS165MU camera.

The balanced photodetector is crucial for minimizing noise in the system. Given the system's sensitivity, reducing noise from both the sample and reference is essential. The photodetector achieves this by subtracting the - Input from the + Input, which requires the power levels of both inputs to be closely matched. A mechanical variable attenuator is employed to manually adjust the power delivered by the 1550 nm laser.

Automation. The second phase of building the measurement system involved automating the instruments to facilitate data acquisition by developing a graphical user interface

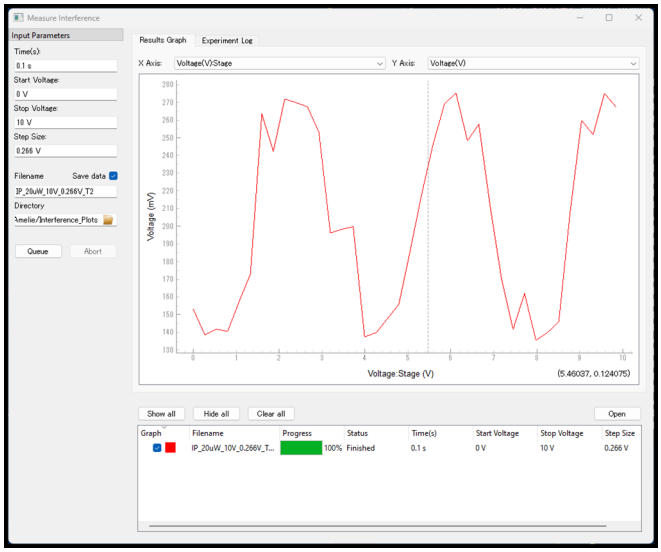

Figure 2: Graphical User Interface (GUI) displaying the interference measurement setup.

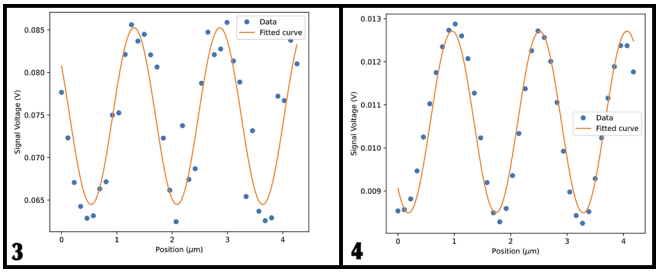

Figure 3, left: DC measurement of the interference pattern with no sample present. Figure 4, right: AC measurement of the interference pattern with no sample present.

(GUI). This was achieved using Python's Pymeasure library. Four instruments were automated: the Rigol DSA815, Thorlabs CS165MU, KPZ101 Piezo stage, and Keithley 2100 Multimeter. Each instrument was programmed into two distinct code blocks: the driver and the procedure. The driver code consisted of command blocks that enabled communication with the respective instrument, while the procedure code generated the GUI by calling the driver to control the device.

Figure 2 illustrates the GUI successfully implemented for two instruments: the KPZ101 Piezo stage and the Keithley 2100 Multimeter. In this setup, the Keithley 2100 measures voltage while the KPZ101 moves the reference arm.

Measuring Interference. Now that a GUI has been successfully created for the measurement system, interference can be measured without samples. The first series of tests were conducted using DC measurements; a Keithley 2100 Multimeter and a KPZ101 Piezo stage were used to measure the interference. The measurement setup involved applying 0 to 10 V to move the KPZ101 stage, with a step size of 0.266 V between data points. As a result, Figure 3 shows the DC measurement for the fit data, where a power of 20 μW was measured at the sample. The interference fitting was based on the sine function equation:

$$X(V) = A * sin(\omega V + \phi) + V_0$$

Noise is shown in the measurement, as illustrated in the graph; therefore, AC measurements were utilized to minimize the noise.

A 0 to 10 V setup was applied with a step size of 0.266 V. An SRS SR830 lock-in amplifier, Keithley 2100 Multimeter, and KPZ101 Piezo stage were used in the measurement process. The power for this measurement was 10 μW at the sample. Figure 4 shows the fitted data using the sine function. The signal voltage was halved as the power was reduced during this measurement, but the noise was minimized. The faint voltage signal is attributed to the power being reduced by half for the AC measurement.

Conclusions and Future Work:

To conclude, an interferometer was built using a 1550 nm laser while automating instruments to facilitate the measurement process. Testing the interference was achieved by employing DC and AC measurements. For this experiment, we successfully built an interferometer and tested interference while minimizing the noise. As a result, more work is needed to be done before testing the mechanical vibrations of 2D materials.

To ensure the interferometer works, frequency domain analyzer measurements are needed to confirm the accuracy of the spectrum analyzer. We need to verify with results that a peak at the center frequency is measured. Once this is confirmed, samples can be measured.

References:

[1] H. Chang, J. Zhang, From cavity optomechanics to cavity-less exciton optomechanics: a review. Nanoscale, 14 (2022), pp. 16710-16730, DOI: 10.1039/D2NR03784J.

[2] Xie, H.; Jiang, S.; Rhodes, D. A.; Hone, J. C.; Shan, J.; Mak, K. F. Tunable exciton-optomechanical coupling in suspended monolayer $MoSe_2$. Nano Lett. 2021, 21, 2538-2543, DOI: 10.1021/acs.nanolett.0c05089.

[3] Morell, N., et al.. Optomechanical Measurement of Thermal Transport in Two-Dimensional $MoSe_2$ Lattices. Nano Lett. 2019, 19, 3143-3150, DOI: 10.1021/acs.nanolett.9b00560.

[4] G. Dion, S. Mejaouri, J. Sylvestre; Reservoir computing with a single delay-coupled non-linear mechanical oscillator. J. Appl. Phys. 21 October 2018; 124 (15): 152132, DOI: 10.1063/1.5038038.

Effect of Annealing Temperature on Nitrogen Vacancy Formation in Nanocrystalline Diamond

CNF Summer Student: Keyes Eames
Student Affiliation: School of Physics, Georgia Institute of Technology

Summer Program(s): 2024 Global Quantum Leap International Research Training Experiences (GQL IRTE) Program at the National Institute for Materials Science (NIMS), Tsukuba, Ibaraki, Japan

Principal Investigator(s): Dr. Tokuyuki Teraji, National Institute for Materials Science (NIMS), Ibaraki, Japan

Primary Source(s) of Research Funding: NSF GQL IRTE Grant to University of Minnesota No. OISE-2020174

Contact: keames3@gatech.edu, teraji.tokuyuki@nims.go.jp

Summer Program Website: https://cnf.cornell.edu/education/reu/2024

Abstract:

Nitrogen-vacancy (NV) centers are diamond lattice defects that are well-suited to quantum sensing. NV-rich nanodiamonds have wide sensing applications in biosensing and nanoelectronics. The present research investigates the effects of annealing temperature and oxygen treatment on NV formation and detection in nanodiamonds. Increasing annealing temperature combined with oxidizing the diamond surface was shown to improve nanodiamond composition and fluorescence.

Summary of Research:

NV centers are color centers in diamond that arise when a substitutional nitrogen atom pairs with a lattice vacancy. NV centers can be neutrally charged (NV^0) or negatively charged (NV^-). NV^- centers have received significant research focus in recent years due to their good quantum properties, such as a long coherence time, optical spin-state initialization, and optical spin-state readout. The spin-dependent energy levels of NV^- centers are sensitive to local magnetic fields, electric fields, temperature, and strain, making them very useful for quantum sensing applications. Nanodiamonds can be formed by crushing bulk diamonds, allowing for high spatial resolution quantum sensing experiments in biosensing and nanoelectronics [1].

Synthetic diamonds can be created by a high-pressure high-temperature compression of a carbon-rich precursor or via a chemical vapor deposition of a carbon-containing gas. Both methods introduce tunable levels of substitutional nitrogen into the diamond lattice [2]. The diamonds are then irradiated with a high-energy electron beam to create lattice vacancies. High-temperature annealing mobilizes the vacancies to pair with nitrogen atoms throughout the diamond lattice and form neutrally charged NV^0 centers. Negatively charged NV^- centers arise when a second substitutional nitrogen atom donates an electron to an NV0 center [3].

NV^- sensors exhibit maximal sensitivity when the NV^- concentration is maximized and the NV^0 concentration is minimized [2]. The current research examines what annealing temperature creates the most NV^- centers without creating a disproportionate amount of NV^0 centers in Tomei MD50 nanodiamonds after irradiating with a high-energy electron beam. The concentration of each NV center was measured by tracking their corresponding peak height on a photoluminescence (PL) spectrum. Measuring temperature-dependent changes in relative NV^0 and NV^- peak heights tracks the relative concentrations of the NV centers.

Due to non-constant sample volumes and graphitization, NV peak heights were determined relative to the phonon sideband such that the PL spectrum was normalized to the range [0,1]. Figure 1 shows the Tomei MD50 NV^0 and NV^- results. Increasing temperature leads to higher NV^-, but NV^0 increases faster and with a larger fractional change. Figure 2 shows that the larger fractional change leads to a declining ratio of NV^-/NV^T, where $NV^T = NV^0 + NV^-$. Higher temperatures also lead to increased graphite on the surface of the nanodiamonds, which significantly reduced the overall fluorescence of higher-temperature samples.

Graphitization on the surface of the diamond led to a blackening of the nanodiamonds visible to the naked eye. The effects of graphitization were counteracted by oxidizing at 550°C for three hours. Oxidizing the diamonds turned them white and increased their overall PL intensity by a factor of 10. Importantly, the two oxidized samples measured showed significant improvements in NV^- concentration and NV^-/NV^T, as shown in Figure 3 and Figure 4.

Conclusions and Future Work:

The present research supports the idea that, within the experimental temperature range of 900-1090°C, increased annealing temperature increases both NV^0 and NV^- concentration. However, higher temperatures seem to induce graphitization and a lowered NV^-/NV^T ratio. Oxidizing nanodiamonds rich in NV centers decreases graphitization, thus increasing the measured NV^- and NV^-/NV^T fluorescence. The inferential weight of these conclusions are limited by the non-constant sample volumes when using nanodiamond

samples. Furthermore, technical limitations prevented measuring the effect of oxidation at different samples on the same diamonds.

The present work focuses only on improving the NV composition of nanodiamonds. However, previous theoretical and experimental work on bulk diamonds suggests that improving diamond composition will improve the underlying quantum properties [2]. Future work is thus needed to measure the effects of NV^- and NV^-/NV^T concentration on T_1 relaxation time, T_2 relaxation time, and the T_2^* decoherence time.

Further research is also needed to determine the compositional effects of oxidizing nanodiamonds which were annealed at increasing temperatures.

Acknowledgements:

This work was made possible by Dr. Tokuyuki Teraji, Dr. Jun Chen, Dr. Takeyuki Tsuji, Dr. Yuta Masuyama, Mrs. Shoko Manako and Mrs. Miyuki Kameoka. Furthermore, this opportunity would not have been possible without the National Institute of Materials Science, the Global Quantum Leap International Training and Research Program, the Cornell NanoScale Facility, and National Science Foundation.

References:

[1] Fujiwara, M., and Shikano, Y. (2021). Diamond quantum thermometry: From foundations to applications. Nanotechnology, 32(48), 482002. https://doi.org/10.1088/1361-6528/ac1fb1.

[2] Barry, J., et al. (2020). Sensitivity optimization for NV-diamond magnetometry. Reviews of Modern Physics, 92(1), 015004. https://doi.org/10.1103/RevModPhys.92.015004.

[3] Shinei, Chikara, et al. "Equilibrium Charge State of NV centers in Diamond." Applied Physics Letters, vol. 119, no. 25, 20 Dec. 2021, https://doi.org/10.1063/5.0079687.

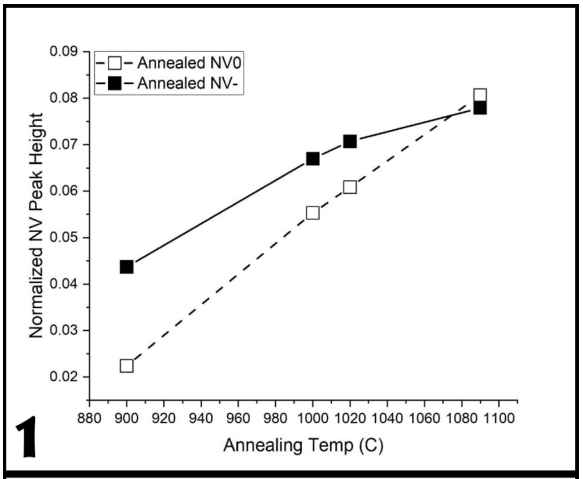

Figure 1: A plot of the NV peak height relative to the phonon sideband versus the annealing temperature. All samples were annealed under vacuum conditions for two hours. Both NV^0 and NV^- normalized peak heights increased within the experimental temperature range of 900-1090°C.

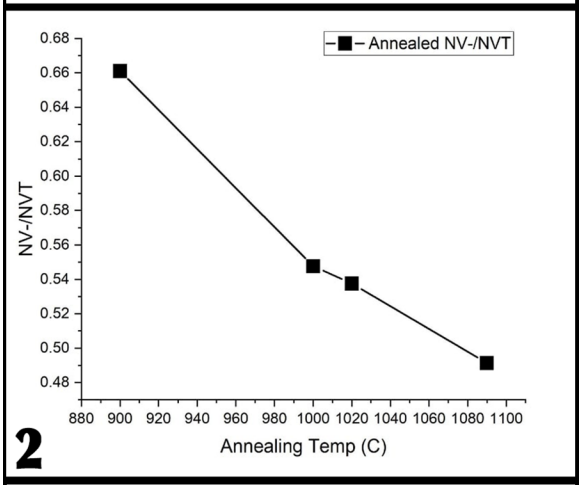

Figure 2: A plot of the NV^-/NV^T, where $NV^T = NV^0 + NV^-$. All samples were annealed under vacuum conditions for two hours. Both NV^0 and NV^- normalized peak heights increased within the experimental temperature range of 900-1090°C.

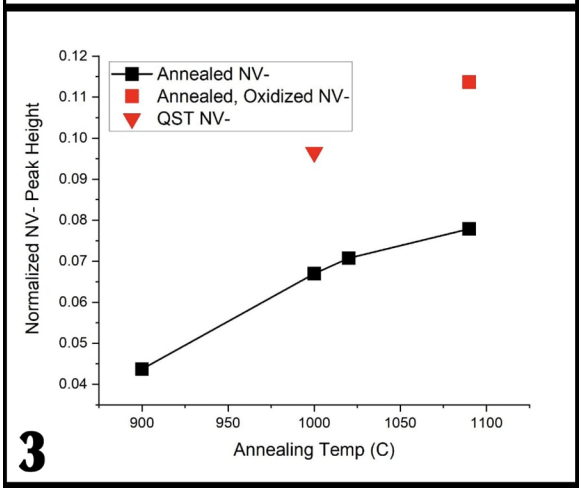

Figure 3: A plot of the normalized NV^- peak height for an annealing-only sample, an annealed and oxidized sample, and a second annealed, oxidized sample provided by the National Institutes of Quantum Science and Technology (QST).

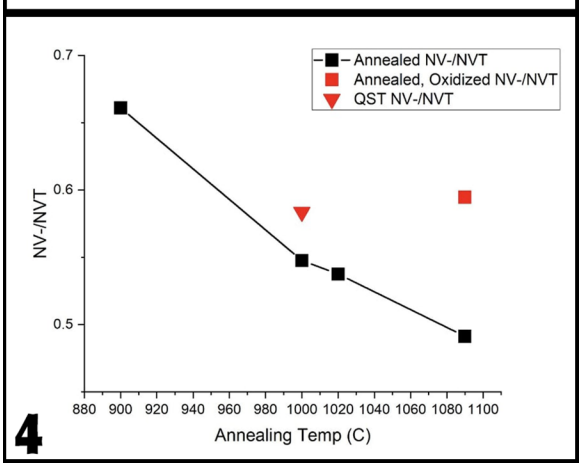

Figure 4: A plot of the NV^-/NV^T ratio for an annealing-only sample, an annealed and oxidized sample, and a second annealed, oxidized sample provided by the QST.

Analysis of the Adhesion and Spreading Behavior of Cellular Spheroids on Supported Lipid Layers

CNF Summer Student: Erica Guelfi
Student Affiliation: Vanderbilt University [undergrad] and Virginia Tech [grad school]

Summer Program(s): 2024 Cornell NanoScale Facility International Research Experiences for Undergraduates (CNF iREU) Program at National Institute for Materials Science (NIMS), Japan
Principal Investigator(s): Dr. Jun Nakanishi, Mechanobiology Group, NIMS, Tsukuba, Ibaraki, Japan
Primary Source(s) of Research Funding: NSF Awards to Cornell OISE-2246252 (IRES) and NNCI-2025233 (NNCI)
Contact: erica.m.guelfi@vanderbilt.edu, ericaguelfi@vt.edu, nakanishi.jun@nims.go.jp
Summer Program Website(s): https://cnf.cornell.edu/education/reu/2024, https://www.nims.go.jp/group/mechanobiology/

Abstract:

Understanding the basic functions of cells, such as spreading and adhesion, is important to generate baseline knowledge on cellular behaviors for more targeted studies. Traditional cellular spreading studies are carried out on hard, planar surfaces which do not mimic physiological conditions. By depositing a layer of biologically relevant lipids onto both liquid-solid and liquid-liquid interfaces, cellular adhesion and spreading behaviors can be studied in multiple environments, providing a more realistic model of how cells move in the body. These cellular functions are mediated by a host of factors, including physical cues, chemical cues, and cell-cell interactions. Monocellular cultures lack these critical cell-cell interactions, making them less analogous to real cell behavior. This study aims to bridge this gap by examining both single-cell and spheroid spreading on supported lipid layers. A seemingly direct relationship was observed between cellular spreading and a cell-adhesive peptide (RGD) density after a long incubation, although a smaller proportion of 0.5% RGD seemed to have increased efficacy in the short term. Further investigation into these relationships can provide insight into cellular spreading behaviors in the body and may eventually serve as a model for cancer metastasis.

Summary of Research:

Background. Cell spreading is facilitated by both internal and external factors, including chemical cues from the cell's environment. RGD is a family of peptides responsible for cellular adhesion and spreading on the extracellular matrix and is found abundantly within the human body [4]. Supported lipid membranes (SLMs) (see Figure 1) are formed from physiologically common lipids that can be conjugated to molecules like RGD to induce cellular spreading based on the literature [2,3]. While the spreading behaviors of single cells are well documented, the behavior of cellular clusters is less well understood due to the influence of intercellular signals and forces.

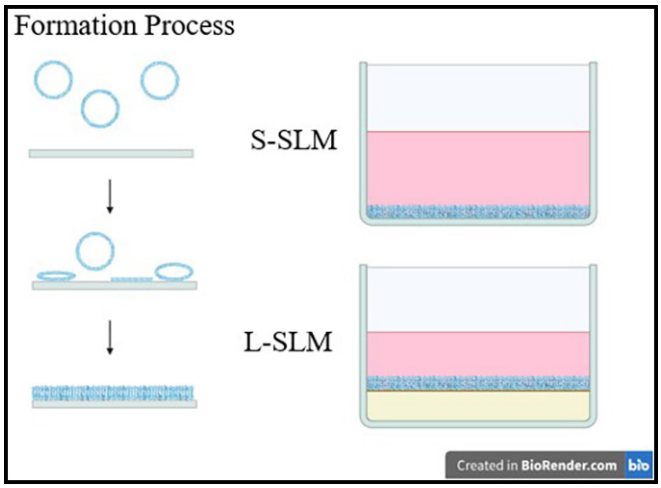

Figure 1: Process of forming SLMs. Solid-SLMs were created by depositing the bilayer at the interface between a functionalized glass slide and cell medium, while liquid-SLMs were created at the interface between perfluorocarbon and cell medium.

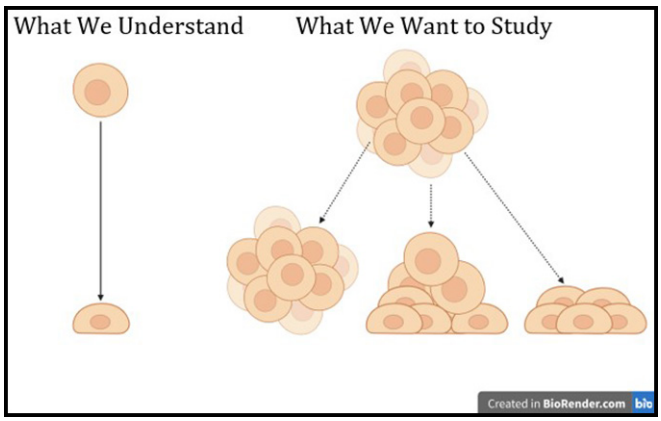

Figure 2: While single-cell spreading is well-studied, the intercellular forces of cellular spheroids make it hard to predict how they will spread.

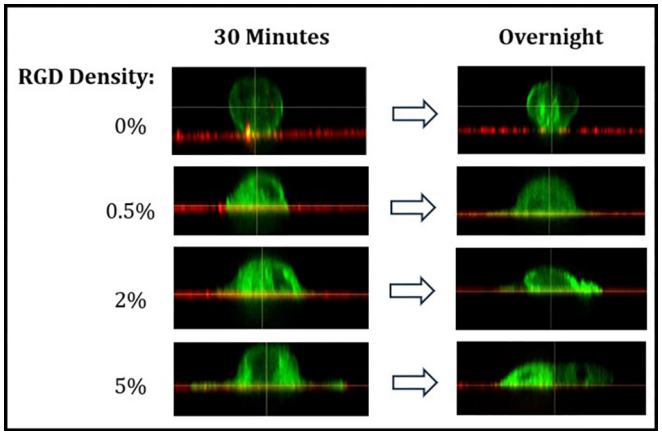

Figure 3: Comparison of confocal images (XZ plane) of cellular spreading on solid-SLMs after 30 minutes and 24 hours of incubation. Red and green fluorescence represent actin and the lipid membrane, respectively. All images are a representative sample from the images taken for that experimental condition.

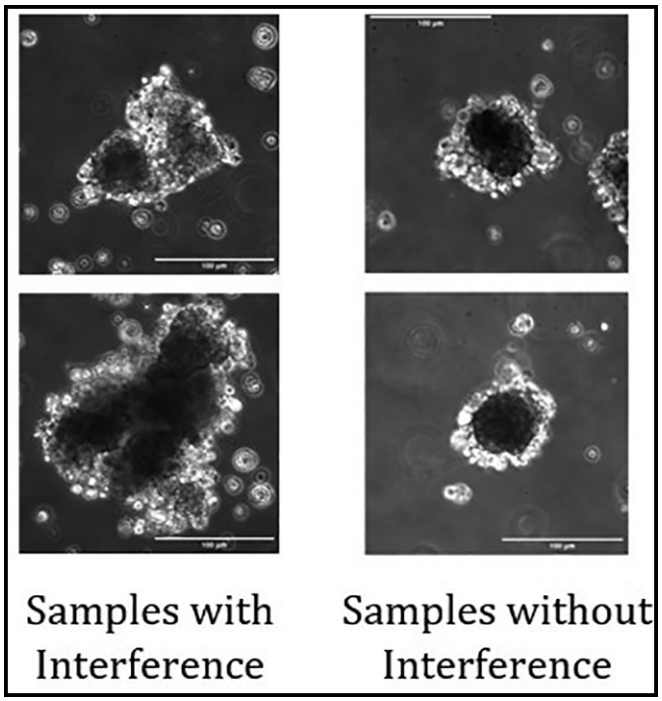

Figure 4: Brightfield images of cellular spheroids showing the adverse effects of shaking during spheroid growth.

Spheroids, or globular clusters of cells, are an important tool as they more closely mimic physiological conditions through the inclusion of these cell-cell interactions [1]. While integrins, which are proteins that control cellular adhesion, bind to the RGD peptide, this force lies in opposition to the proteins binding individual cells in spheroids together. This conflict makes it unclear which forces will win out in spreading experiments (see Figure 2) but can allow for a more accurate picture of how cells migrate within the body.

Case Study: Single Cell Spreading. To first validate the experimental setup and to establish a baseline of spreading behaviors, initial experiments were performed using single Madin-Darby Canine Kidney (MDCK) cells. Cells were incubated overnight on the supported lipid layers and imaged using a confocal microscope after 30 minutes and 24 hours of incubation (see Figure 3), drawing comparisons at different RGD densities. These experiments found that increased cellular spreading appeared directly related to increased levels of RGD in the lipid membrane after overnight incubation. However, cells incubated on 0.5% RGD membranes for 30 minutes seemed to display more spreading than expected, suggesting that perhaps a low proportion of RGD can initially stimulate increased spreading, but that this phenomenon is taken over by more linear trends after a longer incubation period.

Spheroid Formation and Spreading. Cellular clusters were generated from MDCK cells using EZSphere plates. Unfortunately, the non-adhesive coating on the microwells of these plates makes them susceptible to adverse shaking effects. Spheroidal morphology was highly dependent on movement of the plates during medium changes and imaging, and increased shaking would lead to spheroids migrating from one microwell to the next and fusing, creating non-circular amalgamations (see Figure 4). While truly spherical clusters were not formed during the course of this experimentation, "disk-shaped" clusters with a three-dimensional aspect served as an initial approximate to study overall spreading patterns.

Conclusions and Future Steps:

Initial results from these experiments are promising, indicating a potentially linear trend between RGD density and cellular spreading, especially over longer time periods. More investigation is required to understand the potentially increased spreading seen in early culture on 0.5% RGD, but our findings suggest that this RGD density can induce quick early spreading behaviors that slow drastically in the long-term.

Future work will focus on improving spheroid formation techniques to create more uniform and rounded cell clusters. Once a finalized spheroid formation protocol has been established, further study of these cellular clusters on both solid- and liquid-SLMs will be performed, specifically studying the role that intercellular forces play in modifying cell spreading.

In the future, this understanding of spheroid migration and spreading could be used as a rudimentary model for tumor metastasis.

References:

[1] Boot RC, et al. Advances in Physics: X. 2021 Jan 1;6(1). doi:10.1080/23746149.2021.1978316.

[2] Richter RP, et al. Materials Today. 2003 Nov;6(11):32–7. doi:10.1016/s1369-7021(03)01129-5.

[3] Lu Z, et al. Advanced Materials. 2024 Apr 29;36(27). doi:10.1002/adma.202403396.

[4] Yang M, et al. Frontiers in Bioengineering and Biotechnology. 2021 Dec 15;9. doi:10.3389/fbioe.2021.773636.

Impact of Chromium Addition on the Transport Properties of $Mg_3(Sb,Bi)_2$

CNF Summer Student: Alexandra Houseworth
Student Affiliation: Electrical Engineering, Montana State University

Summer Program(s): 2024 Cornell NanoScale Facility International Research Experiences for Undergraduates (CNF iREU) Program at National Institute for Materials Science (NIMS), Japan
Principal Investigator(s): Professor Takao Mori, NIMS, Tsukuba, Ibaraki, Japan
Mentor(s): Dr. Raju Chetty, National Institute for Materials Science, Tsukuba, Ibaraki, Japan
Primary Source(s) of Research Funding: NSF Awards to Cornell OISE-2246252 (IRES) and NNCI-2025233 (NNCI)
Contact: alexandra.houseworth@gmail.com, chetty.raju@nims.go.jp, mori.takao@nims.go.jp
Summer Program Website: https://cnf.cornell.edu/education/reu/2024

Abstract:

$Mg_3(Sb,Bi)_2$ compounds are a promising new material in the search for high efficiency thermoelectric (TE) module components. However, the effect of transition metal doping on the properties of these compounds is not well explored. This research examined the impact of chromium addition coupled with varied sintering temperatures on the electrical and thermal conductivity of $Mg_3(Sb,Bi)_2$ compounds. While the initial goal of the project was to measure the effect of chromium atoms acting as interstitials, it was found that favorable TE properties resulted from higher chromium concentrations at the grain boundaries. Using this new model to target the microstructure, samples prepared with high chromium concentrations and increased sintering temperatures yielded improvements in electrical conductivity and charge carrier mobility, leading to an increase in the low temperature figure of merit (ZT).

Summary of Research:

Introduction and Background. Waste heat recovery is an important step in improving the energy efficiency of the modern power grid. One of the most promising solutions to this problem is the implementation of thermoelectric (TE) modules. TE modules are composed of materials that when subjected to a temperature gradient produce a corresponding potential difference, which can be used for power generation.

While TE modules are reliable, sustainable, and scalable for a variety of applications, the development of these devices is in its infancy due to their low efficiency and high cost. One of the biggest barriers to advancement is in the materials themselves; an effective TE material has a high electrical conductivity but a low thermal conductivity, two material properties that are challenging to decouple. Bismuth telluride-based materials have been the long-standing champion at low to medium temperature ranges but are quite expensive to produce. Research focus has shifted towards developing low-cost alternatives, and the recent discovery of $Mg_3(Sb,Bi)_2$ is promising a new generation of materials. $Mg_3(Sb,Bi)_2$ is competitive with BiTe, but further alloying and modifications of the microstructure are necessary to improve its efficiency.

Previous research into transition metal doping of these compounds has yielded favorable TE properties. Specifically, copper atoms acting as interstitials were found to reduce thermal conductivity, leading to an improved figure of merit [1]. However, there is little research on the impact of chromium doping. The goal of this work was to explore the impact of this element on the transport properties of $Mg_3(Sb,Bi)_2$ compounds

Methodology. Samples with varying chromium concentrations were prepared by combining raw magnesium, bismuth, antimony, tellurium, and chromium into ball milling jars inside of an argon filled glove box. The samples were then milled for five hours, and the resulting powder was spark plasma sintered at 973 K and 1023 K. The densified material was then cut into one 2 mm thick 10 mm diameter disk and one 2 mm square bar. The thermal transport properties of each sample were characterized by Laser Flash Analysis (LFA), and the electrical conductivity and Seebeck coefficient by the ZEM-3 Thermoelectric Characteristics Evaluation System. For both systems, the sample was tested at 50 K intervals from room temperature to 673 K. The microstructure was analyzed using bulk x-ray diffraction (XRD) and scanning electron microscopy (SEM).

Results and Future Work:

The XRD spectra of the 973 K series samples showed little variation from reference $Mg_3(Sb,Bi)_2$ samples with the exception of one peak corresponding to a secondary chromium phase in the two highest concentration samples. The presence of these secondary phases was further confirmed by electron dispersion spectroscopy (Figure 1). The electrical properties of these samples were relatively poor, except for the sample with the greatest chromium concentration (Figure 2).

Because of the prevalence of secondary chromium phases and the poor electrical properties of the material, it was inferred that the chromium atoms were not occupying any lattice sites and instead remained in the secondary phases and at the grain boundaries. When compared with previous work studying

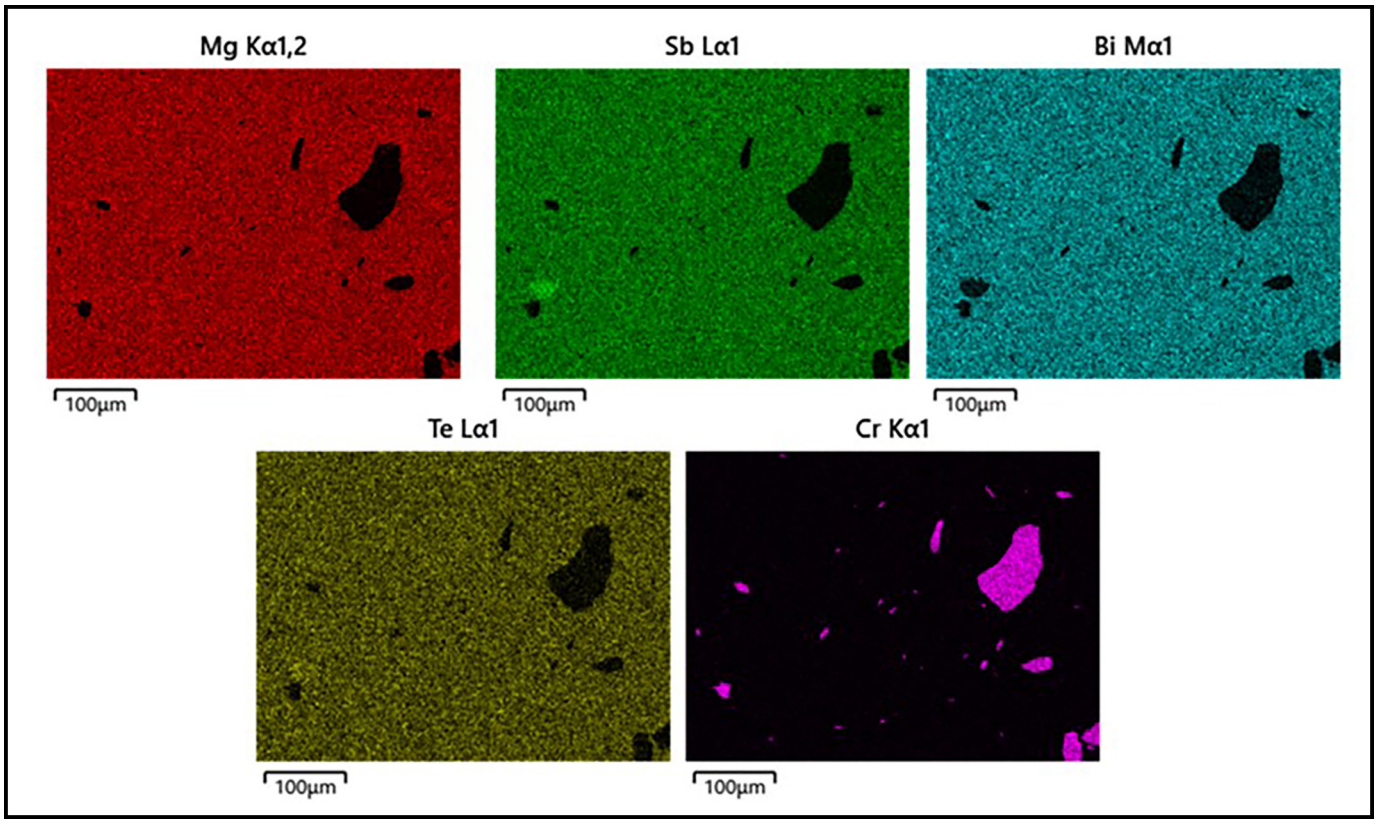

niobium doping of a similar compound, it was found that the same increase in conductivity and weighted mobility occurred at high transition mental concentrations [2]. This was due to a decrease in the grain boundary resistance, improving carrier mobility and overall material performance [3]. After observing this same trend in the chromium doped samples, the project focus shifted from interstitial doping to exploring the relationship between the microstructure and transport properties.

The series of five samples was prepared again at a sintering temperature of 1023 K with the goal of increasing grain size. While secondary phases were still present in this material, these samples saw a dramatic increase in conductivity and weighted mobility when compared with the previous series, especially in the low temperature range (Figure 2). This increase in conductivity led to an overall improvement in the ZT value for the second series (Figure 3).

To verify the presence of chromium at the grain boundaries, the thermal conductivity and Seebeck coefficient of each sample was measured, and the lattice parameter was calculated. Little change in these values was observed regardless of chromium concentration or sintering temperature, evidence that chromium was not acting as an interstitial and distorting the lattice.

Further work is needed to confirm the grain boundary resistance model, both to quantify changing grain size and to understand the fraction of chromium at the grain boundaries. It is unknown if higher chromium concentrations or sintering temperatures would continue to yield favorable properties, a potential route for future experimentation.

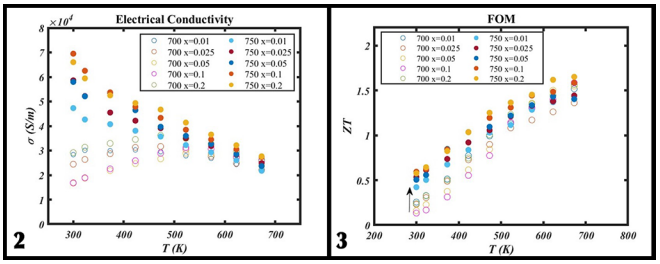

Figure 1, top: EDS images of high concentration Cr sample prepared at 973 K showing Cr secondary phases.

Figure 2, left: Comparison of electrical conductivity at varying Cr concentrations and sintering temperatures.

Figure 3, right: Comparison of ZT values for low and high temperature sample series.

References:

[1] Liu, et al. (2021) Demonstration of ultrahigh thermoelectric efficiency of 7.3% in Mg_3Sb_2/MgAgSb module for low-temperature energy harvesting. Joule 5, 1-13. https://doi.org/10.1016/j.joule.2021.03.017

[2] Luo, et al. (2021). Nb-Mediated Grain Growth and Grain-Boundary Engineering in Mg_3Sb_2-Based Thermoelectric Materials. Advanced Functional Materials 31. https://doi.org/10.1002/adfm.202100258

[3] Kuo, et al. (2018). Grain boundary dominated charge transport in Mg_3Sb_2-based compounds. Energy Environ. Sci., 11, 429. DOI: 10.1039/c7ee03326e.

Fluorinated Ether as an Electrolyte Additive for Lithium-Air Batteries

CNF Summer Student: Bryan Junsuh Kim
Student Affiliation: Chemistry, University of California, Berkeley; Materials Science & Engineering, Massachusetts Institute of Technology

Summer Program(s): 2024 Cornell NanoScale Facility International Research Experiences for Undergraduates (CNF iREU) Program at National Institute for Materials Science (NIMS), Ibaraki, Japan

Principal Investigator(s): Denis Yau Wai Yu, Research Center for Energy and Environmental Materials (GREEN), National Institute of Materials Science (NIMS), Tsukuba, Ibaraki, Japan

Mentor(s): Akihiro Nomura, Research Center for Energy and Environmental Materials (GREEN), National Institute of Materials Science (NIMS), Tsukuba, Ibaraki, Japan

Primary Source(s) of Research Funding: NSF Awards to Cornell OISE-2246252 (IRES) and NNCI-2025233 (NNCI)

Contact: bjunsuhk@mit.edu, yu.denis@nims.go.jp, nomura.akihiro@nims.go.jp

Summer Program Website: https://cnf.cornell.edu/education/reu/2024

Abstract:

Lithium-air batteries have shown promise as a next-generation battery technology due to their utilization of oxygen from ambient air. By using external oxygen instead of an internal oxidizer, the overall battery weight becomes reduced and more lithium can be used for energy storage. Thus, their energy density surpasses modern lithium-ion batteries' and even rivals gasoline fuels'. However, lithium-air batteries' current densities fall far behind industrial standards of at least 10 milliamps per centimeters squared (mA/cm^2) for high-discharge applications (e.g. electrical aircraft, medical devices, consumer electronics) due to the sluggish, diffusion-limited transport of oxygen across the liquid electrolyte. Here, we investigate the co-addition of a well-established fluorinated ether solvent 1,1,2,2-tetrafluoroethyl 2,2,3,3-tetrafluoropropyl (TTE) due to increased oxygen solubility enabled by the molecule's nonpolar fluorocarbons. We find that current densities up to 7.5 mA/cm^2 can be achieved by optimizing the co-solvent ratio to around one-thirds TTE and two-thirds lithium nitrate ($LiNO_3$) in dimethylacetamide (DMA).

Summary of Research:

The lithium-air batteries were assembled as coin cells. The cathode side of the battery was primarily composed of a case with airholes, a stainless-steel spacer, and a porous carbon cathode. The carbon nanotube-based cathode was approximately 2 cm^2 in surface area, and it was wetted with approximately 32 microliters of electrolyte. Cathode materials were separated from the anode side by a membrane separator. The anode side of the battery was primarily composed of a lithium metal disk as the anode, a stainless spacer, and the anode case. The electrodes were connected via voltmeter inside a box connected to an oxygen input line and an exhaust output line.

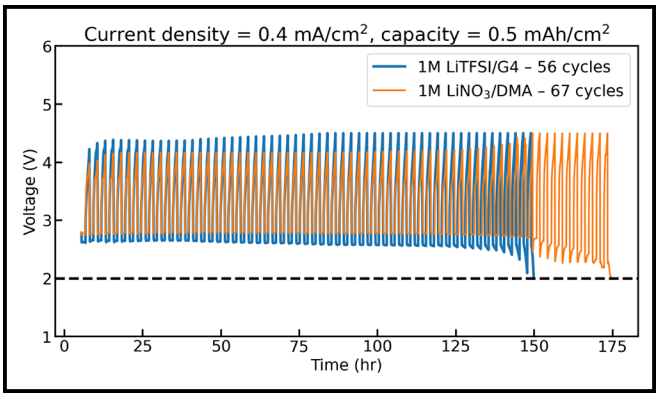

Figure 1: Comparison of lifecycles between 1 M LiTFSI/G4 and 1 M LiNO3/DMA.

Experimental conditions, i.e. current and capacity values, were controlled by an electrochemical workstation that multiple oxygen boxes were inserted in. Battery testing was conducted inside a dryroom with minimal moisture.

One molar (M) $LiNO_3$ in DMA has been known to be a robust candidate as a lithium-air electrolyte because of the stability of straight-chain alkyl amides like DMA in the oxygen electrode [1]. Although DMA is usually expected to be reactive towards lithium metal, the lithium nitrate salt facilitates the formation of a stable solid-electrolyte interphase primarily composed of lithium oxide (Li_2O). As shown in Figure 1, 1 M $LiNO_3$/DMA was demonstrated to boast exceptional cyclelife, or the number of discharge/recharge cycles before a cutoff voltage of 2 volts (V) was reached. At the cutoff voltage, it is expected that the overpotential, or the additional voltage required from the equilibrium potential in order to compensate for side reactions, has become large enough such that the battery has unstabilized due to degradation. At relatively shallow current density and capacity, the DMA-

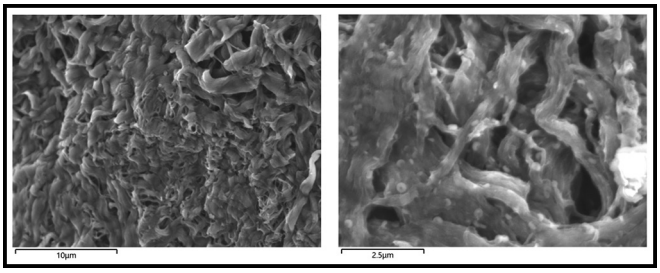

Figure 2: SEM images of a pristine porous carbon cathode (left) and Li_2O_2-deposited porous carbon cathode (right).

based electrolyte showed superior lifecycle compared to 1 M lithium bis(trifluoromethanesulfonyl)imide (LiTFSI) in tetraglyme (G4) solvent: a well-established electrolyte. The electrolytes were prepared in an argon glovebox before being transferred to the dryroom. The discharge reaction between lithium and oxygen forms lithium peroxide (Li_2O_2) as a product with toroidal morphology. Figure 2 shows scanning electron microscopy (SEM) images of a pristine carbon cathode compared with a post-discharge carbon cathode, the latter being deposited with discrete, toroid Li_2O_2 particles.

For TTE experiments, TTE was co-added to G4 at various volume ratios in order to identify an approximate range for oxygen solubility. The oxygen solubilities were measured were an optical oxygen monitor, in which near-infrared emission detected from initial red-light excitation is correlated with oxygen concentration. A co-addition volume in the proximity of a range of 10 to 30% of TTE was shown to maximize oxygen solubility due to the nonpolar fluorocarbons in TTE [2]. 33% TTE was paired with 67% $LiNO_3$/DMA to test larger discharge currents and capacities.

As shown in Figure 3, the electrolyte combination was observed to sustain several cycles of discharge current densities up to 7.5 mA/cm^2. Lithium-air batteries typically cannot sustain current densities beyond 1 mA/cm^2, but the TTE/DMA-based electrolyte was able to approach a commercial benchmark of 10 mA/cm^2 [3,4]. In Figure 4, it was observed that counter-intuitively, larger current densities seem to prolong the cyclelife of lithium-air batteries rather than diminish it. This observation can be hypothesized to be due to formation of a disordered Li_2O_2 discharge product more facile to oxidize during the recharge process.

Conclusions and Future Steps:

Here, heavier discharge current densities up to 7.5 mA/cm^2 were sustainable for an electrolyte of two-thirds LiNO3/DMA and one-thirds TTE by volume. Future steps include a more rigorous optimization of the volume ratios, as the oxygen solubility measurements were conducted for pure solvents rather than lithium salt electrolytes. Furthermore, in order to investigate the hypothesis concerning the prolonged cyclelife at larger current densities, characterization techniques such as SEM and X-Ray Diffraction (XRD) can be employed to probe into the structural differences between the Li_2O_2 discharge product at various current densities.

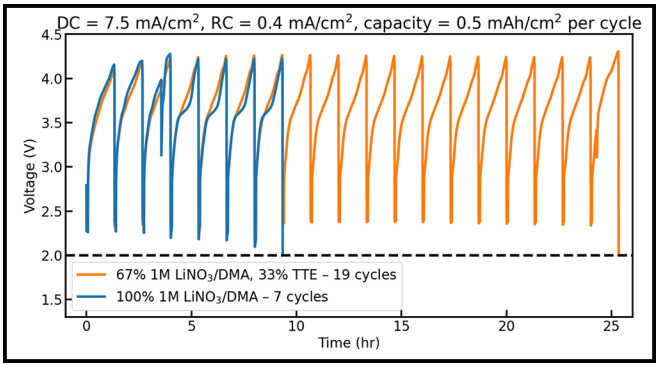

Figure 3: Comparison of lifecycles between 100% 1M $LiNO_3$/DMA and 67% 1M $LiNO_3$/DMA with 33% co-added TTE.

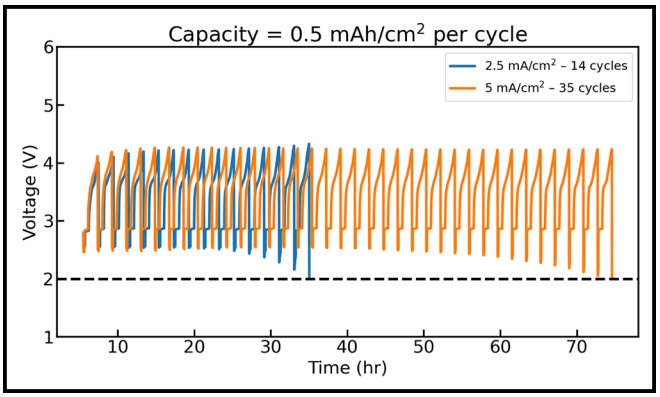

Figure 4: Comparison of lifecycles between 2.5 mA/cm^2 and 5 mA/cm^2 for 1 M $LiNO_3$/DMA with 30-minute intermittent rests between discharge and charge.

Acknowledgements:

I would like to thank the National Science Foundation awards to Cornell University under OISE-2246252 (IRES) and NNCI-2025233 (NNCI) for funding my participation in this research program. I would further like to thank Prof. Denis Y.W. Yu, Dr. Akihiro Nomura, technical staff members, and group members at NIMS for their advisory and support in letting me pursue my own research independence and design of experiments. Last but not least, thank you to Dr. Lynn Rathbun, Garry Bordonaro, and Hiroko Inoue for their immense logistical support throughout the program.

References:

[1] Walker, W. Giordani, V., Uddin, J., Bryantsev, V.S., Chase, G.V., Addison, D. J. Am. Chem. Soc. 2013, 135, 6, 2076-79.

[2] Zhao, Q., Zhang, W., Sun, G., Cong, L., Sun, K., Xie, H., Liu, J. ACS Appl. Mater. Interfaces 2018, 10, 31, 26312–26319

[3] Bennett, W.R., Dornbusch, D., Knudsen, K.B., Mehta, M.R., McCloskey, B.D., Lawson, J.W. NASA, 2020.

[4] Girishkumar, G., McCloskey, B., Luntz, A.C., Swanson, S., Wilcke, W., J. Phys. Chem. Lett. 2010, 1, 14, 2193-2203.

Transport of Intensity Equation for Characterizing Nanostructures and Applications for Laser Cooling Experiments

CNF Summer Student: Cedric Silva
Student Affiliation: Physics and Astronomy, University of Louisville

Summer Program(s): 2024 Global Quantum Leap International Research Training Experiences (GQL IRTE) Program at the National Institute for Materials Science (NIMS), Tsukuba, Ibaraki, Japan
Principal Investigator: Dr. Satoshi Ishii, National Institute for Materials Science (NIMS), Tsukuba, Ibaraki, Japan
Primary Source(s) of Research Funding: NSF GQL IRTE Award to University of Minnesota No. OISE-2020174
Contact: cedsilva3@gmail.com, sishii@nims.go.jp
Summer Program Website: https://cnf.cornell.edu/education/reu/2024

Abstract:

Laser cooling has become a popular topic at the forefront of scientific research in recent years. Scientists continue to achieve colder material temperatures using laser cooling methods. Despite this, how a sample's temperature profile evolves during such experiments is a subfield that has yet to be extensively covered. To learn more, research was conducted into the phase retrieval method called transport of intensity equation (TIE), its calibration with nanostructures, and its prospects for laser cooling experiments. The acquired phase information from TIE coupled with the characterization of a material's temperature dependent refractive index can allow for accurate temperature-profile data to be collected.

Introduction:

In the realm of nanotechnology, being able to quickly and accurately determine a structure's dimensions is extremely useful. One popular method to do this is atomic force microscopy (AFM). However, using this method has several disadvantages including the time needed to acquire data and the cost of entry. Another method is to determine the dimensions via phase information utilizing a quantitative phase imaging (QPI) technique. This phase information can be collected through experiments involving interferometry and lasers; however, these setups are typically complex and rely on environmental factors [1]. An alternative QPI approach that avoids these contingencies and offers a more accessible solution is to use TIE, as shown in Figure 1. TIE possesses several strengths: it only needs an intensity measurement to obtain phase, works with partially coherent light sources, collects data extremely fast, and has high flexibility in its setup construction [2]. Due to these reasons, TIE was chosen as the best candidate to be implemented in laser cooling experiments. However, for this prospect to be explored, a well-calibrated TIE setup is of utmost importance. Experiments were conducted to properly calibrate a TIE setup to quickly obtain phase information from photoresist samples.

$$-k\frac{\partial I(\boldsymbol{r})}{\partial z} = \nabla \cdot \left[I(\boldsymbol{r})\, \nabla \phi(\boldsymbol{r}) \right]$$

Figure 1: Transport of intensity equation from Jialin Zhang, et al. [3].

Summary of Research:

For the TIE setup, an unconventional, infinitely corrected microscope was chosen because of the accessibility of the optical components. The setup was assembled according to the simplified diagram shown in Figure 2. The light source was a white LED with peak emission intensities at 450 and 545 nm. An aperture and condenser lens focused the light to the sample, which is a glass substrate topped with polymer photoresists fabricated in a grid-like pattern. After passing through the sample, the objective lens collected the light and formed an initial image. The light then passed through the tube lens where a dichroic filter was attached to eliminate intensities at wavelengths below 500 nm. The camera position moved along the z-axis to capture both in-focus and defocused images.

These images were analyzed using modified MATLAB codes provided in [2], where an intensity derivative was calculated using finite difference method before being applied to a TIE solver to obtain the phase information. Several algorithms have been developed to solve TIE, but the universal solution presented by Zhang et al. was chosen here primarily due to its excellent solution convergence [3]. In Figure 3, the phase contrast between the photoresist and the background can be seen in a 2D map.

After experimentally determining pixel size, the last step in the process is to take this phase data and convert it into a height profile for the photoresist using equations provided in [1]. The resulting graph, shown in Figure 4, indicates the photoresist is approximately 20 μm wide and 263 nm tall at its highest point. These values agree with AFM data, taken three years prior, showing a maximum height of 261 nm. However, the AFM data does not indicate a fluctuation of height as strong as Figure 4 does. Countless photoresists were profiled, and the discrepancy is thought to be attributed to two factors: most samples have sustained physical damage over the years, and the background phase contains non-uniform noise.

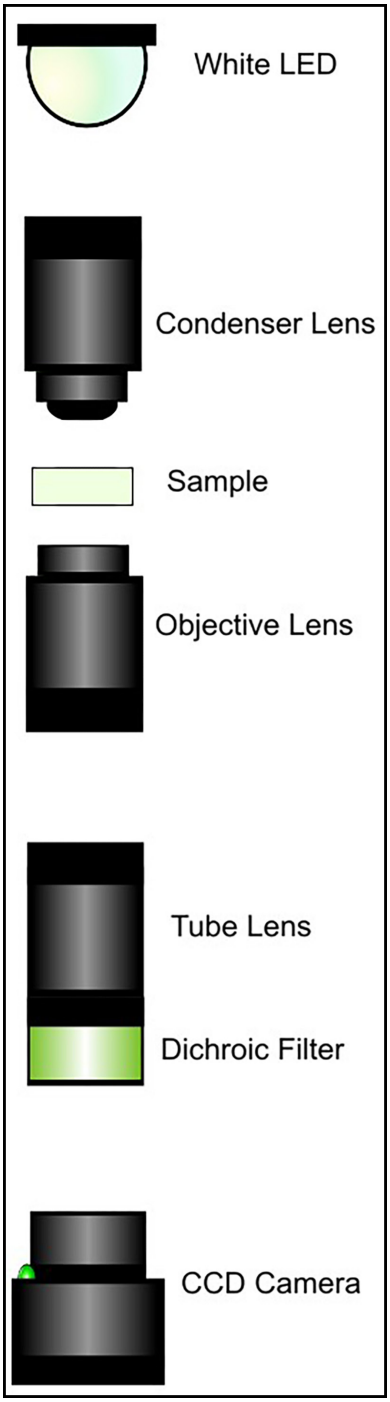

Figure 2: Experimental setup for TIE.

Conclusions and Future Steps:

Ultimately, more data would need to be collected on separate samples to affirm that the data collection process is replicable and applicable to a wider range of imaging subjects. Additionally, further computational work can be done to mitigate background noise when collecting and processing phase data to ensure proper calibration is achieved.

Looking ahead, a well-calibrated TIE experimental setup not only offers scientists a reliable method for obtaining the dimensions of nanostructures, but it is also a powerful tool to quickly extract phase information for various applications. In fact, the article by Zuo, et al. outlines a slightly more complex optical setup that allows for the collection of focused and defocused images simultaneously [2]. This method would allow for nearly instantaneous phase measurements and has several prospects in laser cooling applications. Alongside the research into TIE, an extensive Python code was developed to automate the collection of fluorescence data from rare-earth doped fluoride glass samples using a 2D grid, motorized stage, and spectrometer with Lightfield software [4]. Coupling the code with TIE would allow for seamless temperature-profile data to be collected which could help to expand the range of laser cooling experiments being conducted in the future.

Acknowledgements:

I am grateful for the support of my research advisor, Dr. Ishii, my supervising graduate student, Kevin Tanjaya, and everyone in the research group who helped to make my experience so memorable. A big thank you also goes to my supervisors from Cornell and NIMS personnel who made the program run seamlessly. I learned a lot both academically and culturally. It was an unforgettable experience!

References:

[1] Basanta Bhaduri, et al. Diffraction phase microscopy: principles and applications in materials and life sciences. Adv. Opt. Photon. 6, 57-119 (2014). https://doi.org/10.1364/AOP.6.000057.

[2] Chao Zuo, et al. Transport of intensity equation: a tutorial. Optics and Lasers in Engineering 135, 106187 (2020). https://doi.org/10.1016/j.optlaseng.2020.106187.

[3] Jialin Zhang, et al. On a universal solution to the transport-of-intensity equation. Opt. Lett. 45, 3649-3652 (2020). https://doi.org/10.1364/OL.391823.

[4] Xiaojing Xia, et al. Quantum point defects for solid-state laser refrigeration. Advanced Materials, 33:1905406 (2020). https://doi.org/10.1002/adma.201905406.

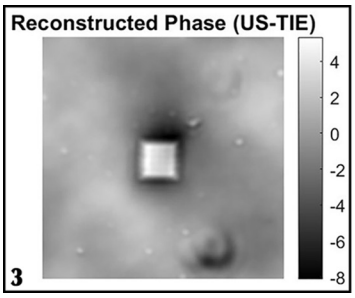

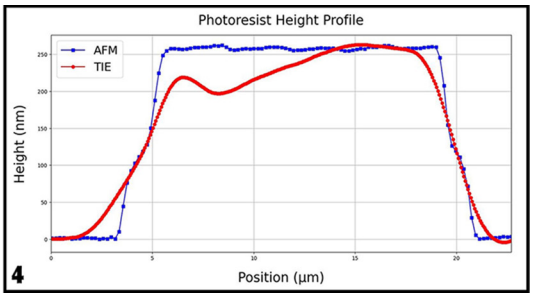

Figure 3, left: Phase reconstruction utilizing Matlab codes provided in Chao Zuo, et al. [2].
Figure 4, right: Height profile of a photoresist.

Tuning Molecular Weight of Poly(NIPAAm-co-HIPAAm-co-SAKIPAAm) to Improve Biomarker Enrichment

CNF Summer Student: Maxim Sokolov
Student Affiliation: University of California, Berkeley

Summer Program(s): 2024 Cornell NanoScale Facility International Research Experiences for Undergraduates (CNF iREU) Program at National Institute for Materials Science (NIMS), Japan

Principal Investigator(s): Dr. Mitsuhiro Ebara, Smart Polymers Group, National Institute for Materials Science (NIMS), Tsukuba, Ibaraki, Japan

Mentor(s): Dr. Ahmed Nabil, Soichiro Yoshizumi, Smart Polymers Group, NIMS

Primary Source(s) of Research Funding: NSF Awards to Cornell OISE-2246252 (IRES) and NNCI-2025233 (NNCI)

Contact: msokolov@berkeley.edu, ebara.mitsuhiro@nims.go.jp, tolba.ahmednabil@nims.go.jp, ousoui1203@gmail.com

Summer Program Website: https://cnf.cornell.edu/education/reu/2024

Abstract:

"Smart" polymers, those that can reversibly change physio-chemical properties in response to an outside stimulus (e.g. ionic concentration, temperature, pH) have been studied for a range of biomedical applications. Among them, temperature responsive polymers have been studied best, bearing applications in early disease detection through biomarker enrichment, drug delivery, and cell sheet engineering. The parameters enabling these polymers to perform their tasks most effectively have not been fully explored. We synthesized poly(NIPAAm-co-HIPAAm-co-SAKIPAAm) in varying conditions to determine a relationship between reaction parameters and molecular weight.

Summary of Research:

Background and Motivation. Viruses contain characteristic proteins which, as biomarkers for disease, can be used in diagnosis. Low biomarker concentration can make detection difficult, potentially causing false negative test results. Additionally, underdeveloped communities are often limited to cheaper, less powerful tests. By conjugating an antibody selective for a disease biomarker to a temperature responsive polymer, the polymer can be precipitated out of solution, increasing the concentration of the sample and increasing the power of the applied test. This process is called biomarker enrichment. The polymer does not need to be cleaved from the antibody and biomarker in order to analyze the sample, allowing for easy testing after polymer introduction. Poly(NIPAAmco-HIPAAm-co-SAKIPAAm) is used because PNIPAAm is well studied, and HIPAAm converts to SAKIPAAm, which readily conjugates with antibodies through click chemistry [1].

Different monomer ratios and molecular weights will affect the temperature at which the polymer will precipitate out of solution, the lower critical solution temperature (LCST). They will also affect the polymer's ability to enrich biomarkers. Low molecular weight polymers are susceptible to agglomeration, and larger ones may tangle [2]. Too many functional sites will cause competition between antibodies, and too few will not be effective. There exists a set of optimal parameters for enrichment, so it

ID	In Feed (M %)		DBCO acid (mg)	CDT (mM)	AIBN (mM)	N+H conc. (M)	Time (h)	NMR Comp (M %)			GPC M_W (g/mol)	Đ
	N	H						N	H	SAKI		
A1	70	30	-	94.4	18.9	4	24	78.5	21.5	-	10403	1.06
A2	70	27	36	94.4	18.9	4	24	78.5	7	14.5	10825	1.05
A3	70	28.5	18	94.4	18.9	4	24	78.5	10.9	10.6	10821	1.05
B1	70	30	-	47.2	9.4	4	24	76.5	23.5	-	17063	1.16
B2	70	27	36	47.2	9.4	4	24	76.5	8.5	15	17151	1.16
B3	70	28.5	18	47.2	9.4	4	24	76.5	18.5	5	16761	1.15
C1	70	30	-	23.6	4.7	4	24	81	19	-	33060	1.37
C2	70	27	36	23.6	4.7	4	24	100			33506	1.30
C3	70	28.5	18	23.6	4.7	4	24	81	8.2	10.8		
D1	70	30	-	11.8	2.4	4	21	71.5	28.5	-	13783	1.16
*E1	90	10	-	47.2	4.8	2	8	86	14	-	4806	1.14
F1	70	30	-	23.6	2.4	4	8	72	28	-	7936	1.10
F2	70	30	-	15.7	1.6	6	8	79	21	-	10702	1.12
G1	50	50	-	23.6	2.4	4	8	63	37	-	8036	1.13
G2	50	50	-	15.7	1.6	6	8	53.5	46.5	-	12181	1.15
H3	70	30	-	23.6	2.4	4	51	77	23	-		
H4	70	30	-	23.6	2.4	4	94	79.5	20.5	-		

Table 1: Tabulated reaction parameters and characterization results for all samples.

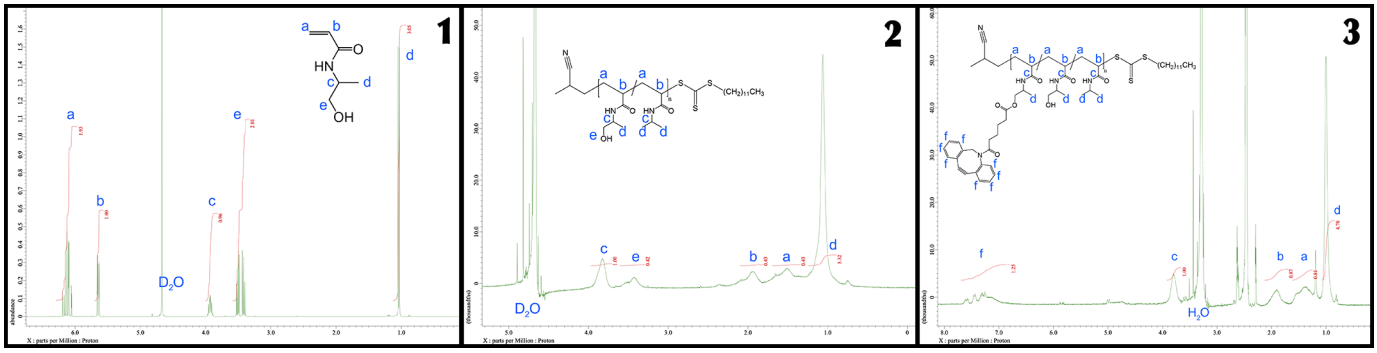

Figure 1: HIPAAm 1H-NMR data. Figure 2: poly(NIPAAm-co-HIPAAm) 1H-NMR data for sample A1. Figure 3: poly(NIPAAm-co-HIPAAm-co-SAKIPAAm) 1H-NMR data for sample A2..

is worthwhile to investigate how these parameters affect the polymer's efficacy, and how reaction conditions affect these parameters.

Goal 3 of the United Nations' 2030 Agenda for Sustainable Development is to "ensure healthy lives and promote well-being for all at all ages." Underdeveloped areas have demonstrated a clear need for low-cost, portable, and fast disease detection. Our group's Smart-Ex biomarker enrichment technology is simple to use, inexpensive, and allows testing in a variety of conditions, helping meet these global demands.

Materials and Methods. NIPAAm monomer was recrystallized from stock solution under hexane, then vacuum dried. HIPAAm monomer was synthesized according to [3], then the monomers were polymerized by reversible addition fragmentation chain transfer (RAFT) polymerization using cyanomethyldodecyl trithiocarbonate (CDT) as chain transfer agent (CTA) and azobisisobutyronitrile (AIBN) as radical initiator. Polymerizations were performed in various schemes. In the first block, 4M of NIPAAm and HIPAAm monomer in ethanol at a 7:3 molar ratio was used. CDT and AIBN were fixed in a 5:1 ratio. CTA molarity varied inversely to target molecular weight, constant of proportionality k=472. After 24h in a 60°C oil bath, the polymer was dissolved in tetrahydrofuran, reprecipitated in diethyl ether, and vacuum dried. According to the process described in [4], some HIPAAm units in the polymer were converted to SAKIPAAm, and the sample was again dried.

The second trial involved a variation in molarity of the monomers in ethanol at 2M, 4M, and 6M as well as NIPAAm/HIPAAm molar ratios of 9/1, 7/3, and 5/5 for a total of nine samples. They were polymerized for 8 hours at 60°C, dissolved in THF, reprecipitated in diethyl ether, and dried. HIPAAm monomer was characterized with hydrogen nuclear magnetic resonance spectroscopy (1H-NMR, JEOL ECS 400, 300MHz) and polymerized samples were characterized with gel permeation chromatography (GPC, Shimadzu Nexera, solvent: DMF containing 10 mmol/L LiCl, standard: poly(styrene)).

Results and Discussion. HIPAAm monomer NMR data are shown in Figure 1. Representative NMR data for poly(NIPAAm-co-HIPAAm) and poly(NIPAAm-co-HIPAAm-co-SAKIPAAm) are shown in Figure 2 and Figure 3, respectively. The results of polymer synthesis are shown in Table 1. Two of the 2M samples were lost due to equipment malfunction, and two of the 90/10 molar ratio samples failed to polymerize. The remaining 90/10 sample had an exceptionally low yield. NMR failed for sample C2.

The peaks indicate that HIPAAm, poly(NIPAAm-co-HIPAAm) and poly(NIPAAm-co-HIPAAm-co-SAKIPAAm) were successfully synthesized. Additionally, results from the second block of polymerizations suggest molarity has a positive effect on polymer length, and monomer ratio has no effect. RAFT agent and initiator concentration have a negative impact on molecular weight, as predicted. HIPAAm generally exists in a lower percentage in polymer than in initial monomer concentration, according to NMR data.

Halving the amount of DBCO acid decreases the amount of SAKI groups present, but not necessarily by half. Overall, variation between samples is high, despite similar reaction conditions.

Conclusions:

Poly(NIPAAm-co-HIPAAm-co-SAKIPAAm) was successfully synthesized at different molecular weights. Poly(NIPAAm-co-HIPAAm) was successfully synthesized at different molecular weights in different reaction conditions. Time and reaction molarity have a positive impact on molecular weight. RAFT agent and initiator concentration have a negative impact on molecular weight, and monomer ratio has no impact on molecular weight. Significant variation exists between monomer input and NMR results. Stronger, quantitative relationships are difficult to form due to this uncertainty as well as measurement uncertainty. Further work conjugating these polymers with antibodies is ongoing.

References:

[1] https://doi.org/10.1039/c9sc03368h.

[2] https://doi.org/10.3390/polym8110380.

[3] https://doi.org/10.1021/bm050829b.

[4] https://doi.org/10.1039/D1BM00349F.

A New Route for Exosome Detection Using All-Dielectric Metasurfaces

CNF Summer Student: Kenndal Williams
Student Affiliation(s): University of Texas at San Antonio, Cornell University

Summer Program(s): 2024 Cornell NanoScale Facility International Research Experiences for Undergraduates (CNF iREU) Program at National Institute for Materials Science (NIMS), Japan
Principal Investigator(s): Masanobu Iwanaga, National Institute for Materials Science (NIMS), Tsukuba, Ibaraki, Japan
Primary Source(s) of Research Funding: NSF Awards to Cornell OISE-2246252 (IRES) and NNCI-2025233 (NNCI)
Contact: wil.kenn03@gmail.com, iwanaga.masanobu@nims.go.jp
Summer Program Website: https://cnf.cornell.edu/education/reu/2024

Abstract:

Exosomes are extracellular vesicles (30-150 nm in diameter) that play critical roles in cellular processes such as immune modulation, signal transduction, and antigen response. Due to their ability to reflect the physiological state of their origin, exosomes hold promise as non-invasive biomarkers for disease diagnosis and prognosis. To harness this potential, exosomes must first be effectively isolated and detected. In this study, we present an advanced metasurface fluorescence (FL) biosensor, engineered with an all-dielectric metasurface substrate coupled to a six-channel microfluidic chip, designed for the high-sensitivity detection of exosomes. Our approach involved targeting both the exosomal surface marker CD63 and internal exosome proteins through fluorescence-tagged antibodies, specifically anti-CD63 and anti-EXOSC5. As a preliminary result, the developed sensor exhibited a remarkable limit of detection of 9.64 attomolar, corresponding to 5.804×10^3 exosomes/mL, positioning it among the most sensitive biosensors reported to date for exosome detection. These findings highlight the significant potential of this metasurface sensor to enhance the precision and efficacy of exosome-based diagnostics.

Summary of Research:

To detect extracellular exosomes, a metasurface fluorescence biosensor was constructed from an all-dielectric metasurface substrate and a six-channel microfluidic (MF) chip synthesized from transparent poly-dimethylsiloxane (PDMS). On the substrate are six sensors. Using nanolithography, the metasurface sensors were designed to be a periodic array of silicon nanopellets of diameter of 220 nm forming a square lattice. These nanopellets have strongly localized electric fields at the outermost surface and have localized strong magnetic fields inside allowing for a significant increase in detection sensitivity. The PDMS microfluidic chip is placed on top of the metasurface substrate and temporarily fuses together through adhesion.

The biosensor is placed in the microfluidic configuration for fluorescent imaging. It is placed on a microscope stage and tubes are connected to it allowing for fluids to run through the channels, over the sensors and out into a waste beaker. The movement of the fluids is powered by a rotary pump and flow of the fluids will be stopped when pictures are needed to be taken.

Experiment 1: Targeting CD63:

The first experiment centered on detecting CD63, a well-known transmembrane marker used for identifying exosomes. CD63 plays critical roles in cell-matrix adhesion, migration, and immune regulation, making it an essential target for exosome identification. In this experiment, the fluorophore HL555 was conjugated to an anti-CD63 antibody using the Hilyte Fluor 555 labeling kit, forming the detection antibody. Concurrently, biotin-labeled anti-CD63 antibodies were used as the capture mechanism. Human exosome standards were diluted into a range of concentrations (from 10^4 to 10^8 exosomes/mL) and incubated with both the HL555-labeled and biotin-labeled anti-CD63 antibodies, synthesizing the exosome complex.

The MF protocol follows a pattern of flowing necessary proteins or exosomes through the channels followed by phosphate-buffered saline (PBS) rinse, allowing the molecules time to adhere to the sensor and rid of any that are unbound. Cystatin-SA protein flowed through the channels to create a binding site for the biotin-labeled-anti-CD63 antibodies.

After immobilizing the exosomes on the cystatin-SA-coated nanopellets, the green excitation light is turned on and fluorescence images are taken of each channel. ImageJ software was used to measure net fluorescence intensity across the channels, providing a quantitative evaluation of exosome binding. Data analysis using the Hill equation revealed a negative correlation between fluorescence intensity and exosome concentration and a value less than one for the degree of cooperative reaction, suggesting anti-cooperative binding behavior between the antibodies and the target exosomes.

Experiment 2: Targeting Inner Exosome Proteins Using anti-EXOSC5:

The second experiment took a different approach by targeting the interior of exosomes through the protein EXOSC5, an exosome component involved in RNA degradation and processing. Studies have shown that EXOSC5 has similar properties to protein found within the extracellular exosomes, enough so, that anti-EXOSC5 can be used to target them. The same HL555 fluorophore conjugation procedure was employed to label the anti-EXOSC5 antibody for detection, while anti-CD63-biotin continued to serve as the capture mechanism.

In this experiment, exosome samples were prepared at concentrations ranging from 10^3 to 10^7 exosomes/mL. The samples were incubated with anti-CD63-biotin at room temperature to facilitate initial binding, followed by a second incubation with anti-EXOSC5-HL555 at 37°C (body temperature). Before the second incubation, anti-EXOSC5-HL555 was diluted in 0.1% PBS-T, which softens and partially cleaves the exosome membrane, allowing the labeled antibody to penetrate the vesicle. Once the exosome-antibody complexes were synthesized, they were introduced into the microfluidic system following a similarly modified MF protocol.

Fluorescence intensity measurements were once again obtained using ImageJ, and the results revealed a stronger positive correlation between fluorescence intensity and exosome concentration than observed in the first experiment. The Hill equation was applied to evaluate the binding interactions, showing a cooperative reaction with a degree of cooperative binding of 73.1425. The limit of detection (LOD) was determined to be 9.64 attomolar, equivalent to 5.804×10^3 exosomes/mL. This LOD is among the lowest reported for exosome biosensors, demonstrating the effectiveness of targeting internal exosome proteins in enhancing detection sensitivity.

These findings illustrate the superior sensitivity of the metasurface biosensor, particularly when targeting internal exosome proteins, and underscore its potential application in diagnostic platforms.

Conclusions and Future Steps:

This research highlights the efficacy of an all-dielectric metasurface biosensor in detecting extracellular exosomes, leveraging both external and internal protein markers. In the first experiment, targeting the transmembrane protein CD63 resulted in anti-cooperative binding and lower-than-anticipated fluorescence intensity, revealing the complexities of surface protein detection. However, the second experiment, focusing on internal proteins with anti-EXOSC5, demonstrated significantly improved outcomes, characterized by a strong cooperative binding response and an exceptionally low limit of detection. These findings underscore the potential of this biosensor technology in advancing diagnostic applications, particularly in diseases where exosome detection plays a pivotal role.

Future investigations should concentrate on refining both the binding and microfluidic protocols to enhance the efficiency and sensitivity of exosome detection. This includes optimizing antibody selection and incubation conditions to improve binding affinity and reduce variability. Additionally, expanding the biosensor's capabilities through multiplexing to simultaneously target multiple exosome markers could provide even greater diagnostic specificity. The results from this research affirm the rich potential of exosomes as next-generation biomarkers, offering significant promise for improving disease diagnosis and monitoring.

Acknowledgements:

I would like to extend my deepest gratitude to my principal investigator, Dr. Iwanaga, for his unwavering support and for entrusting me with this project. I also wish to thank Dr. Rathbun and the National Institute for Materials Science (NIMS) for their valuable guidance and collaboration. This work would not have been possible without the generous funding and resources provided, for which I am sincerely appreciative.

References:

[1] M. Iwanaga. All-Dielectric Metasurface Fluorescence Biosensors for High-Sensitivity Antibody/Antigen Detection. ACS Nano. 2020 Dec 22;14(12):17458-17467. 10.1021/acsnano.0c07722.

[2] M. Iwanaga, T. Hironaka, N. Ikeda, T. Sugasawa, and K. Takekoshi. Metasurface Biosensors Enabling Single-Molecule Sensing of Cell-Free DNA. Nano Letters. 2023; 23(12): 5755-5761. 10.1021/acs.nanolett.3c01527.

CNF

Cornell NanoScale
Science and Technology Facility

国立研究開発法人
物質・材料研究機構